7-2021

On the Local Heat Transfer Behavior or Supercritical Carbon Dioxide

Neil Sullivan

ON THE LOCAL HEAT TRANSFER BEHAVIOR OF SUPERCRITICAL CARBON DIOXIDE

By

Neil Sullivan

A Dissertation Submitted to the Faculty of Embry-Riddle Aeronautical University

In Partial Fulfillment of the Requirements for the Degree of

Doctor of Philosophy in Aerospace Engineering

July 2021

Embry-Riddle Aeronautical University

Daytona Beach, Florida

ON THE LOCAL HEAT TRANSFER BEHAVIOR OR SUPERCRITICAL CARBON DIOXIDE

By

Neil Sullivan

This Dissertation was prepared under the direction of the candidate's Dissertation Committee Chairman, Dr. Mark Ricklick, Department of Aerospace Engineering, and has been approved by the members of the Dissertation Committee. It was submitted to the Office of the Senior Vice President for Academic Affairs and Provost, and was accepted in the partial fulfillment of the requirements for the Degree of Doctor of Philosophy in Aerospace Engineering.

DISSERTATION COMMITTEE

Mark Ricklick Digitally signed by Mark Ricklick Date: 2021.08.03 16:05:17 -04'00'

Chairman, Dr. Mark Ricklick

Sandra Boetcher Digitally signed by Sandra Boetcher Date: 2021.08.03 16:19:29 -04'00'

Co-Chair, Dr. Sandra Boetcher

Member, Dr. John Ekaterinaris

Scott Martin Digitally signed by Scott Martin Date: 2021.08.03 15:33:05 -05'00'

Member, Dr. Scott Martin

Bertrand Rollin Digitally signed by Bertrand Rollin Date: 2021.08.03 22:57:23 -07'00'

Member, Dr. Bertrand Rollin

Sirish Namilae Digitally signed by Sirish Namilae Date: 2021.08.04 13:57:51 -04'00'

Graduate Program Coordinator,
Dr. Sirish Namilae

Date

Maj Mirmirani Digitally signed by Maj Mirmirani Date: 2021.08.04 14:54:11 -04'00'

Dean of the College of Engineering,
Dr. Maj Mirmirani

Date

Lon Moeller Digitally signed by Lon Moeller Date: 2021.08.04 15:06:25 -04'00'

Senior Vice President for Academic Affairs and Provost
Lon Moeller, J.D.

Date

ACKNOWLEDGEMENTS

Here is one of those projects that have one author, but nevertheless cannot be completed alone. Thanks go first to my dissertation committee chairman, Dr. Mark Ricklick, for his patience and guidance with this research, invaluable as we climbed the supercritical fluids learning curve in tandem. I thank my committee co-chair, Dr. Sandra Boetcher, who aside from technical matters has provided much needed insight into the world of research and academia I am about to enter. I express my appreciation as well to my committee members for their contributions, making this work possible.

To my lab colleagues, thanks for showing me, through your example, what is possible with years of effort. I don't know if I'd have gotten this far not having seen those who came before me succeed. Anish: you did it with a smile on your face. I've never met anyone with a better work ethic, and I hope a fraction of that rubs off on me. Karthik: thank you for continuously running the blower; you have made the rest of the world sound like beautiful music by comparison.

I would like to recognize the mentorship I received as an instructor from Dr. Lakshmanan Narayanaswami. He has been an immense help, unknowingly kickstarting my teaching career, while fostering a latent fondness for the practice.

Though no longer with us, and not an engineer, the single largest contributor to my life and my greatest champion has been my dad. It is beyond question I would not be sitting here, writing this, without his love and support. My only means of recompense is to help others, try to make a meaningful contribution to my field, and to leave the world a slightly better place than I found it. Thanks, Dad.

ABSTRACT

A detailed study of the local heat transfer behavior of supercritical carbon dioxide (sCO_2) is performed. Flows relevant to heat transfer devices, such as sCO_2 heaters, recuperators, and internally cooled turbine blades are studied, with particular attention paid to data reduction methodology, and the use of appropriate reference quantities, non-dimensionalizations, and correlations. Additionally, a semi-intrusive temperature measurement technique capable of obtaining highly spatially resolved temperature distributions is adapted for use in the challenging conditions of supercritical (SC) flow. SC fluids have proven difficult to study both experimentally and numerically due to dramatically changing thermodynamic and transport properties near the critical point. It is clear from the existing literature that the heat transfer processes within a SC flow vary from those of a subcritical flow, particularly near the pseudo-critical line. Poor predictions of heat transfer rates may lead to unexpected pinch-points in heat exchangers or heat transfer degradation. Existing experimental research of SC flow heat transfer has largely been limited to spatially averaged trends and/or simplified geometries. There remains a gap between the techniques used in the subcritical regime, and the needs of the supercritical fluids industries and sciences. Numerical simulations that are benchmarked against experimental sCO_2 heat transfer data evaluate the ability of existing correlations to predict heat transfer in the SC regime, both away from and very near the critical point and pseudocritical line. As it is desired to harness the advantages arising from the peaks in k and c_p along this line, a study is performed assessing the applicability of a reduced-order model to this effect. Semi-intrusive temperature measurement is achieved, using proper calibration and coating, with accuracy approximating (uncalibrated) type-T

thermocouple uncertainty. The benchmarked numerical simulations give good agreement with experimental HTC data, suggesting the use of commercial RANS code is suitable as a building block for the study of the physics of these flows. New, modified heat transfer correlations are obtained for sCO_2 turbine blade cooling geometry. Additionally, experimental uncertainty for calculated heat transfer quantities is quantified for the first time in the near-critical region, where fluid properties see very large gradients.

TABLE OF CONTENTS

LIST OF FIGURES

Figure Page

Figure Page

Figure Page

Figure Page

LIST OF TABLES

NOMENCLATURE

β	Coefficient of thermal expansion	[1/K]
Bo	Boiling number	
Bu	Buoyancy parameter	
c_p	Specific heat capacity at constant pressure	[J/kg-K]
CFD	Computational Fluid Dynamics	
CMOS	Complementary metal-oxide-semiconductor	
D	Diameter	[m]
DNS	Direct Numerical Simulation	
EoS	Equation of State	
f	Friction factor	
g	Earth surface gravitational constant	9.81 m/s^2
G	Mass flux	[kg/m^2-s]
γ	Ratio of specific heats	
Gr	Grashof number	
h	Specific enthalpy	[J/kg]
HTC	Heat Transfer Coefficient	[W/m^2-K]
IR	Infrared	
ISSI	Innovative Scientific Solutions Incorporated	
k	Thermal conductivity	[W/m-K]

k	Turbulent kinetic energy	[J/kg]
LES	Large Eddy Simulation	
LMTD	Log-Mean Temperature Difference	[K]
$\dot{m}$	Mass flow rate	[kg/s]
μ	Dynamic viscosity	[Pa-s]
Nu	Nusselt number	
ν	Kinematic viscosity	[m^2/s]
NIST	National Institute of Standards and Technology	
P	Pressure	[Pa]
PCHE	Printed Circuit Heat Exchanger	
Pr	Prandtl number	
q''	Heat flux	[W/m^2]
R	Specific gas constant	[J/kg-K]
ρ	Density	[kg/m^3]
RANS	Reynolds-Averaged Navier-Stokes	
REFPROP	NIST Reference Fluid Thermodynamic and Transport Properties Database	
Re	Reynolds number	
RSS	Root-Sum-Square	
RTD	Resistance Temperature Detector	

SBO	Supercritical boiling number	
sCO_2	Supercritical carbon dioxide	
SST	Menter's Shear Stress Transport k-ω turbulence model	
SW	Span & Wagner Equation of State	
T	Temperature	[K]
τ	Shear stress	[Pa]
TIT	Turbine Inlet Temperature	[K]
TLC	Thermochromic Liquid Crystal	
TSP	Temperature Sensitive Paint	
u	Velocity	[m/s]
UV	Ultraviolet	
v	Specific volume	[m^3/kg]
y^+	Non-dimensional wall distance	
Z	Compressibility factor	

SUBSCRIPTS

B	Bulk
C	Critical
F	Film
H	Hydraulic

In	Inlet
Lg	Latent heat
out	Outlet
pc	Pseudocritical
R	Reduced
W	Wall

1. Introduction

Supercritical fluids are essential for the operation of a wide range of modern processes. For example, supercritical carbon dioxide (sCO_2) has been proposed as a working fluid in a number of advanced thermodynamic cycles for power generation (Carraro, 2021). Supercritical water, helium and CO_2 are widely studied for use in refrigeration and power generation cycles (Lorentzen, 1994; Pioro, 2005). Use of supercritical fluids in power generation, in the form of sCO_2 Brayton cycles, have the potential to provide significant gains in thermal efficiency compared with steam Rankine and gas Brayton cycles, while enabling the use of smaller turbomachinery for the same electrical power output (Ahn, 2015). A better understanding of thermodynamic behavior near the critical point is essential to improving compressor design for these cycles, given significant variation in compressibility (Avadhanula, 2017; Ameli, 2018). The possible increase in thermal efficiency is due, in part, to the large gradient in thermodynamic and transport properties near the critical point (Yang, 2000). Careful heat transfer device design, promoting high effectiveness is required to take advantage of this unique fluid behavior.

1.1. Motivation

Supercritical fluids have proven difficult to study, both experimentally and numerically, precisely due to these dramatically changing thermodynamic and transport properties. These changes can lead to significant deviations from established Nusselt number correlations for internal flows and create “pinch points” in a heat exchanger. This can manifest as a temperature increase in the hot-side fluid or a reversal of the heat flow direction (Lazova, 2016). Careful design and high heat exchanger effectiveness will be

required to harness this unique fluid behavior, particularly in flows near the critical point.

Thermal efficiencies for oxy-combustion sCO_2 cycles can approach 60%, but require higher turbine inlet temperature (TIT), for which active blade cooling will be required (Brun, 2014). To achieve meaningful temperature and heat transfer coefficient (HTC) data and characterize local heat transfer behavior, the ability to measure a continuous distribution of temperature is desired, however some techniques traditionally used in air may not be suitable for the current application. Infrared measurement is a popular non-intrusive technique, but problems arise due to the absorptivity of CO_2 in this bandwidth. Semi-intrusive techniques are also popular, such as thermochromic liquid crystals (TLC) and temperature sensitive paints (TSP). TLCs work well in gas-phase experiments near atmospheric temperatures, but the temperature resolution bandwidth is relatively narrow (Smith, 2001). TSP is the currently proposed semi-intrusive temperature measurement technique and work is performed here to adapt it for accurate, repeated use in the harsh sCO_2 environment.

Oxy-combustion sCO_2 Brayton cycles are poised to become one of the most important new technologies in power generation. To move toward commercialization of this cycle, an improved understanding of heat transfer in sCO_2 is needed, both in heat exchangers and for turbine blade cooling. There currently exists no local temperature or heat transfer coefficient data in the experimental literature. Further, there is no standard method of data reduction and presentation in sCO_2 heat transfer research analogous to that seen in conventional flows. This work intends to address these issues.

1.2. Cooling Flows

Studies of heat transfer to supercritical fluids are built on lessons learned from

thermal management flows in conventional fluids, such as air or steam. Existing methods of measurement, analysis, data reduction, and modeling that exist in the literature can be modified for the unique thermophysical nature of sCO_2 and applied to flows, namely, in active turbine blade cooling and heat exchangers.

1.2.1. Turbine Blade Cooling

Traditional gas turbines employing the Brayton cycle with air as the working fluid have long operated with firing and turbine inlet temperatures well in excess of allowable metal temperatures, and in many cases, above their melting points (Wright, 2013). This has necessitated innovative cooling techniques, both to maintain integrity and improve service life of hot gas path components, in the face of increasing temperatures as higher thermal efficiencies are sought. As the source of coolant flow is bleed air from compressor outlet, increased pressure ratios (again, in search of higher thermal efficiency) result in higher temperature bleed air. The first cooled turbine blades 50 years ago used circular, constant cross section tubes inside the airfoil. Modern hot gas path components are thermally managed using external (film) cooling, internal (convective) cooling, careful materials selection, a thermally driven mechanical design of cooling components, and selection of the cooling fluid (Bunker, 2007). Internal cooling now consists of jet impingement, and rib-turbulated, dimpled and pin-fin cooling passages (Wright, 2013). An example of a typical internal cooling arrangement is shown in Figure 1.1.

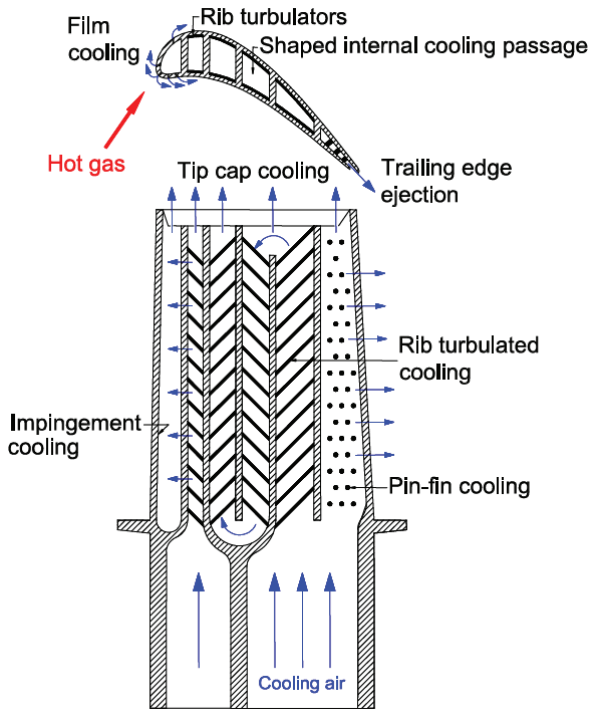

Figure 1.1 Turbine internal cooling channels example (Wright, 2013).

Leading edge, mid-chord, and trailing edge cooling channels may all have different cross sections. Pin-fin channels are often used at the rear of the chord, which is a thinner section that sees a significant heating load (Wright, 2013). The pin-fin channel increases the heat transfer area, increases turbulence in the channel, and produces 3-dimensional horseshoe vortices, all of which promote heat transfer. The pins also impart the hollow channel strength and rigidity. The pin-fin channel is treated below in this paper.

1.2.2. Heat Exchangers

All hot gas path components in turbines can be modeled as heat exchangers. Typically, regardless of heat exchanger construction type or flow arrangement (parallel-flow or counter-flow), heat exchanger performance is determined by the heat load and the log-mean temperature difference (LMTD) (Bergman, 2011). The temperature profile for a simple parallel-flow heat exchanger is seen in Figure 1.2.

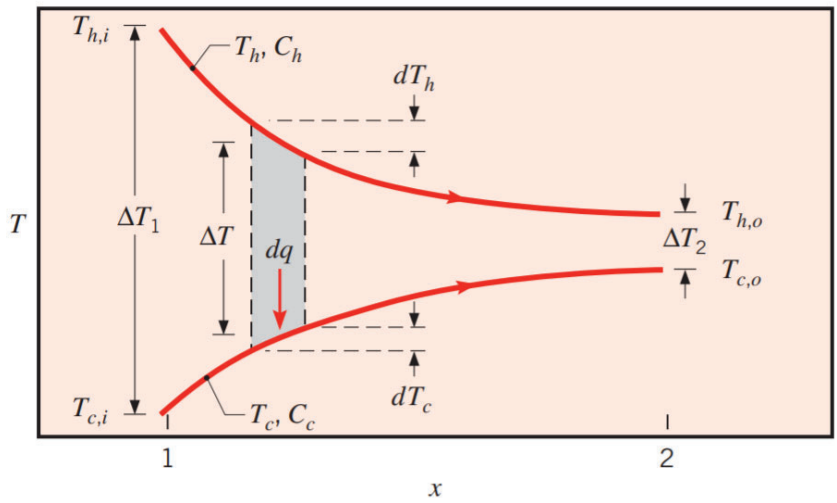

Figure 1.2 Streamwise temperature distribution in a parallel flow heat exchanger (Bergman, 2011).

If an overall HTC U can be obtained thus:

$$\frac{1}{UA} = \frac{1}{U_c A_c} = \frac{1}{U_h A_h} = \frac{1}{(hA)_c} + R_w + \frac{1}{(hA)_h} \tag{1}$$

Where h is the convection coefficient, subscripts c and h represent the cold and hot sides of the heat exchanger, respectively, and R_w is the thermal resistance of the wall separating the flows, a heat transfer rate can be expressed in this form:

$$q = UA\Delta T_m \tag{2}$$

Where ΔT_m is some form of mean temperature. An incremental change in heat dq can be expressed as:

$$dq = -\dot{m}_h c_{p,h} dT_h \tag{3}$$

On the hot side, where $\dot{m}_h$ is the hot side fluid mass flow rate, $c_{p,h}$ is the specific heat of the hot side fluid, and dT_h is the incremental change in temperature, and:

$$dq = \dot{m}_c c_{p,c} dT_c \tag{4}$$

Equivalently, for the cold side. An incremental heat transfer rate can also be expressed holistically for the heat exchanger as:

$$\mathrm{d}q = U\Delta T\mathrm{d}A \tag{5}$$

Here, ΔT is the local temperature difference between the hot and cold side fluids, which is constantly changing. Using the form from Equation 2, the appropriate mean difference, owing to Newton's law of cooling, is the LMTD, shown in Equation 6.

$$\mathrm{LMTD} = \frac{\Delta T_2 - \Delta T_1}{\ln(\Delta T_2/\Delta T_1)} \tag{6}$$

For the parallel flow configuration, ΔT_1 is the temperature difference at hot and cold side inlets, and ΔT_2 is the difference at both outlets. For a counterflow configuration, ΔT_1 would be the difference between hot inlet and cold outlet, and ΔT_2 would be the difference between hot outlet and cold inlet. Note that for a counterflow configuration, the cold side outlet temperature can exceed the hot side inlet temperature. This is not the case with parallel flow. This method is very useful for many applications, but makes many assumptions, one of which is a constant value of specific heat on hot and cold sides in Equations 3 and 4. For flows involving a phase change, two-phase flows, or flows with varying thermophysical properties, such as those discussed here, this traditional analytical approach may no longer be appropriate.

Compact heat exchangers are a critical component in advanced power cycles, and these are often proposed for sCO_2 cycles. The *surface area density* is a useful metric for heat exchanger "compactness" and is the ratio of heat transfer area to heat exchanger volume. A typical shell and tube heat exchanger has a surface area density of $\sim 100\ \mathrm{m^2/m^3}$ and a compact heat exchanger is considered one with a value in excess of $700\ \mathrm{m^2/m^3}$ for gas flows, or $400\ \mathrm{m^2/m^3}$ for liquid flows (Kwon, 2020). Figure 1.3

shows a comparison of shell and tube and a printed circuit heat exchanger (PCHE) of equivalent capacity.

Figure 1.3 PCHE size compared with equivalent shell and tube heat exchanger (Kwon, 2020).

These compact devices typically incur larger pressure drops and have hydraulic diameters under 5 mm. A significant number of studies have been performed on various PCHE flow geometries, including different cross sections (though mostly semi-circular due to the fabrication process) and several types of turbulators (straight and zig-zag ribs) (Kwon, 2020).

1.3. Supercritical Fluids

A supercritical fluid is a fluid at a condition above its critical temperature and critical pressure. At this (T, P) location, intermolecular forces become less dominant than inertial forces, and the densities of corresponding liquid and gas phases converge, eliminating any phase change or phase boundary above this point (Yang, 2000). This removes any surface tension or latent heat of vaporization in the traditional sense. In the presence of strong density gradients, this can give rise to a more complex and nuanced regime of two-

phase flow: devoid of droplets but instead containing “parcels” or “blobs” of denser liquid-like fluid in a less dense medium. A (T, P) phase diagram for CO_2 is shown in Figure 1.4.

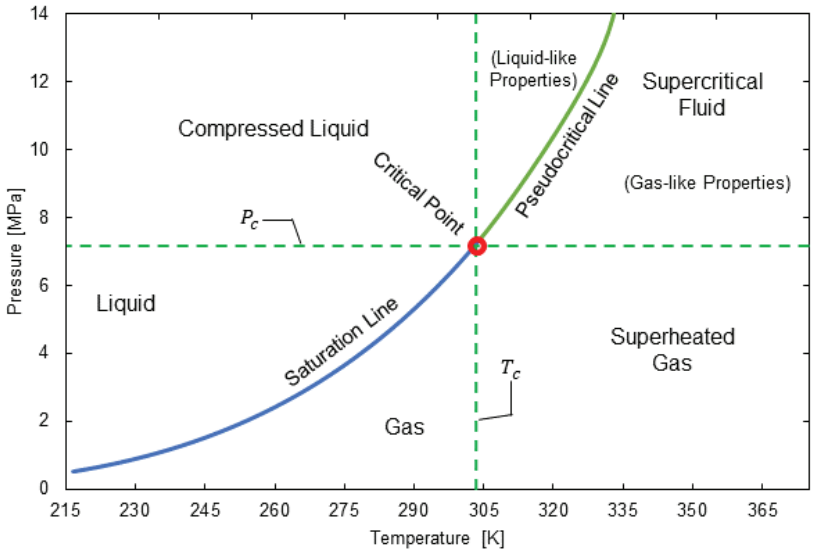

Figure 1.4 CO_2 phase diagram, including supercritical region

The critical region is characterized by significant gradients in thermodynamic and transport properties. At the critical point, as the surface tension and latent enthalpy approach zero, the specific heat (c_p) and thermal conductivity (k) tend to infinity, creating a singularity. This point also sees strong gradients in density (ρ) and viscosity (μ). The large variation in properties is seen in Figure 1.5.

The pseudocritical line is essentially an extension of the saturation line from the critical point into the supercritical region, and here, instead of representing the location of a phase change, it connects temperatures (the pseudocritical temperature, T_{pc}) where heat capacity is maximum for a given pressure. In crossing this line, through addition or removal of heat, the fluid will experience *pseudoboiling*, a maximum change in volume

and a minimum change in temperature. Departures from expected heat transfer behavior in supercritical flows are partially attributed to this behavior.

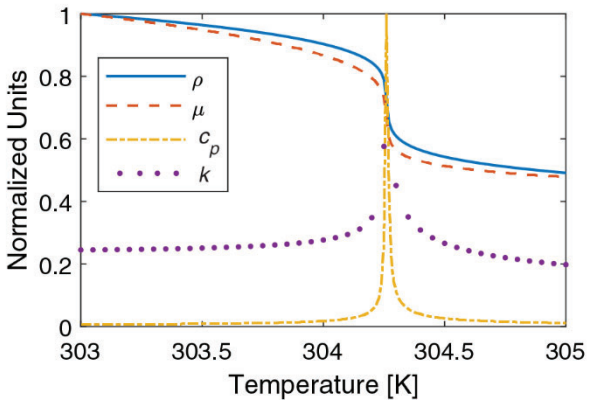

Figure 1.5 Normalized fluid properties on a 7.4 MPa isobar

The pseudocritical line divides the supercritical region into sub regions: one with more liquid-like properties at higher pressures and lower temperatures, and another with more gas-like properties at (relatively) lower pressures and higher temperatures. The peaks in c_p and k decrease with increasing distance from the critical point, at higher pressures and temperatures. The variable properties, while potentially advantageous for heat transfer applications, can create problems in experimental situations with data acquisition and data reduction, and introduce numerical instability to computational work.

1.4. Semi-Intrusive Temperature Measurement

Several non- and semi-intrusive temperature measurement techniques are available to researchers in the heat transfer community. The method germane to present work is a semi-intrusive technique using TSP. The term *semi-intrusive* is used because this method has a lower impact on a flow than would an array of thermocouples, however the wetted

surface is prepared with paint, resulting in a non-zero impact on the flow (by contrast, IR imaging does not require any surface preparation). TSP consists of luminescent molecules called luminophores suspended in an oxygen-impermeable polymer binder. The binder is mixed with a solvent and sprayed onto a surface of interest. The solvent then evaporates from the surface, leaving behind the binder and luminophores. These molecules absorb an excitation light source of appropriate wavelength and store this radiation energy in a variety of excited electronic states. The stored energy can be released via several pathways, both radiative, and non-radiative. A diagram of energy storage and conversion is shown in Figure 1.6.

Electrons can release energy by emitting a photon of a longer wavelength via radiative relaxation: phosphorescence is associated with triplet excited states and longer time scales, and fluorescence is associated with singlet excited states and shorter time scales (fluorescence is the luminescence mechanism upon which TSP is based). Energy can also be transferred by internal conversion between energy states, and external conversion (energy transfer with other molecules through collisions).

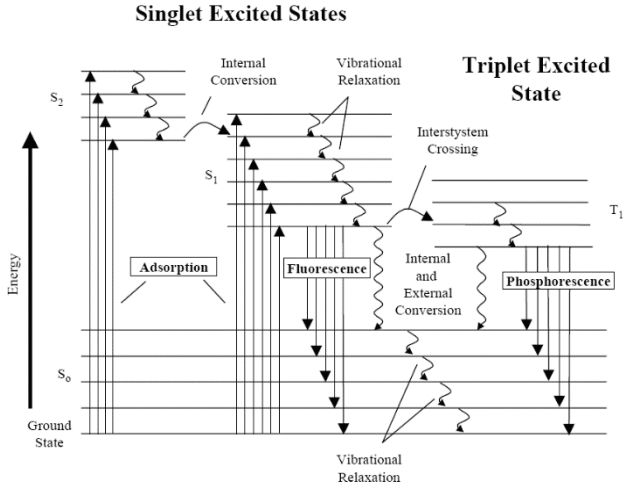

Figure 1.6 Jablonski energy level diagram (Liu, 2005)

Energy transfer by external conversion in this manner is called thermal quenching. The probability of collision with adjacent molecules, either luminophore or binder, increases with increasing temperature, and so the quantum efficiency of luminescence decreases. The result is an inverse relationship between temperature and luminophore photon emission (Liu, 2005). The temperature of a surface can therefore be evaluated by measuring the light intensity of a TSP-coated surface under an excitation light. Temperature is calculated by comparing the intensity of emitted light at an unknown temperature to the intensity at a known temperature, in a ratio. The intensity ratio is compared to an established calibration curve, from which the unknown temperature is obtained.

2. Literature Review

There is a sizeable body of work, both experimental and numerical, on using the unique properties of sCO_2 to advantage in advanced cycles, using advanced components. Methods of analysis and data reduction, however, lack consistency, and the author feels there is value in a more thorough exploration of the fundamental flow physics and local heat transfer behavior. A solid foundational approach that focuses on simple flows, consistent reference values, and repeatability is needed.

2.1. sCO_2 Brayton Cycle

Supercritical carbon dioxide has been proposed as a working fluid in a number of advanced thermodynamic cycles for power generation (Ahn, 2015). Indirectly heated cycles have been proposed, with sources including geo-thermal, solar-thermal, nuclear and coal. It is well-known that these cycle thermal efficiencies approach the Carnot efficiency with increasing TIT (Çengel, 2011). Recently, sCO_2 cycles involving oxy-combustion inside the carbon dioxide medium have been proposed. These cycles feature TIT approaching 1200° C and thermal efficiency approaching 65%. A distribution comparing the performance of several proposed cycles is presented in Figure 2.1.

There are many advantages to the use of sCO_2 in a thermodynamic cycle. The cycle enjoys an increase in compressor performance when compared to a gas Brayton cycle, as less work is required to raise the pressure of the less compressible fluid. Compressibility factor, Z, refers to the ratio of specific volume of a fluid to that of an ideal gas. When Z is unity, behavior approximates an ideal gas, and it tends toward incompressibility when Z approaches zero.

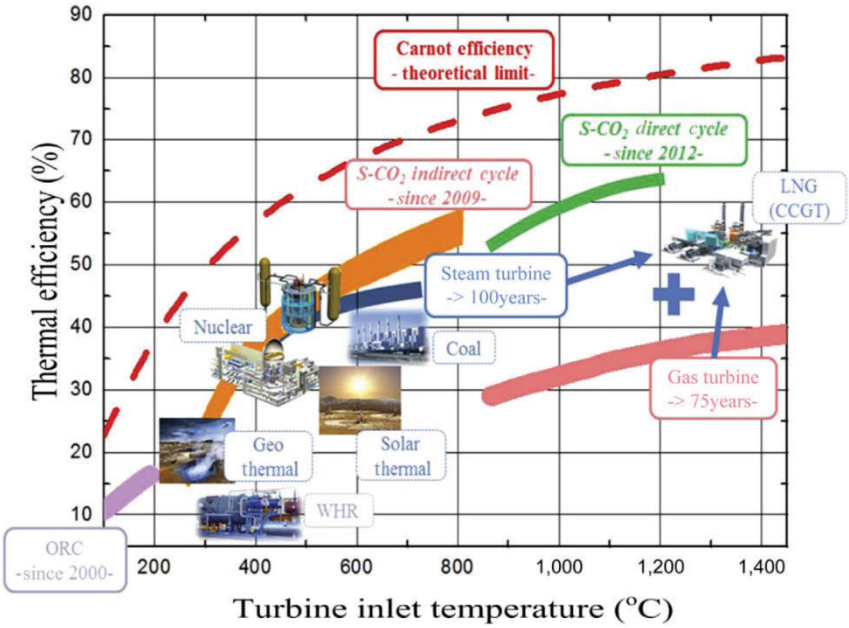

Figure 2.1 Thermal efficiency vs. TIT: traditional and sCO_2 power cycles (Ahn, 2015)

Compressibility factor is defined in Equation 7:

$$Z = \frac{Pv}{RT} \tag{7}$$

Where Z is the compressibility factor, P is the static pressure, v is the specific volume, R is the specific gas constant, and T is the static temperature.

Approaching the critical point, real fluid effects are important and sCO_2 compressibility factor lies between 0.2 – 0.5, allowing easier compression than in a traditional gas turbine cycle. As the minimum operating pressure (at compressor inlet) is relatively high in a sCO_2 cycle, the fluid is very dense at all stations in the flow. This manifests in a higher specific power output and can permit turbomachinery upwards of 10 times smaller than an equivalent steam Rankine cycle, and with a smaller footprint. Additionally, carbon dioxide is less corrosive at typical TITs than steam, which allows for either higher TITs or use of a wider range of turbine materials. In a steam Rankine

cycle, high efficiencies are possible because the cycle operates across the vapor dome, and the working fluid is compressed as a liquid, requiring less power. Gas Brayton cycles can enjoy high efficiencies on account of their large turbine inlet temperatures but suffer due to large power requirements from their compressors. Figure 2.2 compares these condensing and non-condensing cycles in a temperature-entropy diagram.

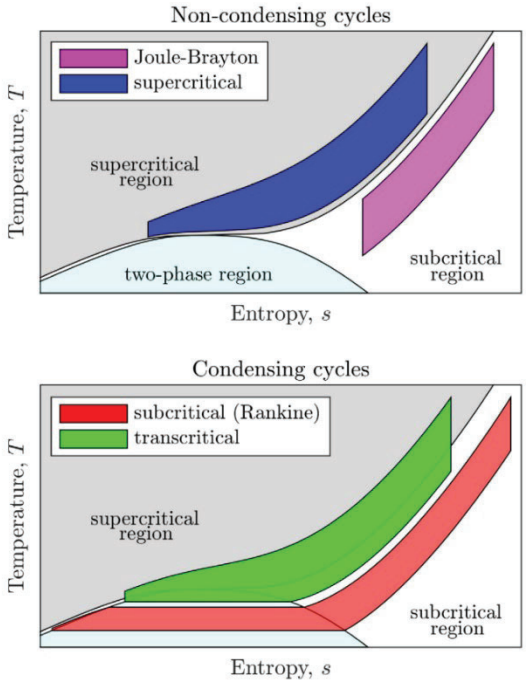

Figure 2.2 Power cycle classification (White, 2021)

A direct-fired sCO_2 Brayton cycle, a non-condensing cycle operating entirely in the supercritical region and represented by the blue area in the upper diagram, can combine these advantages (Ahn, 2015). A caveat arises, however, from this list of advantages in that a higher overall operating pressure will result in a lower pressure ratio across the turbine. The thermal efficiency of a Brayton cycle is tied to this ratio via the isentropic relations as shown in Equation 8.

$$\eta = 1 - \frac{T_1}{T_2} = 1 - \left(\frac{P_1}{P_2}\right)^{\gamma - 1/\gamma} \quad (8)$$

Where T and P are temperatures and pressures, subscripts 1 and 2 are turbine inlet and outlet, and γ is the ratio of specific heats. Figure 2.3 shows the change in cycle performance with respect to turbine pressure ratio for a typical gas Brayton cycle with air as the working fluid.

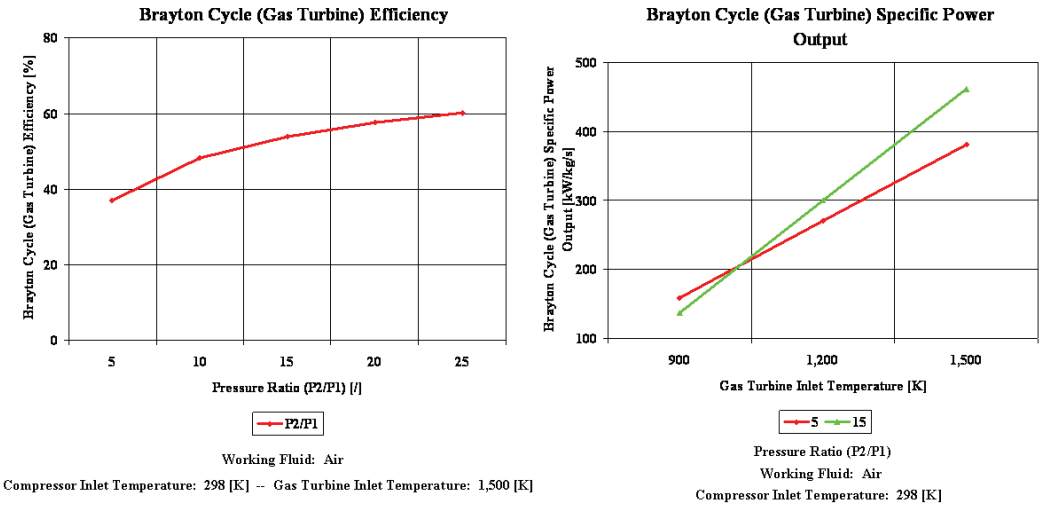

Figure 2.3 Brayton cycle performance with respect to turbine pressure ratio and TIT (Engware, 2006).

Due to increased TIT, and the reduction in total temperature ratio across the turbine in the direct-fired sCO_2 Brayton cycle, more heat needs to be recuperated after expansion to increase thermal efficiency (Ahn, 2015). Effective, low-cost heat exchangers are essential, often in a recompression/recuperator layout, to the development of these cycles. Careful recuperator design will be necessary, as the specific heat of cold side fluid can be two to three times higher than the hot side flow (both sides sCO_2) and the PCHEs most often proposed for this purpose has a large capital cost (as much as 90% of the system)

(White, 2021). Thermal efficiency has also been shown to be sensitive to the recuperation process chosen (Ahn, 2015). There is also a significant need for turbine blade cooling at the higher temperatures seen in direct-fired cycles (Brun, 2014).

2.2. sCO_2 Thermophysical Behavior

Supercritical fluids are not encountered at atmospheric conditions and as such are non-intuitive. For example, they can simultaneously have liquid-like densities and gas-like diffusivities, and a list of other thermodynamic and transport properties become weighted averages between corresponding compressed liquids and superheated gases (Bellan, 2000). Fluid behavior at the critical point becomes more interesting as this point is a thermodynamic singularity: heat capacity, thermal conductivity and isentropic compressibility tend to infinity here.

The pseudocritical line can be interpreted as an extension of the saturation line beyond the critical point. This line is the set of points of temperature where heat capacity is maximum, for a given pressure. These temperatures are known as pseudocritical temperatures and divide the supercritical regime into regions where the fluid may have more liquid-like or more gas-like behavior. While a discrete phase change no longer occurs above the critical temperature and pressure, pseudoboiling is said to occur across the pseudocritical line, and represents a condition where heat addition to the fluid will have minimum effect on temperature change, but maximum effect on specific volume change. Heat transfer enhancements and degradations in supercritical flows are attributed to this behavior. Compressibility and thermal conductivity also have peaks along this line, but no longer tend to infinity and the peaks decrease with increasing distance from the critical point.

As can be seen in Figure 1.5, fluid property changes near the critical point are significant, and in some cases, properties change by orders of magnitude. Therefore, real-fluid behavior must be captured in any experimental data reduction and numerical modeling, particularly when studying heat transfer.

The impact of pseudoboiling on heat transfer enhancement and degradation is manifest in part via buoyancy effects. Pseudoboiling occurs when heat is transferred from a surface to a supercritical fluid below its pseudocritical temperature. Fluid layers close to the surface may rise above the pseudocritical temperature, resulting in a significant increase in specific volume relative to the dense, lower temperature bulk flow. At lower heat fluxes, this low-density near-wall flow may leave the surface in small fluid chunks, similar to the gas bubbles formed from nucleate boiling in conventional two-phase flow. This mass transfer contributes to the overall energy transfer across the surface, and this is referred to as heat transfer enhancement. Conversely, in a cooling flow, if there exists a layer of fluid at the pseudocritical temperature between the wall and bulk temperatures, the peak in thermal conductivity at this temperature can result in a heat transfer enhancement (Cabeza, 2017).

At higher heat fluxes and/or lower mass flow rates, however, a pseudo-film boiling can occur, where a radially static lower density layer of gas-like supercritical fluid, with lower thermal conductivity, prevents contact between the heated surface and the higher density, liquid-like supercritical bulk flow. This is the deteriorated heat transfer regime, and deterioration can be mitigated by increasing turbulence in the flow to promote film layer breakup (Cabeza, 2017). A summary of conditions favorable to, and detrimental to, heat transfer is shown in Figure 2.4.

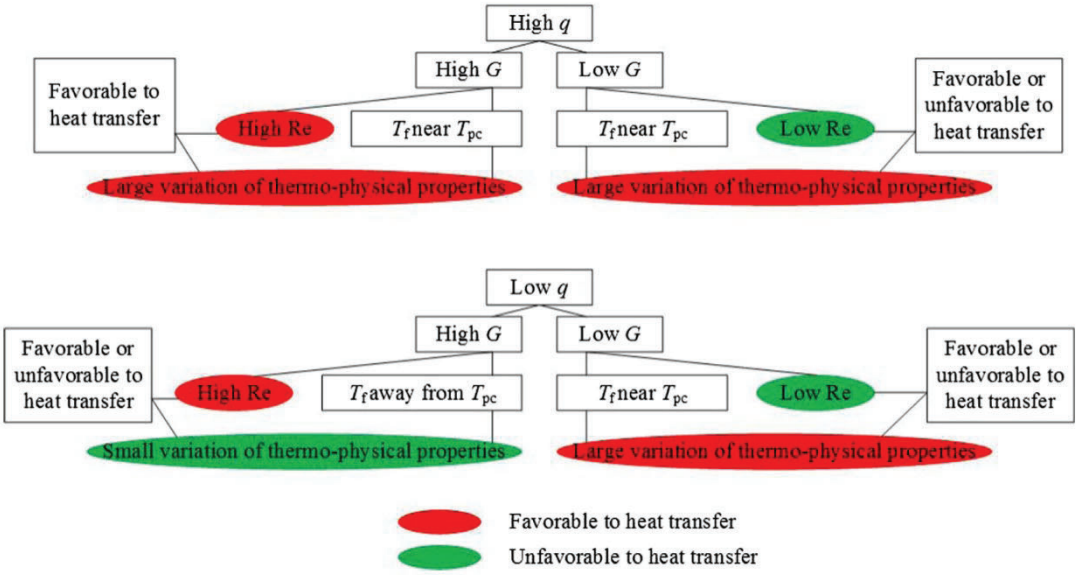

Figure 2.4 Impact of flow parameters on heat transfer (Huang, 2016)

Also relevant to the description of heat transfer behavior in supercritical fluids is the piston effect (Carlès, 2010) where a heat flux causes a thermal wave which drives expansion and compression of the hydrodynamic boundary layer. This process is depicted in Figure 2.5.

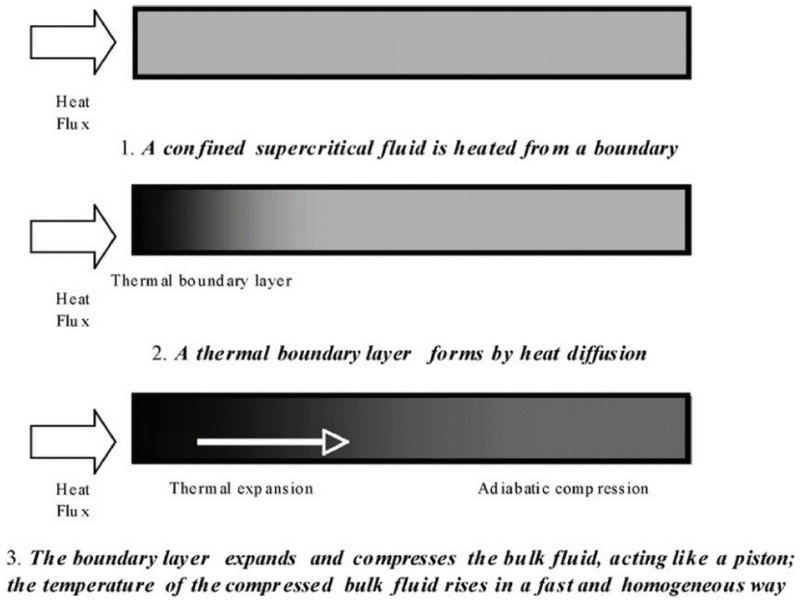

Figure 2.5 Piston effect (Cabeza, 2017)

This mechanism is strongly linked to temperature perturbations in the overall flow. Similarly, density fluctuations are linked to convection or diffusion effects and pressure perturbations are linked to acoustical effects. It is noteworthy however that the time scales associated with these effects are sufficiently different here that they are essentially decoupled for supercritical flows (Cabeza, 2017).

2.3. Semi-Intrusive Temperature Measurement

Current work is being performed with UniTemp, a commercially available TSP from Innovative Scientific Solutions Incorporated (ISSI). This product uses a Ru(bpy) luminophore in a shellac binder. The excitation wavelength is from 380 to 520 nm and emission wavelength is between 500 and 720 nm. Figure 2.6 shows manufacturer data including a calibration curve and spectral behavior.

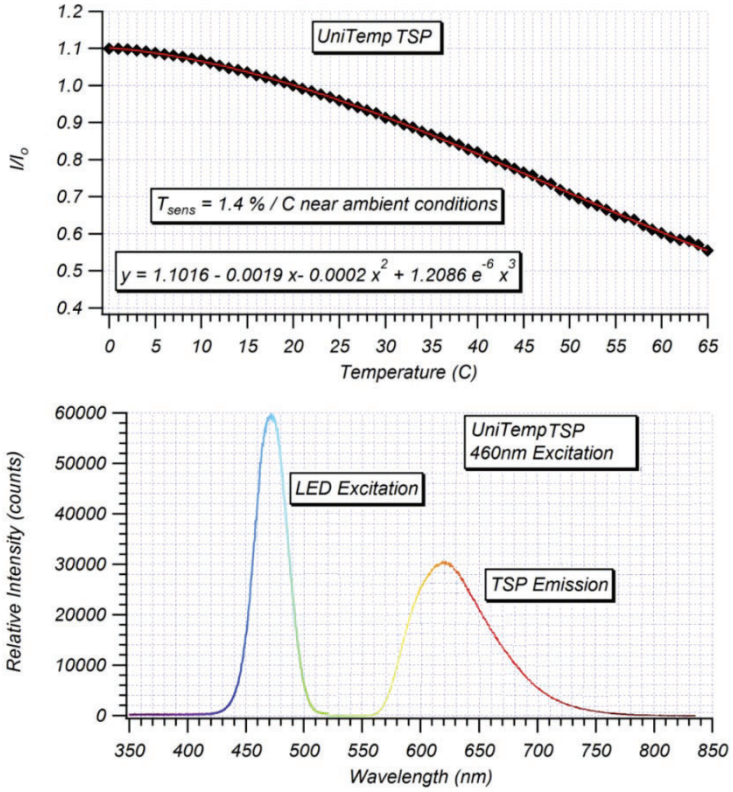

Figure 2.6 UniTemp TSP data (ISSI)

An in-house calibration curve was generated in previous work by this lab (Prasad, 2017) and is used for current work. The use of an intensity ratio as opposed to an absolute brightness can mitigate several sources of error, including non-uniform paint illumination, uneven paint coating, or inadequate mixing of the paint prior to application, which can produce non-homogeneous distribution of luminophores.

Another semi-intrusive technique involves use of thermochromic liquid crystals (TLC). TLCs selectively reflect visible light, with the wavelength of this reflected light a function of crystal temperature (Smith, 2001). The anisotropic nature of the crystals, specifically their optical properties, often requires strict lighting and image capture geometry that is not always feasible in heat transfer experiments. Careful in-situ calibration can be performed, however, to mitigate uncertainty arising from optical anisotropy.

The dominant wavelength of reflected visible light changes monotonically with temperature within a particular temperature range, or bandwidth. Temperature can therefore be evaluated across a surface by measuring this reflected wavelength and comparing with a previously established calibration. High spatial resolution and accuracy can be obtained with this method, similarly to TSP. TLCs are typically prepared to reflect colors spanning the entire visible spectrum for a fixed temperature range. Increasing temperature corresponds to shorter reflected wavelengths: a red color response is seen at the lower temperature limit and blue is seen at the highest temperatures. The crystals appear translucent outside of this temperature bandwidth.

While the performance of this method is high in terms of spatial resolution and temperature measurement, the temperature ranges are restrictive, owing to the physics of

TLCs and the small band of wavelengths that make up the visible spectrum. The widest bandwidth TLC formulations are capable of displaying temperature variations of approximately 20 °C (Smith, 2001). This is likely not suitable for current work, particularly in high heat flux experiments. Figure 2.7 shows the spatial resolution of the TLC technique, allowing flow features such as a von Karman vortex street to be captured.

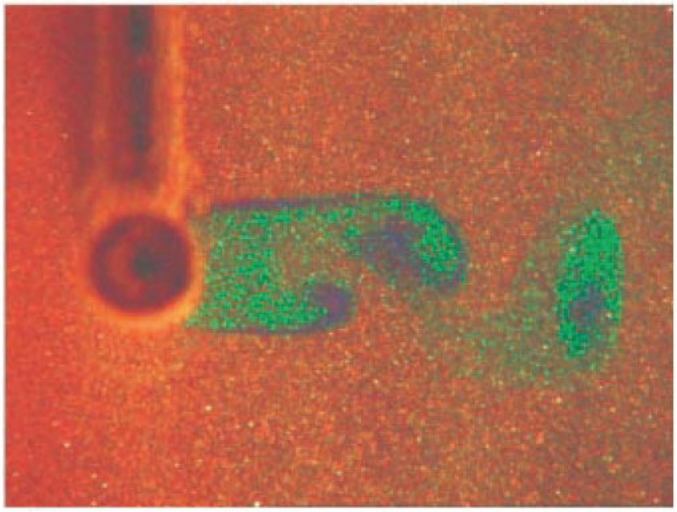

Figure 2.7 TLC measurement of a cylinder in crossflow (Smith, 2001)

Infrared photography (IR) is a widely used non-intrusive technique in the heat transfer community (Vollmer, 2018). While highly applicable and useful for heat transfer experiments in air, CO_2 has unique spectral transmissivity behavior in the infrared, with dips around 2.7, 4.3 and 15 μm, as shown in Figure 2.8.

A significant portion of the emitted power in proposed experimental temperature ranges is transmitted in these bandwidths. The spectral behavior of the working fluid in the proposed work is expected to unduly contribute to experimental error should IR imaging be used, so this non-intrusive technique is not considered for current work.

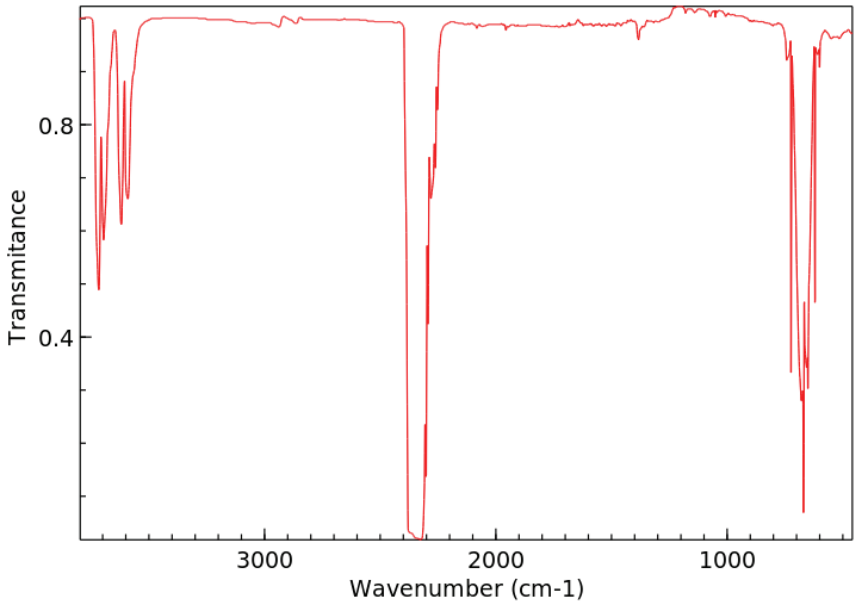

Figure 2.8 CO_2 spectral transmissivity (NIST Webbook)

2.4. Experiments in sCO_2 Heat Transfer

Many experiments in sCO_2 heat transfer concern the adaptation or replacement of well-established semi-empirical Nusselt number correlations (such as Dittus-Boelter) common in air and sub-critical fluids. This work is performed to account for the significant variations in thermodynamic and transport properties in the near-critical region (Cabeza, 2017). Such efforts date back to the late 1950s (Bringer, 1957) and primarily investigate mixed and forced convection flows in horizontal and vertical circular tubes. New correlations have been developed for specific flow geometries and within certain Reynolds number and mass and heat flux regimes over the decades (Krasnoshchekov, 1969; Baskov, 1977; Petrov, 1985; Fang, 1999; Pitla, 2002; Yoon, 2003; Son, 2006; Oh, 2010; Jackson, 2002; Dang, 2007; Huai, 2007; Kuang, 2008; Lee, 2013; Gupta, 2013; Preda, 2012; Saltanov, 2015; Liao, 2002; Kim, 2008; Simões, 2008; Bruch, 2009).

These studies take varying approaches to calculating heat transfer quantities that are functions of fluid properties, such as where to evaluate specific heat capacity, thermal conductivity, density, or viscosity, as all these quantities will have strong gradients in the flow. Some correlations use fluid properties evaluated at bulk temperature while others employ pseudocritical temperature, as well as ratios of properties at wall and bulk temperatures. The effect of buoyancy was found significant in nominally forced convection regimes in most heat transfer coefficient predictions, with this effect increasing with higher heat flux (Cabeza, 2017). All temperature measurements in the aforementioned research have been obtained using thermocouples or resistance temperature detectors (RTDs) and use of spatially averaged data is still prevalent. To develop increasingly useful heat transfer correlations applicable to a wider range of fluxes and Reynolds numbers, local data with high spatial resolution is needed. To this end, a method of continuous temperature measurement is desired.

Bourke et al. (1970) measure wall temperatures in vertically upward and downward flows of transcritical and supercritical CO_2 in a circular tube. The impact of sub- to supercritical inlet conditions is investigated, as well as the heat transfer effects of buoyancy when flow direction is reversed relative to the direction of buoyancy forces. Further, a range of operating pressures and heat fluxes are tested. Heat transfer coefficients are found to deviate from previously observed flows of gaseous or liquid CO_2 by factors of 2-10. Comparisons are made with a single phase Nusselt number correlation by Colburn. Significant heat transfer enhancement is found in the critical region for both upward and downward flows. Local increases in wall temperature are observed at higher heat fluxes in upward flow. At low mass flow rate, local wall

temperature peaks occur at some heat flux levels, indicating an unsteady buoyancy effect on heat transfer. All enhancement effects are seen to decay with increasing operating pressure, above and below the critical point.

Adebiyi and Hall (1976) contribute an often-cited experiment on a heated flow of sub- and supercritical CO_2 in a large horizontal tube. Wall temperatures of a uniformly heated pipe are taken over a range of inlet Reynolds numbers. The authors report a significant variation of temperatures around the circumference of the pipe, indicating a strong buoyancy effect. Heat transfer enhancement at the bottom of the pipe and degradation at the top of the pipe arise from this phenomenon. The authors present two previously established criteria for flows for which buoyancy effects can be excluded; the criteria are presented as inequalities 9 and 10.

$$\mathrm{Gr_b Re_b^{-2}} \left(\frac{\rho_\mathrm{b}}{\rho_\mathrm{w}}\right) \left(\frac{x}{D}\right)^2 < 10 \tag{9}$$

$$\mathrm{Gr_b^* Re_b^{-2.75} Pr_b^{-0.5}} \left[1 + 2.4\mathrm{Re_b^{-\frac{1}{8}}} \left(\mathrm{Pr_b^{\frac{2}{3}}} - 1\right)\right]^{-1} < 3 \times 10^{-5} \tag{10}$$

Where Gr is the Grashof number, Re is the Reynolds number, Pr is the Prandtl number, ρ is density, D is the tube diameter, and subscripts b and w refer to properties taken at bulk and wall temperatures, respectively. The Grashof number is generally defined for pipes as:

$$\mathrm{Gr} = \frac{g\beta(T_\mathrm{w} - T_\mathrm{b})D^3}{\nu^2} \tag{11}$$

Where g is the acceleration due to gravity, β is the thermal expansion coefficient, D is the pipe diameter, and ν is the kinematic viscosity. The strong fluid property variation in the radial direction raises the question of where to define the thermal expansion

coefficient or kinematic viscosity. The modified Grashof number Gr^* in inequality 10 addresses this with the following modification:

$$\mathrm{Gr}_\mathrm{b}^* = \frac{\rho_\mathrm{b} - \rho_\mathrm{w}}{\rho_\mathrm{b}} \frac{gD^4}{\nu_\mathrm{b}^2 k_\mathrm{b}} \frac{q_\mathrm{w}}{T_\mathrm{w} - T_\mathrm{b}} \tag{12}$$

The criterion described by inequality (10) assumes a fully developed mixed convection flow and does not include a streamwise location argument. The flows reported here in general exceed the criteria set forth by both inequalities and measured buoyancy effects support their assertion. Some data however show that the impact of the buoyancy effect was still developing after 100 diameters of heated length for some Reynolds numbers. The authors note a lack of clarity in the literature concerning a distinction between thermally fully developed forced convection flows and flows for which a temperature distribution indicative of significant buoyancy effects is fully developed.

Mokry and Pioro (2011) propose a heat transfer correlation for sCO_2 flowing upward in a smooth circular tube, with an application to nuclear reactor cooling. The reactor in question is to be cooled with supercritical water but owing to the expense of experiments at conditions supercritical relative to water, current work is performed on carbon dioxide, which has a more convenient critical point. The experiment was conducted at a range of operating pressures, mass fluxes, heat fluxes, and inlet temperatures. The authors present the template upon which heat transfer correlations are developed, shown in Equation 13.

$$y = C_0 t_1^{C_1} t_2^{C_2} \ldots t_\mathrm{n}^{C_\mathrm{n}} \tag{13}$$

Where C_0 is a constant of proportionality, t_n represents various parameters relevant to heat transfer, and C_n represents exponents used in the curve fit. The Mokry and Pioro correlation assumed the form shown in Equation 14.

$$\mathrm{Nu} = C_0 \mathrm{Re}^{C_1} \overline{\mathrm{Pr}}^{C_2} \left(\frac{\rho_\mathrm{w}}{\rho_\mathrm{b}}\right)^{C_3} \tag{14}$$

A ratio of the densities at wall and bulk temperatures captures, in part, the effect of strong radial gradients in thermophysical properties. Liu et al. (2014) conduct an experiment on a cooled sCO_2 flow in three horizontal tubes of varying diameter. A variety of mass flow rates and inlet conditions were studied for their impact on heat transfer coefficient and pressure drop. Tube diameter was found to have a significant impact on heat transfer, and a new Nusselt number correlation is proposed for large diameter tubes. This correlation is based on the Dittus-Boelter correlation with additional terms to account for the variable thermophysical properties and is shown as Equation 15.

$$\mathrm{Nu}_\mathrm{w} = 0.01\, \mathrm{Re}_\mathrm{w}^{0.9}\, \mathrm{Pr}_\mathrm{w}^{0.5} \left(\frac{\rho_\mathrm{w}}{\rho_\mathrm{b}}\right)^{0.906} \left(\frac{c_{p,\mathrm{w}}}{c_{p,\mathrm{b}}}\right)^{-0.585} \tag{15}$$

Where c_p is specific heat at constant pressure. Maximum heat transfer is seen where bulk temperature approaches the pseudocritical temperature. Pressure drop is observed to decrease along the flow path, as the cooler fluid downstream is at a significantly higher density and thus lower flow velocity. Large discrepancies between previously established correlations and experimental data are observed, but the maximum error of this new correlation is reported as ± 15%.

Tanimizu and Sadr (2016) study heat transfer behavior of sCO_2 flow in a horizontal pipe at a range of heat fluxes, mass flow rates, operating pressures, and inlet temperatures. Results are compared with the Dittus-Boelter correlation and three buoyancy parameters are evaluated for suitability to test conditions. While strong buoyancy effects are seen in the flow, neither trends nor absolute values of the tested parameters agree with measured heat transfer enhancement and deterioration in this

experiment. The two flow conditions considered in Adebiyi and Hall (1976) are considered along with a simpler version of the form:

$$\mathrm{Bu_c} = \frac{\mathrm{Gr_b}}{\mathrm{Re_b^2}} \ll 10^{-3} \tag{16}$$

Where $\mathrm{Bu_c}$ is the variable to which this buoyancy parameter is assigned. Results from this experiment show a general overprediction of heat transfer from the traditional correlations for all flows near the pseudocritical temperature, owing to thermophysical property change. Over predictions were also noted at flow conditions well away from the pseudocritical line and this is attributed to buoyancy and fluid acceleration effects. The authors dispute the usefulness of the more sophisticated buoyancy parameters, as all three tested parameters showed different trends and magnitudes along the length of the test section. Neither of these were able to better characterize the significance of buoyancy effects as that shown in inequality (16).

Zhu et al. (2019) introduce a novel parameter to the study of supercritical fluid heat transfer with a supercritical boiling number, as a way of predicting heat transfer deterioration associated with pseudoboiling. A boiling number in two-phase flow is traditionally described as the ratio of heat flux to the flux required to fully convert all liquid to vapor (Thome, 2006):

$$\mathrm{Bo} = \frac{q}{\dot{m} h_{\mathrm{lg}}} \tag{17}$$

Where Bo is the boiling number and h_{lg} is the latent heat of vaporization. The parameter suggested in this work extends this along the saturation line, through the critical point, to the pseudocritical line:

$$\mathrm{SBO} = \frac{q_{\mathrm{w}}}{G h_{\mathrm{pc}}} \tag{18}$$

Where G is the mass flux and h_{pc} is the fluid enthalpy taken at pseudocritical temperature. This fluid enthalpy will be a local maximum but not arbitrarily large as is that case at the critical point. This peak decays as the operating pressure in the flow increases into the supercritical region. SBO can be employed as a metric to estimate density ratio in the flow relative to liquid-like and vapor-like fluid at a given operating pressure, and in that way determine the relative strengths of convective forces and momentum contribution from rapid fluid expansion (pseudoboiling). A range of operating pressures and mass fluxes are tested in a horizontal tube at constant heat flux in a cooling configuration. Heat transfer deterioration is noted at a particular SBO value, with this value determined by a departure (overshoot) from expected wall values from established correlations.

2.5. Numerical Work in sCO_2 Heat Transfer

Zhang and Yamaguchi (2007) perform a numerical analysis of a laminar horizontal pipe flow experiment with forced convection in a solar collector. An in-house unsteady finite volume code using a segregated pressure solver is used. Real fluid properties were obtained using piecewise polynomial functions of temperature at the operating pressure of 8.0 MPa. Significant variations in fluid thermophysical properties are seen radially. Heat transfer enhancement and superior heat transfer performance relative to water is reported for the heat flux range of 100 – 800 W/m^2 and Reynolds number range of 210 – 1800. The authors attribute this behavior to a thinner boundary layer (larger radial temperature gradient) relative to a water flow, and a reduced viscosity. The flow does not fully develop hydraulically or thermally in the computational domain, and this also

fosters heat transfer performance. Large heat capacities are also reported, further increasing heat transfer.

Suo-Antilla and Wright (2011) adapt an existing commercial CFD code to use with real fluids. C3D is a finite volume LES code nominally used to simulate fires and combustion. Density may vary by a factor of 4 or 5 in a short distance in fire simulations, as it does in many sCO_2 flows, and the code is well-suited to this. Real fluid property data is implemented into the code using the NIST REFPROP library, while the code is modified slightly to use an enthalpy formulation instead of the existing internal energy formulation, to avoid numerical instabilities associated with the peaks in specific heat capacities near the critical point. The code is applied to flows related to nuclear reactor cooling and demonstrates good agreement with experimental data, showing promise for its predictive ability for forced and natural convection problems.

Ameli et al. (2017) study numerically the impact of the accuracy of a real gas model on performance of a centrifugal compressor in a sCO_2 Brayton cycle. A lookup table is used to provide real fluid data near the critical point and the effect of temperature and pressure point resolution on compressor behavior is investigated. Several boundary conditions and compressor operating conditions are also studied. Compressor efficiency is shown to be very sensitive to the resolution of the tabular fluid property data. REFPROP data was again used, which itself employs the Span and Wagner (SW) equation of state (Span, 1996), specifically intended for carbon dioxide, and use in near critical point applications. Instabilities arise however with increased table resolution: the SW EoS cannot calculate densities arbitrarily close to the critical point, frustrating table refinement.

A conflicting problem arises as the code used in this study interpolates tabular data using a trilinear method, which can lead to numerical instabilities if there are large value changes between adjacent table entries. These instabilities can eventually lead to simulation divergence. This encourages table refinement. Figure 2.9 shows the significant impact of refining table resolution on the flow field around an impeller blade. Mach contours and velocity vectors are shown for a flow solution first using 100 temperature and 100 pressure data points, and another with 3 times this resolution. The same temperature and pressure bounds are used in both cases.

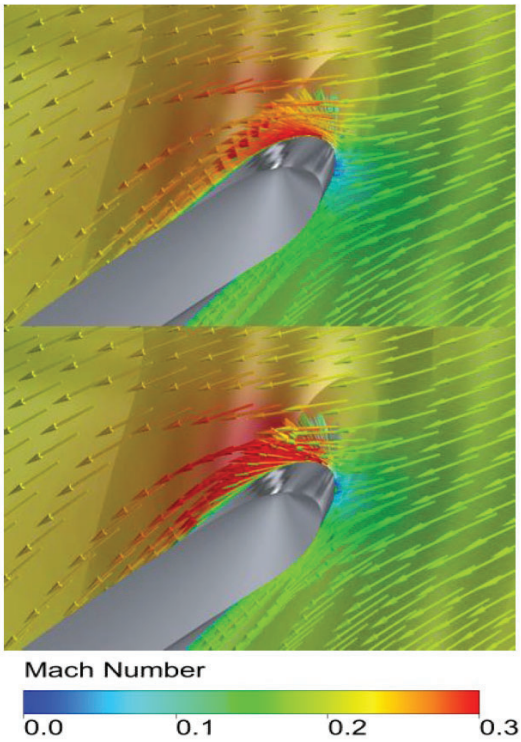

Figure 2.9 Compressor impeller flowfield (Ameli, 2017)

Wang et al. (2018) bring four RANS turbulence models to bear in a finite volume CFD code on a cooling flow of sCO_2 in horizontal tubes of three diameters. NIST fluid property data is used. Four k-ε models are compared: Re-Normalization Group (RNG), Launder and Sharma (LS), Yang and Shih (YS), and Abe, Kondoh and Nagano (AKN).

The AKN model is shown to agree best with experiment. The effect on heat transfer of heat flux, tube diameter and buoyancy is investigated. At bulk temperatures above pseudocritical (at the operating pressure of 8.0 MPa), heat transfer enhancement is observed with increasing heat flux and increasing tube diameter. At bulk temperatures below pseudocritical, these effects are not seen. Additionally, buoyancy effects on heat transfer enhancement are reported as minimal in tubes with relatively large diameter.

Jiang et al. (2018) assert that the ability of RANS turbulence models to predict buoyancy effects is hindered by the strong variations in thermophysical properties near the pseudocritical line. The authors develop a computational method that accounts for the anisotropy in turbulent heat flux to apply a correction for the buoyancy effect in the heat transfer to supercritical flows. This method captures the buoyancy effect's production of turbulent kinetic energy and includes a turbulent Prandtl number model that captures turbulent heat flux. These modifications are made to an existing AKN k-ε turbulence model in Ansys Fluent 13.0 and its performance in predicting heat transfer deterioration is validated against experimental and DNS data. Accurate prediction is attributed to the model's ability to synthesize the relationship between heat transfer deterioration and recovery and accurate calculation of turbulent kinetic energy. Results are found sensitive to turbulent Prandtl number.

Wang et al. (2019) propose a heat transfer correlation derived from numerical simulation of a cooling flow in large horizontal tubes. A set of simulations based on the experiment by Adebiyi and Hall investigated the effect of turbulence model selection, tube diameter, mass flux, heat flux and operating pressure. The AKN k-ε model again shows superior predictive ability. The authors report a significant departure from

established Nusselt number correlations and develop a new correlation suited to near-wall film layers of sCO_2 based on Gnielinski's formulation (Gnielinski, 1975) but also capturing the effect of density ratio between near-wall and bulk flows. Use of the modified correlation provides increased accuracy to the experimental data for the complete range of bulk temperatures tested, but discrepancies remain at bulk temperatures very near the pseudocritical temperature.

Li et al. (2019) present a RANS simulation of sCO_2 heat transfer in a tube with novel cross section. NIST REFPROP data is again used in Ansys Fluent with Menter's k-ω Shear Stress Transport (SST) turbulence model. The ability of the turbulence model to resolve any buoyancy effects on heat transfer was validated against experimental data on a standard horizontal circular tube and showed good agreement. A parametric study at constant initial and boundary conditions was performed for geometric quantities associated with the cylindrically concave and fillet features of the tube. Results indicate an improvement in heat transfer (even near a pseudocritical bulk temperature) and no reported increase in friction factor.

2.6. Problem Statement and Hypothesis

The body of literature on gas turbine thermal management and flows in large and compact heat exchangers is certainly expansive. There also exists a large number of studies on heat transfer behavior in sCO_2, both in simple geometries and in advanced heat transfer devices. This work almost exclusively deals with global or streamwise varying heat transfer rates. Selected studies do provide local data; however, this has been constrained to numerical simulations. The impact of the fluid property variations near the critical point has been historically accounted for by the modification of existing

correlations, such as Dittus-Boelter or Gnielinski. Due to a lack of empirical data, it is not yet known how accurate numerical predictions on local coefficients are.

The literature gap lies both in an incomplete characterization of the fundamental flow physics, leading to a more complete understanding of the local heat transfer behavior, and in the various data reduction and non-dimensionalization methods being employed. Challenges lie in accurate and stable modeling of near-critical flows due to their rapidly changing thermodynamic and transport properties (large density gradients being the biggest offender) and experimental uncertainties along the pseudocritical line, where large property gradients are also observed.

Problem statement: a significant amount of highly spatially resolved heat transfer data has yet to be obtained in supercritical flows and the impact of local variations is therefore unknown. Also, data reduction methodology is not standardized in the supercritical fluid heat transfer community. Further, there is a lack of in-house experimental validation of numerical methods.

The hypothesis of this work lies in the value contained in obtaining more spatially resolved temperature and heat transfer data and modeling flow physics in simple heat transfer flows. This foundational approach has the potential to greatly benefit the heat transfer community by elucidating trends and potentially providing heat transfer correlations that are agnostic to changes in heat or mass flux, flow geometries, or proximity to the critical point. A more complete characterization of this behavior will enable advanced designs of power generation and propulsion technologies (and in other industries), especially applications such as heat exchangers and recuperators that rely on the flow and heat transfer of supercritical fluids. Results from this work will equip

designers with critical data currently missing from heat transfer literature and be of general use to the heat transfer community.

To achieve this objective, several smaller objectives have been established. Each of these objectives are tied to a specific task in the research plan and contribute to the overall success of the research.

- Adapt and implement a verified, semi-intrusive temperature measurement technique (TSP) for use in a supercritical environment.
    - Achievement of this objective establishes the measurement technique details to be utilized for a future experimental campaign. Confirmation of the expected accuracy, repeatability, and degradation rates will be quantified and compared to existing gas phase data.
- Assess the applicability of modern commercially available computational codes in analyzing sCO_2 heat transfer.
    - A robust benchmarking effort ascertains the ability of commercial Reynolds-Averaged Navier-Stokes (RANS) CFD codes to reproduce experimental and previous numerical results from literature, using straight-forward heat transfer problems in simplified geometries.
    - Achievement of this objective provides insight into the capability of modern design tools and identify necessary model improvements and opportunities.
- Conduct expanded CFD campaign accompanying experimental work on sCO_2 heat transfer.
    - The verified numerical method is adapted and extended to flow conditions

and geometries relevant to work.

  - Achievement of this objective will allow in-house verification of CFD predictive ability with experiment and further elucidate the unique flow features in this thermodynamic regime.

- Implement a reduced-order numerical model for optimization of sCO_2 heat transfer along the pseudocritical line.
  - A one-dimensional code is compared to validated CFD results to assess the capability of reduced order methods and to harness the unique variable fluid properties in the pseudocritical region.
  - Achievement of this objective will determine whether simplified (more computationally tractable) models using real fluid properties can maintain fidelity to higher-order methods and investigate optimization through pseudoboiling.
- Perform an uncertainty analysis in the near-critical region to assess the propagation to fluid properties and heat transfer correlations using a root-sum-square (RSS) method.
  - Achievement of this objective will add valuable context to research being performed on flows near the critical point and suggests an alternate approach to developing correlations in this region may be appropriate.

3. Methodology

This study uses experimental apparatus and a variety of computational setups, including a simple horizontal pipe and a pin fin array. Experimental and numerical methodology and associated data reduction for the various investigations is presented below.

3.1. Semi-Intrusive Temperature Measurement

The applicability of a commercially supplied (TSP) consisting of organic luminophores in a shellac binder was first investigated in a simple experiment. Two coupons of TSP-coated acrylic were prepared, and one was subjected to an environment of quiescent sCO_2 for a four-hour period, simulating the proposed initial test conditions. A small quantity of dry ice was weighed and placed in a pressure vessel along with the coupon. The vessel was sealed, the dry ice was allowed to fully sublimate, and pressure was monitored as the contents reached room temperature. The vessel was held above the CO_2 critical point (304.13 K, 7.38 MPa) for 4 hours, and then depressurized. The vessel and apparatus are seen in Figure 3.1.

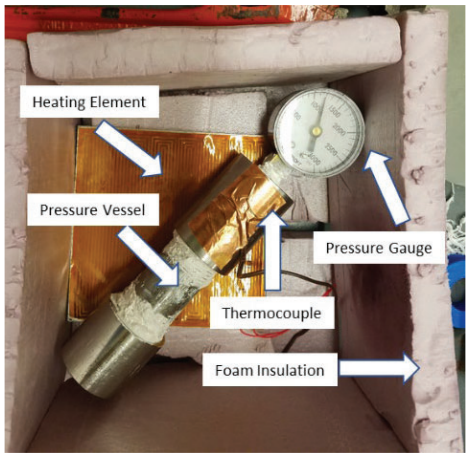

Figure 3.1 Feasibility pressurization setup

Subsequent work was performed with a larger device with facility for continuous TSP imaging and built-in heating and temperature measurement. The entire experimental apparatus consists of a source of very high-pressure carbon dioxide, a pressure vessel with sight glass for TSP coupon viewing, a UV light source and scientific-grade CMOS camera with data acquisition equipment. The apparatus is seen in Figure 3.2.

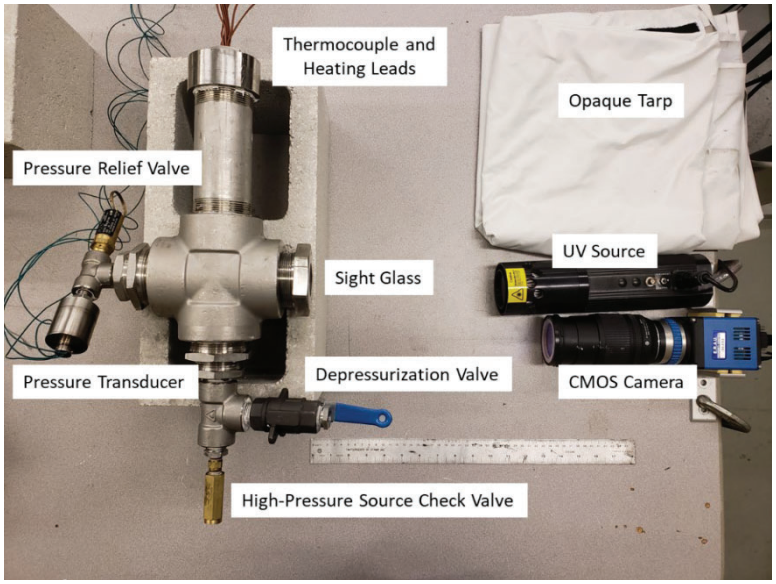

Figure 3.2 TSP testing apparatus

TSP coupons were prepared on aluminum backing. This prevents any ingress of supercritical fluid into the coupon material, results of which are shown below. A coupon was inserted into the pressure vessel by removing and replacing the sight glass. A reference image was taken of the coupon in air at laboratory conditions. Next, high-pressure CO_2 was fed into the device from a nominally 2000 psi supply and was allowed to return to room temperature. A second reference image was taken with the pressure vessel filled with high-pressure, room temperature CO_2 gas. Additional CO_2 was added to the pressure vessel, sufficient to reach supercritical conditions. Heat was then added by

an AC heating element wrapped around the outer surface of the pressure vessel, bringing the fluid above the critical point. Temperature was measured by two thermocouples in the flow and two fixed to the coupon, ensuring the fluid was homogeneous, steady, and supercritical. The apparatus was covered with a polystyrene insulation enclosure for thermal isolation and shielded from ambient light with an opaque tarp. The TSP was excited by the UV light source and images were taken with the CMOS camera, correlated with simultaneous measurements from the thermocouples and pressure transducer. This procedure was performed for 8 prepared TSP coupons at thermodynamic states in the supercritical region, variously close to the critical point.

The aim is to evaluate the suitability of TSP as a semi-intrusive temperature measurement technique for sCO_2 flows and characterize and quantify the deviations in its response with respect to that well-documented in subcritical flows. Any changes to the TSP calibration curve and differences in the product's hysteresis in this flow regime are of interest. The TSP formulation tested is a commercial solution from Innovative Scientific Solutions, Inc. It utilizes a Ru(bpy) luminescent probe and a Shellac binder (ISSI, 2017).

To investigate the interaction between the sCO_2 and TSP, a protective coating was applied to select coupons. This coating must be thin, so as not to impose a significant temperature drop under expected heat flux conditions in future tests, and it must be water-based, so as not to interfere with the TSP basecoat. A commercially available sprayable clear, water-soluble polyurethane coating was used here. Additionally, the effect of reference image condition was investigated to determine the impact of transmission medium (air vs. carbon dioxide) and thermodynamic state (subcritical vs.

supercritical) on the TSP calibration curve. Reference images were taken with the pressure vessel in air at lab conditions, in subcritical CO_2 gas, and in supercritical CO_2, at known temperatures.

3.1.1. TSP Data Reduction

Images of excited TSP coupons were taken with a PCO pco.edge 4.2 scientific-grade CMOS camera in grayscale. Several images (generally 4) are taken, imported into a MATLAB code as arrays, and averaged. The standard practice is a "data image" at an unknown temperature is compared to a "reference image" at a known temperature. The unknown temperature is obtained by calculating the ratio of the average image intensities of the data image to the reference image. This intensity is defined as the mean grayscale value of all image pixels. The intensity ratio is the input to an established calibration curve. The calibration curve used here was developed in-house for a specific batch of TSP and is shown in Figure 3.3.

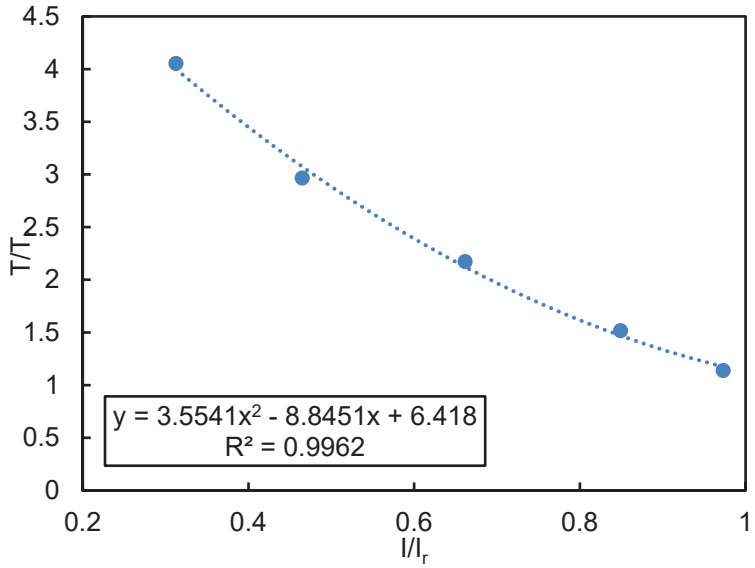

Figure 3.3 Current TSP calibration curve (Prasad, 2017)

A typical TSP data image is shown in Figure 3.4. In many cases below, a subset of

the available image data is selected manually to mitigate sources of error such as reflections of the excitation light source in the sight glass, or the shadow cast by the sight glass housing.

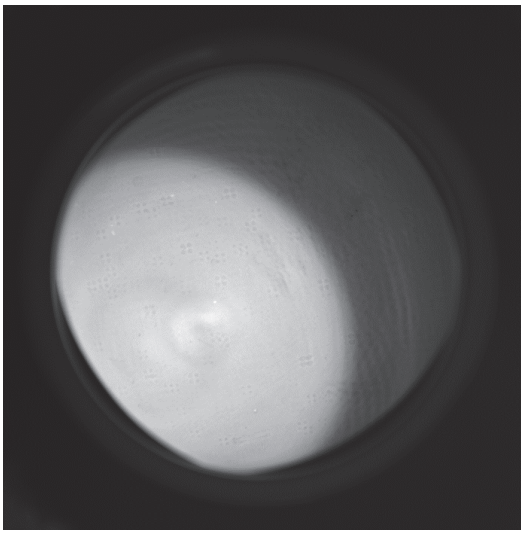

Figure 3.4 Raw image: illuminated TSP seen through sightglass

3.2. CFD Benchmarking

Validation was performed to determine the ability to accurately simulate heat transfer to sCO_2 with commercially available CFD codes, using real fluid properties. Results were compared with an experiment involving a cooled flow of sCO_2 in a horizontal pipe by Dang and Hihara (2004) and also a previous benchmarking effort by Yong Li et al. (2019). The experimental test section configuration is shown in Figure 3.5.

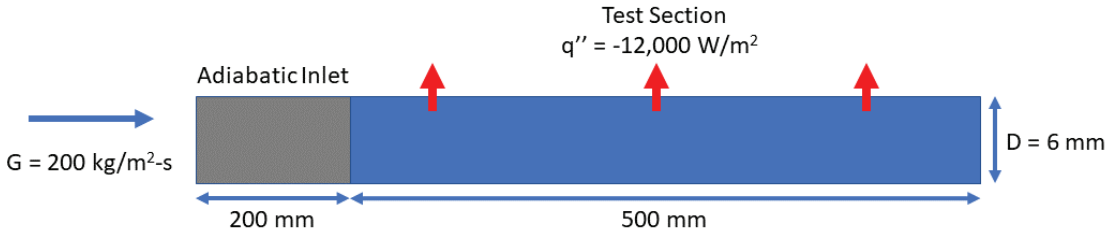

Figure 3.5 Test section configuration (Dang, 2004)

In the experiment, HTC was calculated according to Equation 19:

$$\mathrm{HTC} = \frac{q''_{\mathrm{w}}}{\mathrm{LMTD}_{\mathrm{w}}} \tag{19}$$

Where HTC is heat transfer coefficient, q''_w is heat flux, and LMTD_w is a log-mean temperature difference calculated obtained from:

$$\mathrm{LMTD}_{\mathrm{w}} = \frac{(T_1 - T_{\mathrm{w1}}) - (T_2 - T_{\mathrm{w2}})}{\ln\left(\frac{T_1 - T_{\mathrm{w1}}}{T_2 - T_{\mathrm{w2}}}\right)} \tag{20}$$

Where T_1 and T_2 are CO_2 bulk temperatures taken by Type-T thermocouples calibrated to ± 0.1 K at test section inlet and outlet, and T_{w1} and T_{w2} are wall temperatures at the same locations, using outside wall temperatures taken by thermocouples soldered into the pipe wall (at 3 o'clock and/or 9 o'clock positions), with inside wall temperatures calculated using one-dimensional heat conduction.

Li et al. (2019) calculate HTC according to a different method for their CFD benchmarking:

$$\mathrm{HTC} = \frac{q''_{\mathrm{w}}}{\overline{T}_{\mathrm{b}} - T_{\mathrm{w,in}}} \tag{21}$$

Where $\overline{T}_{\mathrm{b}}$ is a mean CO_2 bulk temperature, taken as the arithmetic mean of inlet and outlet bulk temperatures, themselves mass-averaged quantities:

$$\overline{T}_{\mathrm{b}} = \frac{\overline{T}_{\mathrm{b,in}} + \overline{T}_{\mathrm{b,out}}}{2} = \frac{\frac{\int_{A,\mathrm{in}} c_p \rho u T \,\mathrm{d}A}{\int_{A,\mathrm{in}} c_p \rho u \,\mathrm{d}A} + \frac{\int_{A,\mathrm{out}} c_p \rho u T \,\mathrm{d}A}{\int_{A,\mathrm{out}} c_p \rho u \,\mathrm{d}A}}{2} \tag{22}$$

Where c_p, ρ, and u are the local specific heat, density, and fluid velocities taken at inlet and outlet. The temperature of the inner wall, $T_{\mathrm{w,in}}$ is taken as the arithmetic mean of the temperature along the test section at 10 evenly spaced locations:

$$T_{\mathrm{w,in}} = \frac{\sum_{j=1}^{10} T_{\mathrm{w,j}}}{10} \tag{23}$$

Numerical simulations were performed in Siemens STAR-CCM+ v15 using a Reynolds-Averaged Navier-Stokes (RANS) code. Real fluid properties for the supercritical CO_2 were obtained from NIST REFPROP and used in lookup tables. The CFD benchmarking consisted of a series of three-dimensional steady RANS simulations using Menter's k-ω SST turbulence closure (Menter, 1994) and a density-based solver. The governing equations are shown here in differential form.

Continuity:

$$\frac{\partial \rho}{\partial t} + \nabla \cdot (\rho \boldsymbol{v}) = 0 \tag{24}$$

Where ρ is fluid density and $\boldsymbol{v}$ is the velocity vector.

Conservation of momentum:

$$\frac{\partial (\rho \boldsymbol{v})}{\partial t} + \nabla \cdot (\rho \boldsymbol{v} \otimes \boldsymbol{v}) = \nabla \cdot \boldsymbol{\sigma} + \boldsymbol{f}_{\mathrm{b}} \tag{25}$$

Where $\boldsymbol{f}_{\mathrm{b}}$ is a resultant body force vector, and $\boldsymbol{\sigma}$ is the stress tensor, which can be expressed as:

$$\boldsymbol{\sigma} = -P\boldsymbol{I} + \boldsymbol{T} \tag{26}$$

Where $\boldsymbol{I}$ is the identity matrix, and $\boldsymbol{T}$ is the viscous stress tensor.

Conservation of energy:

$$\frac{\partial (\rho E)}{\partial t} + \nabla \cdot (\rho E \boldsymbol{v}) = \boldsymbol{f}_{\mathrm{b}} \cdot \boldsymbol{v} + \nabla \cdot (\boldsymbol{v} \cdot \boldsymbol{\sigma}) - \nabla \cdot \boldsymbol{q} + S_E \tag{27}$$

Where E is the total energy per unit mass, $\boldsymbol{q}$ is the heat flux, and S_E is an energy source term. The constitutive relations required for closure of the system are the turbulence model, which couples the stress tensor and the velocity field, and the equation of state.

The k-ω shear stress transport model is used here, which is a two-equation model, one governing kinetic energy, k, and the other the specific dissipation rate ω:

$$\frac{\partial(\rho k)}{\partial t} + \nabla \cdot (\rho k \overline{\boldsymbol{v}}) = \nabla \cdot [(\mu + \sigma_k \mu_t)\nabla k] + P_k - \rho \beta^* f_{\beta^*}(\omega k - \omega_0 k_0) + S_k \tag{28}$$

Where $\overline{\boldsymbol{v}}$ is the mean velocity vector, μ is dynamic viscosity, μ_t is the turbulent viscosity, σ_k and β^* are model coefficients, P_k is the kinetic energy production term, f_{β^*} is a factor applied to free-shear, S_k is a user-defined source term, and k_0 and ω_0 are ambient turbulence values.

$$\frac{\partial(\rho \omega)}{\partial t} + \nabla \cdot (\rho \omega \overline{\boldsymbol{v}}) = \nabla \cdot [(\mu + \sigma_\omega \mu_t)\nabla \omega] + P_\omega - \rho \beta f_\beta(\omega^2 - \omega_0^2) + S_\omega \tag{29}$$

Where σ_ω is a model coefficient, P_ω is the specific dissipation production term, and S_ω is a user-defined source term. The code employs a *user-defined* equation of state using tabular data imported from NIST REFPROP. This data is in large part curve fit from the Span & Wagner equation of state (Span, 1994) which is expressed in terms of a non-dimensional Helmholtz function. These are generally split into an *ideal-gas* component and a *residual* component, accounting for real-gas effects:

$$\phi(\tau, \delta) = \phi^0(\delta, \tau) + \phi^r(\delta, \tau) \tag{30}$$

Where ϕ^0 is the ideal gas expression and ϕ^r is the residual expression, both functions of the reduced density $\delta = \rho/\rho_c$ and reciprocal of reduced temperature $\tau = T_c/T$. Here, the ideal-gas component expression is:

$$\phi^0(\tau, \delta) = \ln(\sigma) + a_1^0 + a_2^0 \tau + a_3^0 \ln(\tau) + \sum_{i=4}^{8} a_i^0 \ln[1 - exp(-\tau \theta_i^0)] \tag{31}$$

And the residual component:

$$\phi^r(\tau,\delta) = \sum_{i=1}^{7} n_i \delta^{d_i} \tau^{t_i} + \sum_{i=8}^{34} n_i \delta^{d_i} \tau^{t_i} \exp(-\delta^{c_i}) + \sum_{i=35}^{39} n_i \delta^{d_i} \tau^{t_i} \exp[-\alpha_i(\delta-\varepsilon_i)^2 - \beta_i(\tau-\gamma_i)^2] + \sum_{i=40}^{42} n_i \Delta^{b_i} \delta \exp[-C_i(\delta-1)^2 - D_i(\tau-1)^2] \quad (32)$$

Where:

$$\Delta = \left\{(1-\tau) + A_i[(\delta-1)^2]^{1/2B_i}\right\}^2 + B_i[(\delta-1)^2]^{a_i} \quad (33)$$

And a_i, θ_0^i, n_i, a_i, b_i, β_i, A_i, B_i, C_i, and D_i are model coefficients.

The density-based (coupled) solver in STAR-CCM+ solves all conservation equations simultaneously as a vector of equations. The velocity field is obtained from conservation of momentum, the pressure is obtained from this result and the continuity equation, and density is obtained from the equation of state. These equations are shown here in vector form:

$$\frac{\partial}{\partial t}\int_V \boldsymbol{W}\,\mathrm{d}V + \oint [\boldsymbol{F} - \boldsymbol{G}] \cdot \mathrm{d}\boldsymbol{a} = \int_V \boldsymbol{H}\,\mathrm{d}V \quad (34)$$

Where $\boldsymbol{W}$ is the state vector, $\boldsymbol{F}$ and $\boldsymbol{G}$ contain convective and viscous forces, and $\boldsymbol{H}$ is the total body force vector:

$$\boldsymbol{W} = \begin{bmatrix} \rho \\ \rho\boldsymbol{v} \\ \rho E \end{bmatrix} \quad (35)$$

$$\boldsymbol{F} = \begin{bmatrix} \rho\boldsymbol{v} \\ \rho\boldsymbol{v}\boldsymbol{v} + P\boldsymbol{I} \\ \rho\boldsymbol{v}H + P\boldsymbol{v} \end{bmatrix} \quad (36)$$

$$\boldsymbol{G} = \begin{bmatrix} 0 \\ \boldsymbol{T} \\ \boldsymbol{T} \cdot \boldsymbol{v} + q'' \end{bmatrix} \tag{37}$$

$$\boldsymbol{H} = \begin{bmatrix} S_u \\ f_r + f_g + f_P + f_u + f_\omega + f_L \\ S_u \end{bmatrix} \tag{38}$$

A boundary layer of stacked hexagonal prisms and core mesh of polyhedral cells were used. Wall y^+ values were all below 1, allowing an accurate characterization of the thermal boundary layer and at least 3 computational cells in the viscous sublayer. A constant mass flow inlet, pressure outlet, and non-slip, constant heat flux pipe wall boundary conditions were selected. The computational mesh is shown in Figure 3.6.

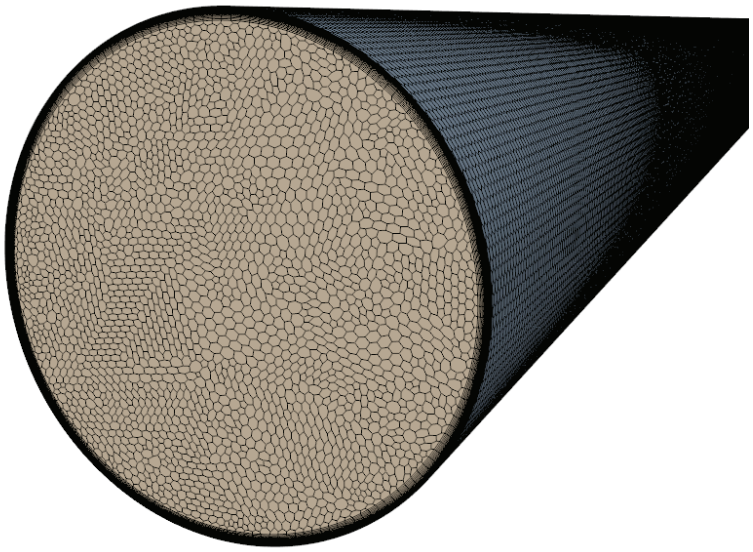

Figure 3.6 Computational mesh for horizontal pipe CFD benchmarking effort

Results are presented, calculated from CFD results using both approaches from Equations 19 and 21. Inlet wall temperatures were taken 5 cm into the test section to mitigate numerical artifacts from the interface between the adiabatic inlet section wall and the heat transfer section wall. HTC prediction, plotted as a function of average bulk

temperature and calculated using a constant wall heat flux of $-12{,}000\ \mathrm{W/m^2}$ (a cooling heat flux), is seen in Figure 3.7. Due to variable fluid properties, it is difficult to predict an average bulk temperature for a given inlet temperature in a numerical simulation, therefore, there is not a one-to-one correspondence of HTC data with the 2004 experiment. It is clear, however, the current predictions follow the trend set by experiment and values within 10%, with larger errors at the pseudocritical line peak and smaller errors away from it, as expected.

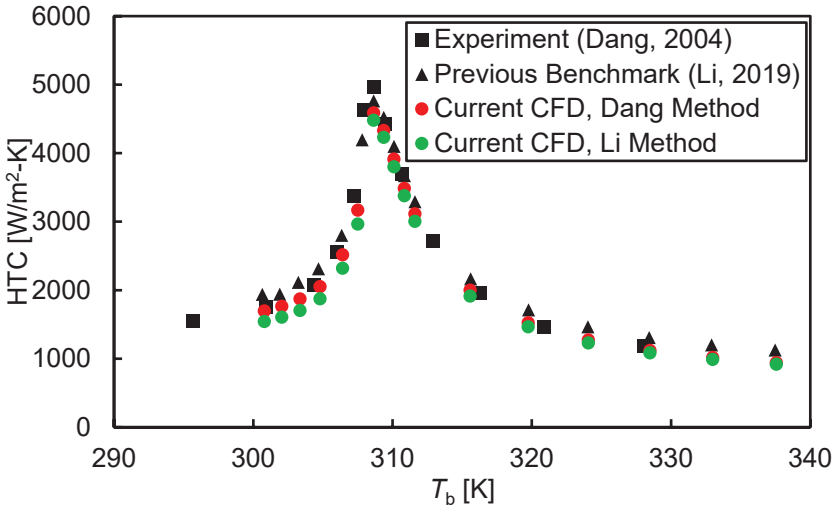

Figure 3.7 HTC prediction: current CFD results compared to experiment and previous benchmarking.

Local (streamwise) values of HTC are presented for select cases with $T_{inlet} = 306\ \mathrm{K}$, 309 K, and 312 K in Figure 3.8, Figure 3.9, and Figure 3.10. The values are calculated using the reported constant heat flux, local bulk temperature on a plane at each streamwise location calculated from Equation 22, and a circumferential average of wall temperature at the same location. The data are compared against the corresponding values from Figure 3.7.

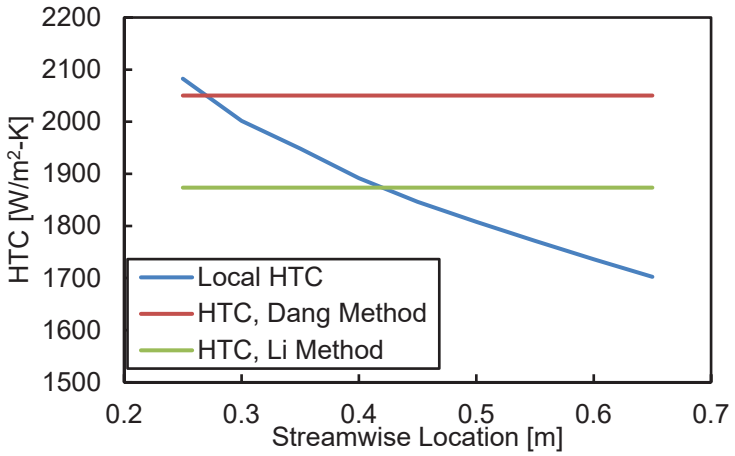

Figure 3.8 Streamwise HTC Variation, $T_{\text{inlet}} = 306\,\text{K}$

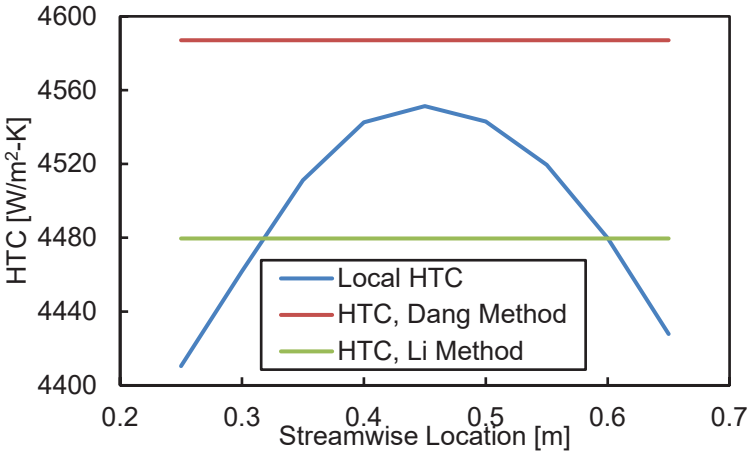

Figure 3.9 Streamwise HTC Variation, $T_{\text{inlet}} = 309\,\text{K}$

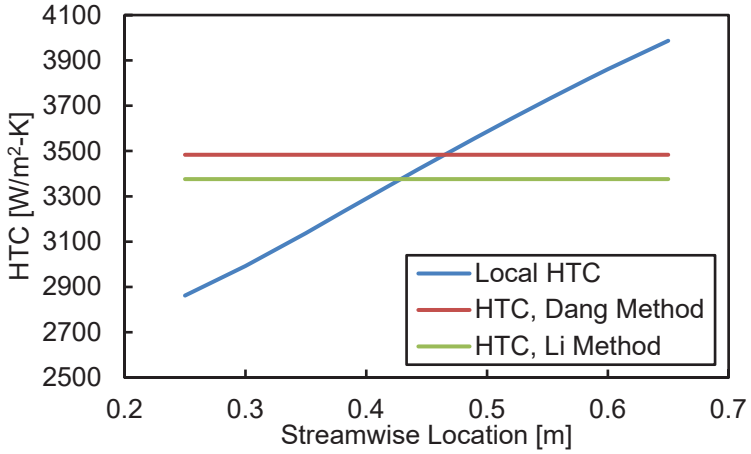

Figure 3.10 Streamwise HTC variation, $T_{\text{inlet}} = 312\,\text{K}$

The global HTC value calculated as per (Dang, 2004) matches most closely with the

experimental value, however it is demonstrated as a poor average value when compared to the corresponding local streamwise HTC. The Dang & Hihara method involves taking wall temperature at a single location for a given pipe cross section. This is common in the experimental literature for subcritical buoyant flows and can represent a functional average wall temperature value. Figure 3.11 shows a circumferential temperature distribution at 60 cm for a test case with an inlet temperature of 306 K, which indicates this is often not the case under current conditions. Fluid properties can vary significantly across this temperature range, so a single temperature value taken at mid pipe elevation can lead to problematic assumptions. Also, the resulting variation in local HTC value around a pipe circumference at a single streamwise location is striking.

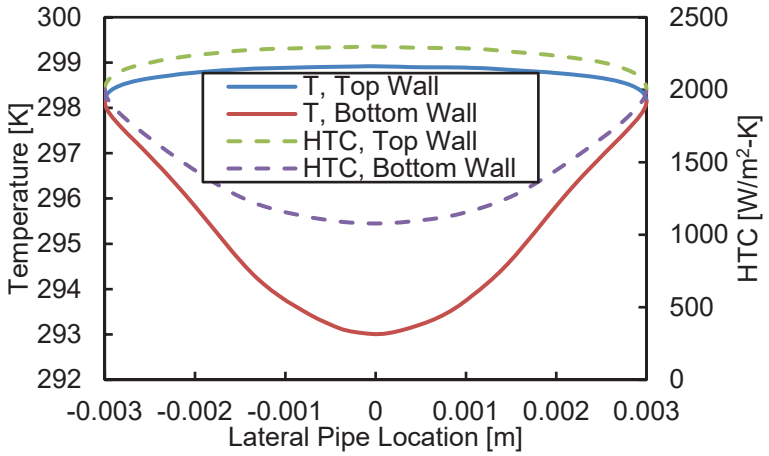

Figure 3.11 Circumferential temperature and HTC distribution, 60 cm pipe cross section, $T_{\text{inlet}} = 306\,\text{K}$.

The experiment uses a 0.2 m long adiabatic entrance length to establish fully developed flow before the fluid enters the heat transfer section. This would traditionally be considered an appropriate length, given traditional metrics for entrance lengths for turbulent flows ($\text{Re}_D > 2{,}900$) are on the order of $L/D = 10$ (Çengel, 2006). This adiabatic length would give $L/D = 33$. This is supported if flow development is

determined based on pressure gradient, which stabilizes in the adiabatic length at approximately 15 cm ($L/D = 25$), as seen in Figure 3.12, which shows $\mathrm{d}P/\mathrm{d}x$ for three inlet temperatures, with data taken as a moving average with a window of 7 points to remove noise arising from the numerical method.

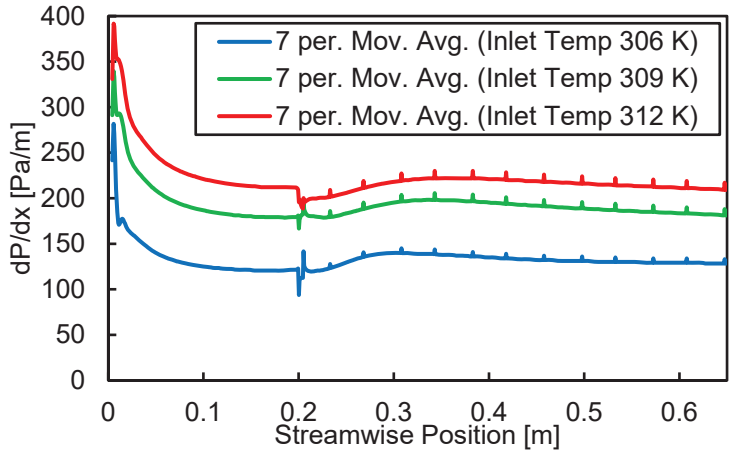

Figure 3.12 Pressure gradient, select cases

A more holistic investigation of the flow field shows the development length may in fact not be sufficient: for example, centerline velocity is seen to not reach an asymptote in the first 0.2 m in Figure 3.13.

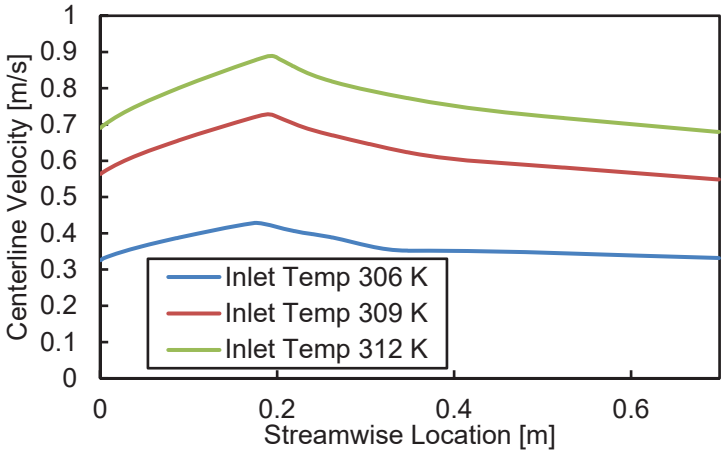

Figure 3.13 Centerline velocity, select cases

Normalized streamwise velocity profiles are shown in Figure 3.14, Figure 3.15, and

Figure 3.16 for inlet temperatures of 306 K, 309 K, and 312 K.

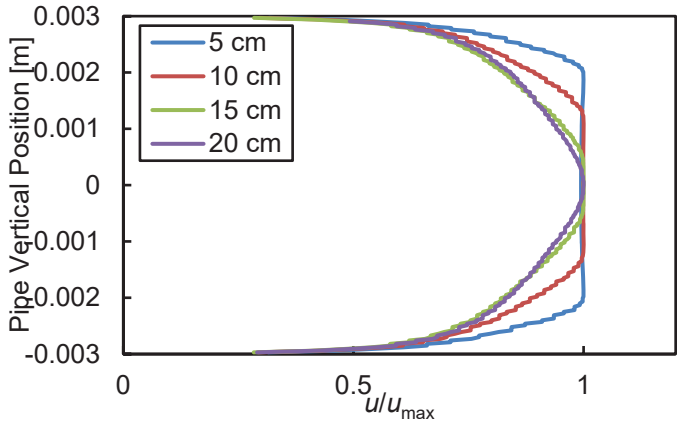

Figure 3.14 Streamwise velocity profiles: adiabatic inlet, $T_{\text{inlet}} = 306\ \text{K}$

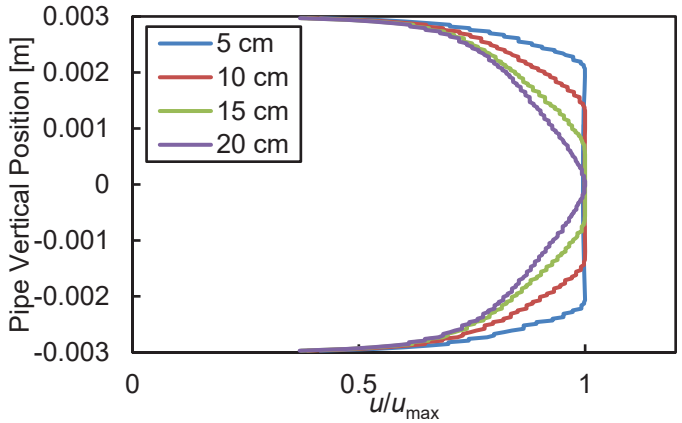

Figure 3.15 Streamwise velocity profiles: adiabatic inlet, $T_{\text{inlet}} = 309\ \text{K}$

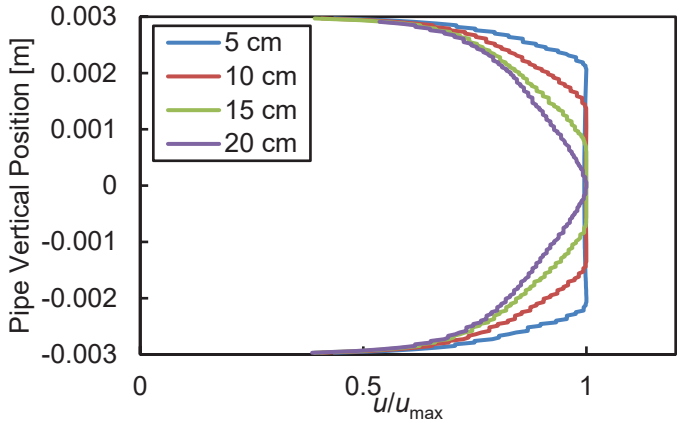

Figure 3.16 Streamwise velocity profiles: adiabatic inlet, $T_{\text{inlet}} = 312\ \text{K}$

It appears the self-similarity of the velocity profile changes with inlet temperature, with the less viscous (higher Re) fluid at higher temperature requiring a significantly longer entrance length. Figure 3.17, Figure 3.18, and Figure 3.19 show the impact of heat transfer on the hydraulic boundary layer development; again, the length at which self-similarity is observed varies across this (relatively small) range of inlet temperature.

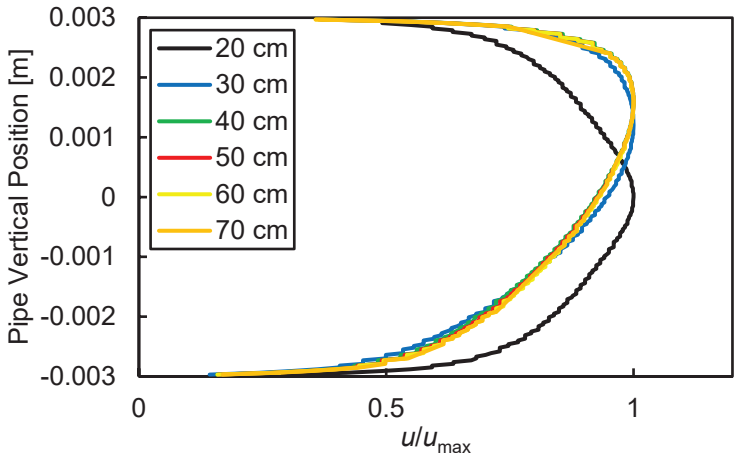

Figure 3.17 Streamwise velocity profiles: test section, $T_{\text{inlet}} = 306\,\text{K}$

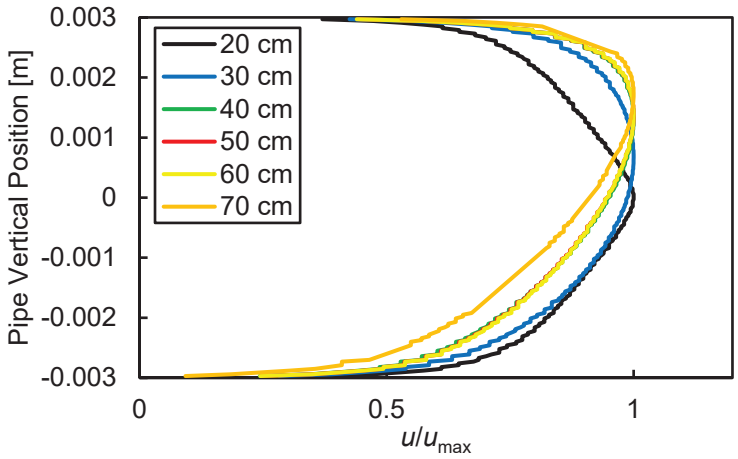

Figure 3.18 Streamwise velocity profiles: test section, $T_{\text{inlet}} = 309\,\text{K}$

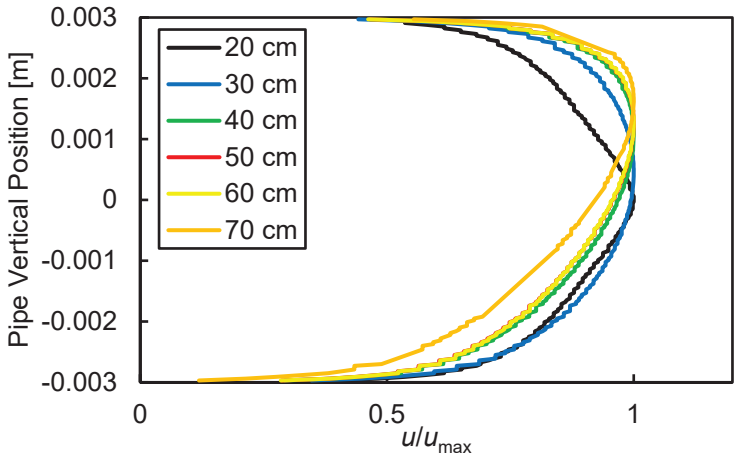

Figure 3.19 Streamwise velocity profiles: test section, $T_{\text{inlet}} = 312\,\text{K}$

In these flows near the pseudocritical line, the heat transfer section imposes not only a temperature gradient, but a significant gradient in viscosity, in both the radial and streamwise directions. Table 3.1 highlights this change, with the resulting change in Re, should this value be taken based on inlet or outlet conditions.

Table 3.1

Viscosity variation, select cases

	Inlet	Outlet	% Change
$T_{\text{inlet}} = 306\,\text{K}$			
μ [Pa-s]	4.596×10^{-5}	5.591×10^{-5}	↑ 21.6
Re_D	26,107	21,461	↓ 17.8
$T_{\text{inlet}} = 309\,\text{K}$			
μ [Pa-s]	2.599×10^{-5}	3.025×10^{-5}	↑ 16.4
Re_D	46,163	39,670	↓ 14.1
$T_{\text{inlet}} = 312\,\text{K}$			
μ [Pa-s]	2.282×10^{-5}	2.542×10^{-5}	↑ 11.4
Re_D	52,578	47,198	↓ 10.2

One feature shared among all the above velocity profiles is that none demonstrate the expected shape of fully developed turbulent flow, which is a flatter distribution promoted by turbulent mixing. The expected streamwise velocity distribution of a fully developed

turbulent duct flow can be described using fluid properties and experimental data collected over many years by several researchers, dating back to such figures as Jean Louis Poiseuille and Osborne Reynolds (Pritchard, 2011). The shear stress on a fluid can be expressed as the sum of laminar and turbulent quantities:

$$\tau = \tau_{\text{lam}} + \tau_{\text{turb}} = \mu \frac{\mathrm{d}\overline{u}}{\mathrm{d}y} - \rho\overline{u'v'} \tag{39}$$

Where $\overline{u}$ is the mean streamwise velocity and u' and v' are fluctuating velocity components. The overbar represents a time average, giving the Reynolds stress $-\rho\overline{u'v'}$. Dividing this by density gives:

$$\frac{\tau}{\rho} = \nu \frac{\mathrm{d}\overline{u}}{\mathrm{d}y} - \overline{u'v'} \tag{40}$$

Where ν is the kinematic viscosity. The quantity τ/ρ is significant and often the square root of the quantity is taken, $(\tau/\rho)^{1/2}$, which has units of velocity. It is referred to as the *friction velocity*, denoted u^*, and is constant (for subcritical flows). The non-dimensional parameter $\overline{u}/u^*$, denoted u^+, is often plotted against a non-dimensional wall distance, taken as yu^*/ν, most often denoted y^+. Experimental data (Tennekes, 1972) shows fully developed velocity distributions can be expressed as:

$$\begin{cases} u^+ = \dfrac{\overline{u}}{u^*} = \dfrac{yu^*}{\nu} = y^+ \ , \ 0 \le y^+ \le \text{5-7} \\ u^+ = 2.5\ \ln(y^+) + 5.0,\ y^+ > 30 \end{cases} \tag{41}$$

Where the region $0 \le y^+ \le$ 5-7 is the viscous sublayer. The region 5-7 $< y^+ < 30$ is a transitional region called the buffer layer and is not covered by this correlation. These equations apply nominally to flows where ν, and therefore μ and ρ, are constant, which is not the case in these transcritical pipe flows. The velocity profile can also be described by the so-called empirical power law equation:

$$\frac{\overline{u}}{U} = \left(\frac{y}{R}\right)^{1/n} = \left(1 - \frac{r}{R}\right)^{1/n} \tag{42}$$

Where U is the centerline velocity, R is the pipe radius, and n is a function of Re (Hinze, 1975):

$$n = -1.7 + 1.8 \log_{10} \mathrm{Re} \tag{43}$$

Which is valid for $\mathrm{Re} > 2 \times 10^4$, encompassed by the current regime. This eliminates fluid properties from the calculation of velocity, but a Reynolds number remains, the value of which depending on constantly changing reference quantities in these flows. The thermal boundary layer development is driven by the development of the hydraulic boundary layer in a way that can be described by invoking the Prandtl number:

$$\frac{\delta_t}{\delta} = \mathrm{Pr}^{-1/3},\ 0.6 \leq \mathrm{Pr} \leq 50 \tag{44}$$

Where δ is the hydraulic boundary layer thickness, and δ_t is the thermal boundary layer thickness. In these near-critical heat transfer flows, a continuously variable viscosity may call into question the nature of a fully developed boundary layer. A significant variation in Pr exacerbates this issue and is further discussed in Section 3.4. Additionally, the significant variation in density can lead to continuously varying flow velocities, also with gradients in the streamwise and radial directions.

3.3. Cylindrical Pin-Fin Array

Internal blade cooling using bleed sCO_2 from the compressor outlet is simulated at 30 MPa, which is bled into the hot gas path, in a direct-fired Brayton cycle. An alternative, closed-loop cooling configuration at a 7.4 MPa (closer to the critical point) is also investigated for its ability to take advantage of fluid property variation. This

configuration would add complexity and capital cost to the cycle but provide potentially increased cooling effectiveness. Both configurations are shown in Figure 3.20. Computational work that has been validated by experiment in air at laboratory conditions is used as a benchmark for current work (Prasad, 2018).

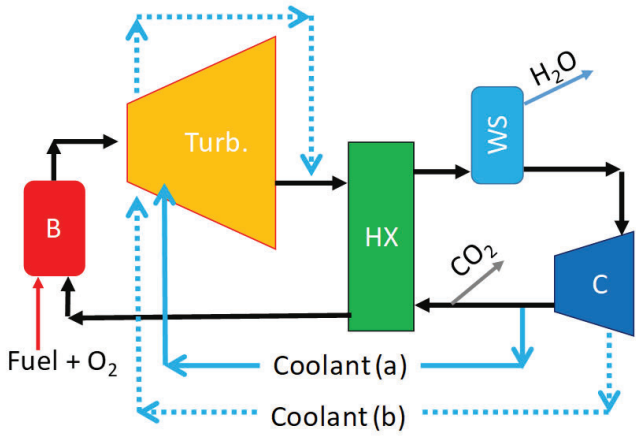

Figure 3.20 Direct-fired Brayton cycle cooling configurations

For the conventional compressor bleed case, the cooling channel inlet temperature assumes compressor inlet temperature of 300 K, and an isentropic compressor with inlet pressure 10 MPa and pressure ratio 3 (compressor outlet 330 K and 30 MPa). The endwall and pin temperature assumes an ideal combustor giving TIT of 1200 K. A one-dimensional conduction model is used through a 0.5 mm thick Inconel turbine blade wall, estimated to be representative of sCO_2 turbine blade construction. The hot gas path heat transfer coefficient was obtained from a chord length-averaged Nu via the Chilton-Colburn analogy (Berman, 2011).

$$\overline{\mathrm{Nu}}_L = \left(0.037\,\mathrm{Re}_L^{4/5} - A\right)\mathrm{Pr}^{1/3} \tag{45}$$

Which is valid over the range $0.6 \leq \mathrm{Pr} \leq 60$ and $\mathrm{Re}_{x,c} \leq \mathrm{Re}_L \leq 10^8$. A is given as:

$$A = 0.037\,\mathrm{Re}_{x,c}^{4/5} - 0.664\,\mathrm{Re}_{x,c}^{1/2} \tag{46}$$

Where $\mathrm{Re}_{x,c}$ is the transitional Reynolds number, taken here as 500,000.

This fluid stream, entering the turbine at or near 30 MPa, is well within the supercritical regime and therefore established heat transfer correlations are more likely to apply. As a starting point, the coolant-side heat transfer coefficient was obtained from the Dittus-Boelter correlation, shown in Equation 47, along with an enhancement coefficient to account for the effect of pins or other turbulators. Blade chord length is taken as 51 mm (Barber-Nichols, Inc.) and the cooling channel is sized based on a first-stage turbine blade from a CFM56 (aero engine) gas turbine, shown in Figure 3.22.

$$\mathrm{Nu} = 0.023\,\mathrm{Re}^{4/5}\mathrm{Pr}^{n} \tag{47}$$

Where n is taken as 0.4 for a fluid being heated (current case), and 0.3 for a fluid being cooled. The one-dimensional heat transfer model is shown in Figure 3.21.

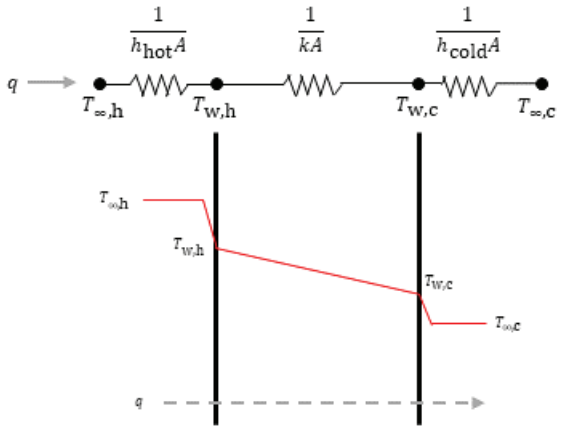

Figure 3.21 Turbine blade one-dimensional heat transfer model

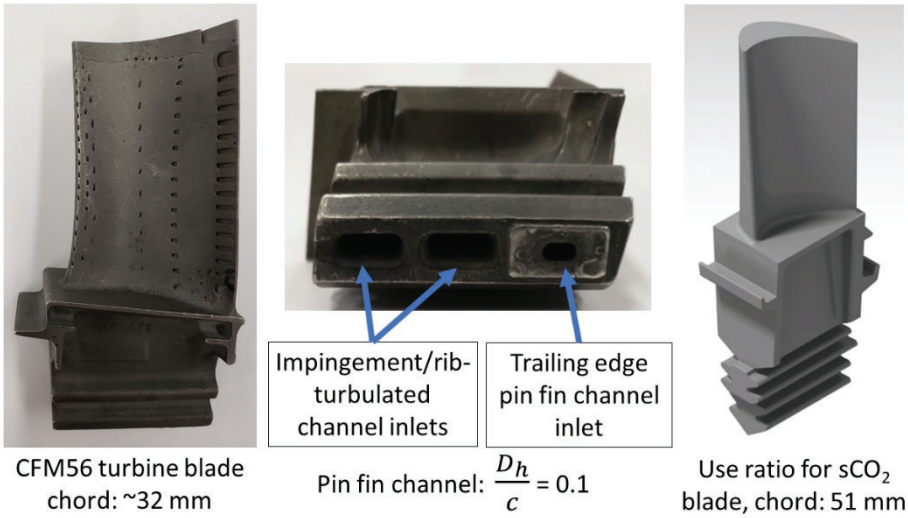

Figure 3.22 Turbine blade and typical cooling geometry example

Thermodynamic and transport properties of carbon dioxide were extracted from REFPROP, a software package released by NIST. These files contain pressure-temperature tabulated fluid properties and use the equation of state developed by Span and Wagner (1996). Cases run at 30 MPa used data from 300 K to 400 K and from 20 MPa to 60 MPa, at 1000 temperature points and 1000 pressure points. Cases simulating a closed-loop cooling configuration used data from 250 K to 400 K and from 7 MPa to 9 MPa, also at 1000 temperature points and 1000 pressure points. Speed of sound, specific heats, enthalpy, thermal conductivity, dynamic viscosity, density, and entropy were included in the model. The 3-dimensional computational domain used a mass flow inlet and pressure outlet, along with periodic boundary conditions on left and right sides. No-slip, constant temperature walls were selected for the bottom endwall and pin surfaces, and the top wall was adiabatic. These boundary conditions correspond to the existing validated simulations in air (Prasad, 2018). The computational domain with boundary conditions is seen in Figure 3.23.

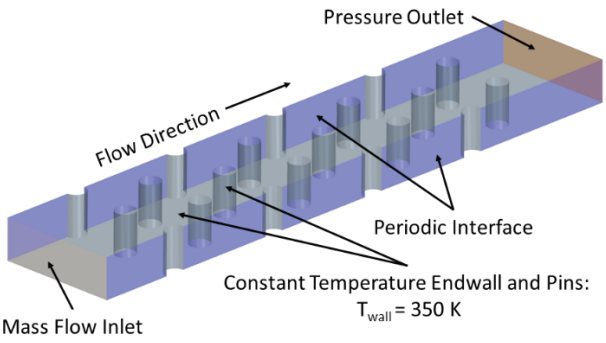

Figure 3.23 Staggered cylindrical pin fin array computational domain

To permit increasing TIT, modern gas turbine engines employ advanced internal cooling designs and geometries. These include jet impingement channels on leading edges, rib and baffle-turbulated sections at mid-chord, and often, pin-fin channels near the trailing edge. A planform view of the staggered cylindrical pin-fin array is shown in Figure 3.24.

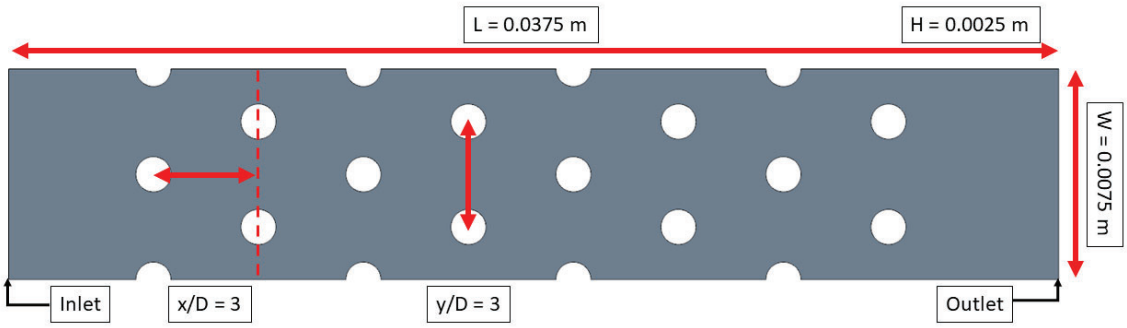

Figure 3.24 Staggered cylindrical pin fin array planform, $D_{\text{pin}} = 1.25$ mm

Cases with air as the working fluid were run with an ideal gas EoS at an operating pressure of 1 atmosphere (~0.1 MPa). Cases with sCO_2 were run at 30 MPa, representing bleed CO_2 at compressor outlet conditions. Closed-loop cooling cases were run (near the critical pressure) at 7.4 MPa. Table 2, below, summarizes conditions for each test case. Spatial discretization is second order. Turbulence closure was achieved with k-ω SST (Menter, 1994) using default model coefficients. SST has been shown to perform well

relative to other models for pin-fin channel flows (Fernandes, 2017). The mesh consists of roughly 11 million cells, with polyhedral core cells and between 30 and 50 prismatic boundary layers on wall and pin surfaces. Mesh independence was previously conducted in air for the same geometry (Prasad, 2018) and several cases in present work were simulated at 19 million cells to ensure the change in working fluid had no impact on mesh independence. No appreciable change in results were observed at this increased mesh density. All wall y^+ values are below 1. The mesh configuration at the intersection of the bottom endwall and a pin fin is shown in Figure 3.25.

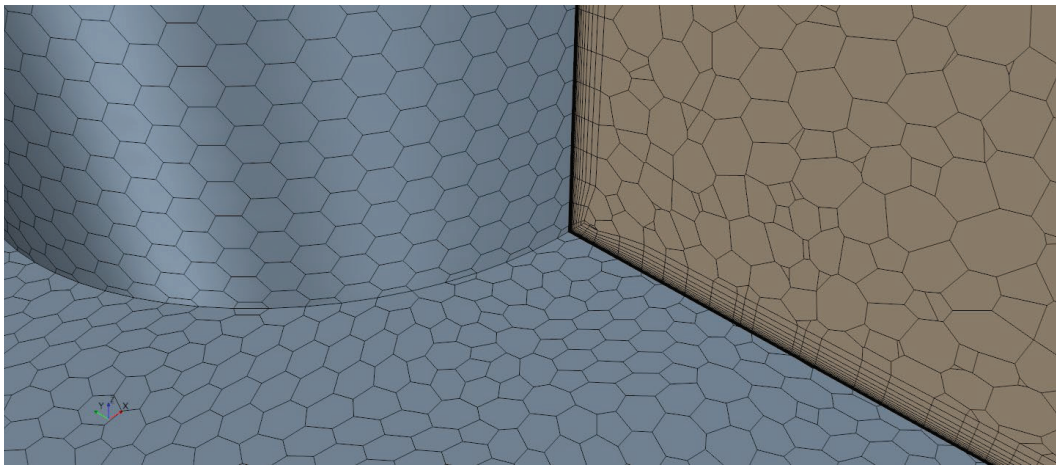

Figure 3.25 Boundary layer and core mesh structure

3.3.1. Pin-Fin Array Data Reduction

Results from air and sCO_2 cases were compared against Nusselt number correlations developed for staggered pin fin arrays in air. Reynolds number is calculated with inlet conditions and pin diameter. Nusselt numbers are taken as an average of values on pin surface and endwall combined. The characteristic length is pin-fin diameter and thermal conductivity is taken at the inlet. Characteristic lengths from literature variously reference hydraulic diameter and pin-fin diameter. In the interest of consistency for current work,

calculated values and values predicted from correlations all use pin-fin diameter as reference length.

$$\mathrm{Re}_D = \frac{\rho_{\mathrm{in}} u_{\mathrm{in}} D_{\mathrm{in}}}{\mu_{\mathrm{in}}} \tag{48}$$

$$\mathrm{Nu}_{\mathrm{sCO_2}} = \frac{h D_{\mathrm{pin}}}{k_{\mathrm{in}}} \tag{49}$$

Heat transfer correlations (for air) used for comparison are as follows:

From (Metzger, 1982):

$$\mathrm{Nu}_D = 0.079\ \mathrm{Re}_D^{0.717} \tag{50}$$

From (Van Fossen, 1982):

$$\mathrm{Nu}_D = 1.12 \left(\frac{D}{D'}\right)^{0.153} \mathrm{Re}_{D'}^{0.685} \tag{51}$$

Where D' is a hydraulic diameter defined by:

$$D' = 4\frac{V}{S} \tag{52}$$

Where V is the fluid volume and S is the wetted surface area.

From (Short, 2002):

$$\mathrm{Nu}_{D_{\mathrm{h}}} = 0.419 \left(\frac{H_{\mathrm{pin}}}{D_{\mathrm{h}}}\right)^{-0.3} \left(\frac{S_{\mathrm{L}}}{D_{\mathrm{h}}}\right)^{0.077} \left(\frac{S_{\mathrm{T}}}{D_{\mathrm{h}}}\right)^{0.2} \mathrm{Re}_{D_{\mathrm{h}}}^{0.45} \mathrm{Pr}_{\mathrm{b}}^{1/3} \tag{53}$$

Where S_{L} is the pin pitch in the streamwise direction and S_{T} is pin pitch in the transverse direction. This correlation was developed for macro pin fin arrays. Friction factor was obtained to assess relative performance of the cooling geometry under various flow conditions and is calculated using the method employed in (Liao, 2002) which accounts for pressure drop across mini/micro channels due to viscous friction in the following manner:

$$f = \frac{\Delta P_f}{\frac{1}{2}\rho_{\mathrm{b}} u_{\mathrm{b}}^2} \frac{L}{D_{\mathrm{h}}} \tag{54}$$

Where ρ_{b} and u_{b} are density taken at bulk temperature and streamwise velocity of the bulk flow, respectively. L is the length of the array and D_{h} is the hydraulic diameter of the array. Bulk quantities are obtained by averaging over the entire computational domain volume. As left and right boundaries are periodic, the domain is effectively infinite in the spanwise direction so hydraulic diameter is taken as twice the channel height. Further:

$$\Delta P_f = \Delta P - \left(\frac{\rho_{\mathrm{out}} u_{\mathrm{out}}^2}{2} - \frac{\rho_{\mathrm{in}} u_{\mathrm{in}}^2}{2} \right) \tag{55}$$

Where ΔP is stagnation pressure drop across the domain, with density and streamwise velocity taken at outlet and inlet.

3.4. Reduced-Order Model

An investigation was performed into an optimization of the unique heat transfer enhancement phenomena intrinsic to supercritical fluids in a cooling flow of supercritical carbon dioxide (sCO_2) in forced convection. A one-dimensional heat transfer code was written both to assess the applicability of a reduced-order model in predicting heat transfer in horizontal pipe cooling flows and to consider a method of harnessing the unique and highly variable fluid properties of CO_2 in the pseudocritical region. The pipe geometry and experimental conditions from the experiment by Dang and Hihara (Dang, 2004) was selected, as a simple flow geometry was desired for this exploratory study, and CFD benchmarking had already been performed, matching well, even across the pseudocritical line. The CFD results help to inform and assess the one-dimensional code. Specifically, a series of test cases with constant mass flux, heat flux, and pipe diameter with a range of inlet temperatures was simulated and heat transfer coefficient prediction

was compared with experiment.

The HTC prediction is shown compared against experimental values above in Figure 3.7. CFD results match well with experiment, including in the pseudocritical region, where a peak in heat transfer occurs for this cooling flow. The pseudocritical temperature is obtained via curve fit from REFPROP data (Liao, 2002):

$$T_{\mathrm{pc}} = -122.6 + 6.124\,P - 0.1657\,P^2 + 0.01773\,P^{2.5} - 0.0005608\,P^3 \tag{56}$$

Where T_{pc} is given in ℃ and P is the static pressure in bar. The favorable benchmarking result gives confidence in the use of local fluid properties and flow quantities from CFD to inform a reduced order model, based on the empirical correlation proposed by Dang and Hihara, who propose the following modified Gnielinski correlation for Nusselt number prediction:

$$\mathrm{Nu} = \frac{(f_{\mathrm{f}}/8)(\mathrm{Re_b} - 1000)\mathrm{Pr}}{1.07 + 12.7\sqrt{f_{\mathrm{f}}/8}(\mathrm{Pr}^{2/3} - 1)} \tag{57}$$

Where subscripts b and f refer to quantities evaluated at bulk and film temperatures, respectively. The film temperature is taken as:

$$T_{\mathrm{f}} = (T_{\mathrm{b}} + T_{\mathrm{w}})/2 \tag{58}$$

Where subscript w refers to the temperature at the inner pipe wall. Prandtl number in Equation 57 is obtained from a switch case, which depends on quantities taken at bulk and film conditions:

$$\begin{cases} c_{p_{\mathrm{b}}}\mu_{\mathrm{b}}/k_{\mathrm{b}}, & \text{for } c_{p_{\mathrm{b}}} \geq \overline{c}_p \\ \overline{c}_p\mu_{\mathrm{b}}/k_{\mathrm{b}}, & \text{for } c_{p_{\mathrm{b}}} < \overline{c}_p \text{ and } \mu_{\mathrm{b}}/k_{\mathrm{b}} \geq \mu_{\mathrm{f}}/k_{\mathrm{f}} \\ \overline{c}_p\mu_{\mathrm{f}}/k_{\mathrm{f}}, & \text{for } c_{p_{\mathrm{b}}} < \overline{c}_p \text{ and } \mu_{\mathrm{b}}/k_{\mathrm{b}} < \mu_{\mathrm{f}}/k_{\mathrm{f}} \end{cases} \tag{59}$$

Where $\overline{c}_p$ is an "integrated" specific heat capacity defined as:

$$\overline{c}_p = (h_{\mathrm{b}} - h_{\mathrm{w}})/(T_{\mathrm{b}} - T_{\mathrm{w}}) \tag{60}$$

Where h is fluid enthalpy. The correlation is also a function of the friction factor, which is taken at film temperature and calculated according to (Filonenko, 1954):

$$f_{\mathrm{f}} = [\log_{10}(\mathrm{Re}_{\mathrm{f}}) - 1.64]^{-2} \tag{61}$$

The Reynolds numbers are calculated as:

$$\mathrm{Re}_{\mathrm{b}} = Gd/\mu_{\mathrm{b}} \tag{62}$$

And:

$$\mathrm{Re}_{\mathrm{f}} = Gd/\mu_{\mathrm{f}} \tag{63}$$

Finally, HTC is calculated using thermal conductivity taken at film temperature:

$$\mathrm{HTC} = \mathrm{Nu}\, k_{\mathrm{f}}/D_{\mathrm{h}} \tag{64}$$

Where D_{h} is the hydraulic diameter of the pipe.

An algorithm to simulate a buoyancy-free supercritical cooling flow with constant heat flux boundary condition and real fluid properties was implemented in MATLAB. The algorithm is summarized in Figure 3.26. Due to rapidly changing fluid properties in both the axial and radial directions, an iterative approach is necessary for this simplified cooling model. Boundary conditions are first input to the model, in this case: a pipe hydraulic diameter, mass flux, constant heat flux, and inlet pressure and temperature. Using pressure and bulk temperature in a cell, the code queries the NIST REFPROP software for fluid properties (density, dynamic viscosity, thermal conductivity, and constant pressure specific heat capacity are required). A reasonable film temperature guess is made and fluid properties at this location are obtained. Using bulk and film temperatures and properties, the modified Gnielinski correlation is invoked, and a heat balance is performed. The resulting heat flux is compared against the target constant value and the algorithm repeats, having incremented the wall temperature appropriately,

until a suitable convergence is obtained. Another heat balance is performed using the constant heat flux to obtain bulk conditions in the next cell. This process continues for all cells in the one-dimensional domain.

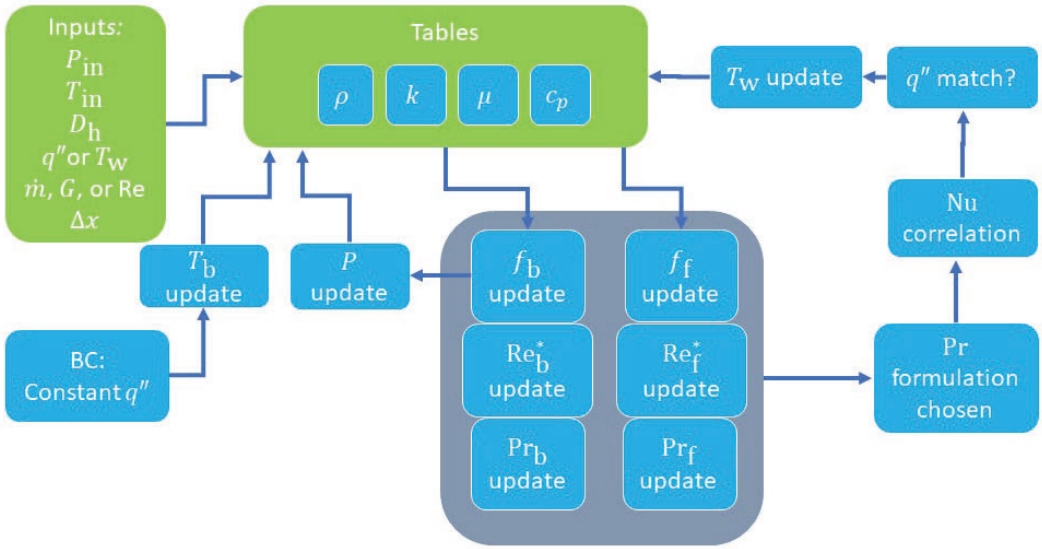

Figure 3.26 One-dimensional model algorithm

Challenges arise with this simplified approach due to the need for reference values for the important non-dimensional quantities Re and Nu. The Reynolds numbers in Figure 3.26 receive asterisks and this indicates they are updated to reflect local changes in viscosity, affecting the Darcy friction factor. The friction factor in turn affects the pressure drop, which is not constant in the axial direction in near-critical flows. Further, Figure 3.27 illustrates the significant variation in Prandtl number in the pipe cross section for a simulation with inlet temperature 309 K; Prandtl here significantly increases toward the wall, with a sharp decline within the thermal boundary layer. Clearly, not only is a two-fold variation possible, but the change is not necessarily monotonic, either in the radial or axial directions.

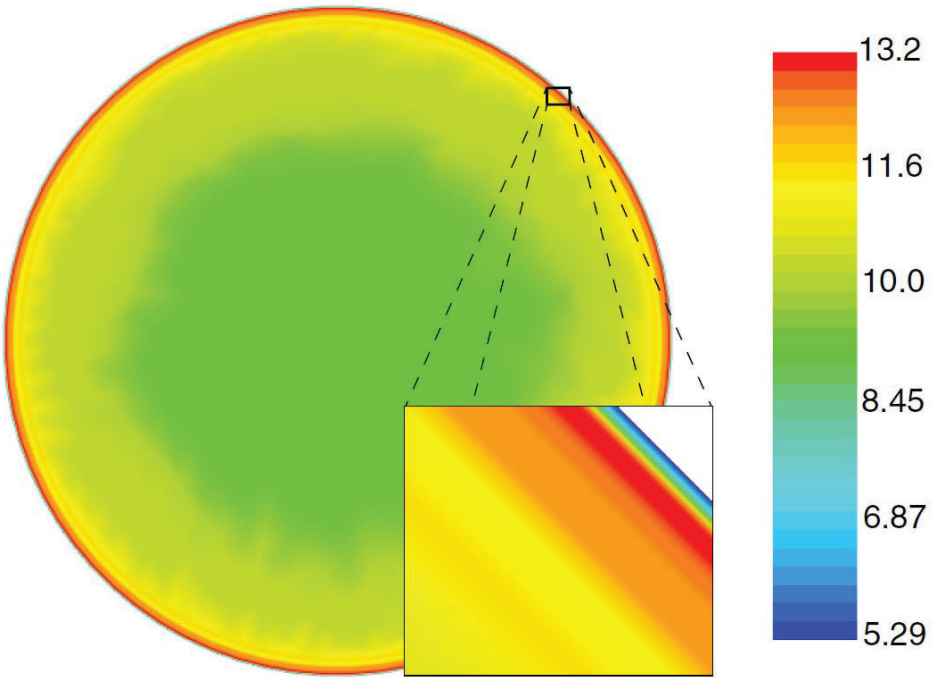

Figure 3.27 Prandtl number variation from CFD results, $T_{\text{inlet}} = 309$ K, cooled section at 60 cm.

The trend seen at this cross section is not consistent, however, and Pr trends are sensitive to small changes in boundary or inlet conditions. Figure 3.28 shows the evolution of Prandtl number distributions along the test section length of a single test case with $T_{\text{inlet}} = 309$ K, and Figure 3.29 shows the same pipe cross sections with $T_{\text{inlet}} = 306$ K.

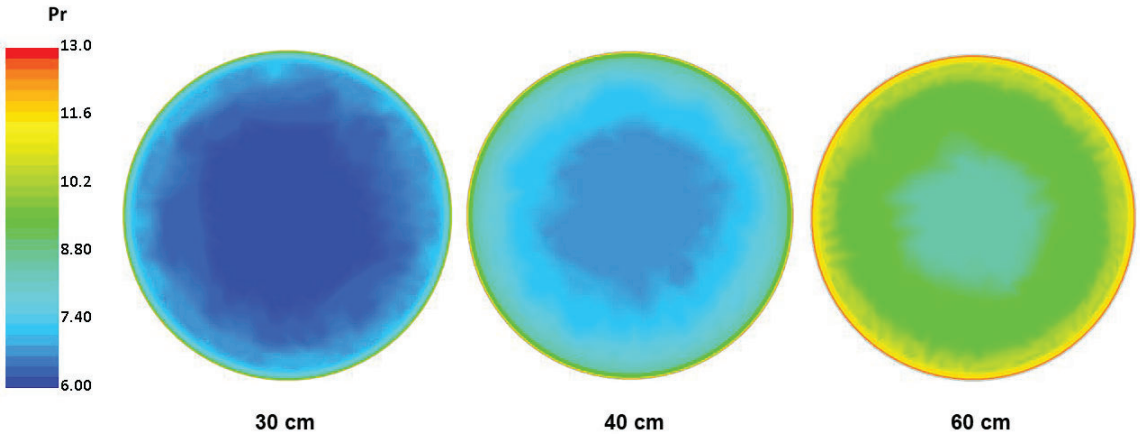

Figure 3.28 Prandtl number variation at various cross sections, $T_{\text{inlet}} = 309$ K

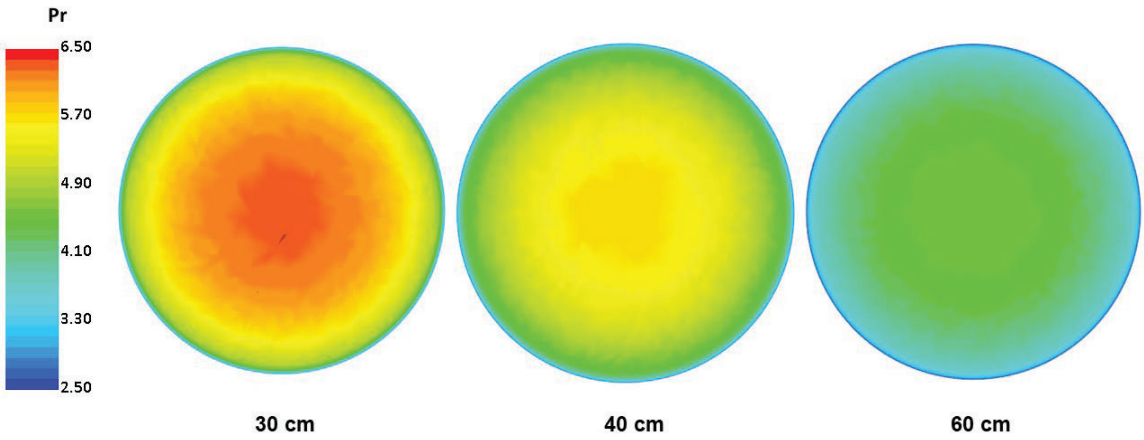

Figure 3.29 Prandtl number variation at various cross sections, $T_{\text{inlet}} = 306$ K

The Prandtl number is plotted with respect to streamwise location in the heat transfer section for these cases in Figure 3.30.

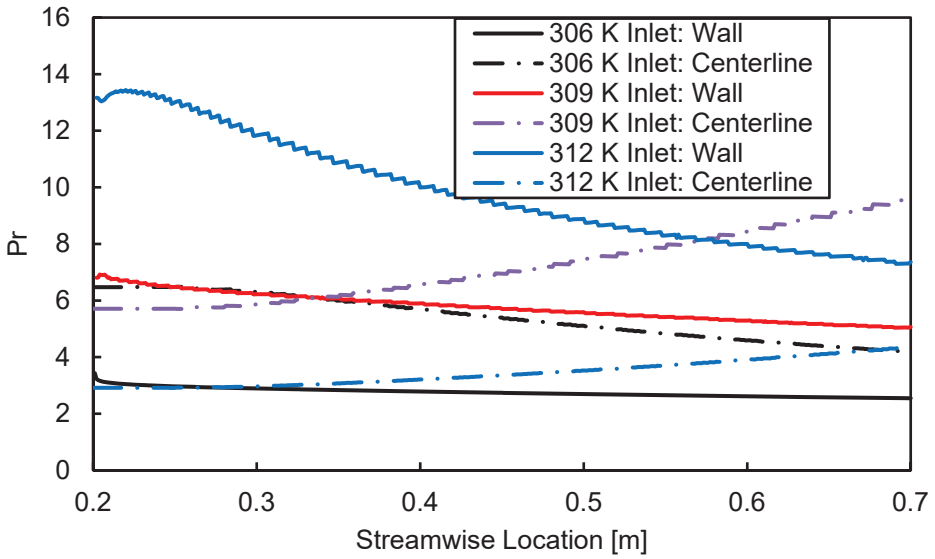

Figure 3.30 Wall and centerline Prandtl number, select cases

Variation in Pr in the streamwise direction is as large as 67% for these near-critical cases. A similar characterization is supported by data taken radially, as seen in Figure 3.31, Figure 3.32, and Figure 3.33.

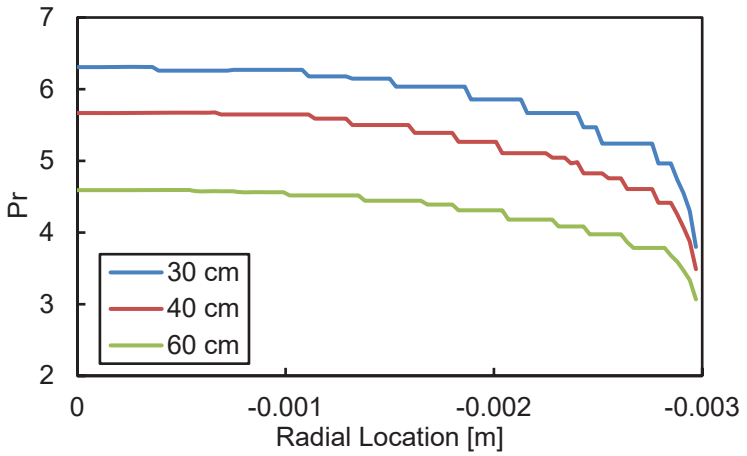

Figure 3.31 Radial Prandtl number distributions, $T_{\text{inlet}} = 306\,\text{K}$

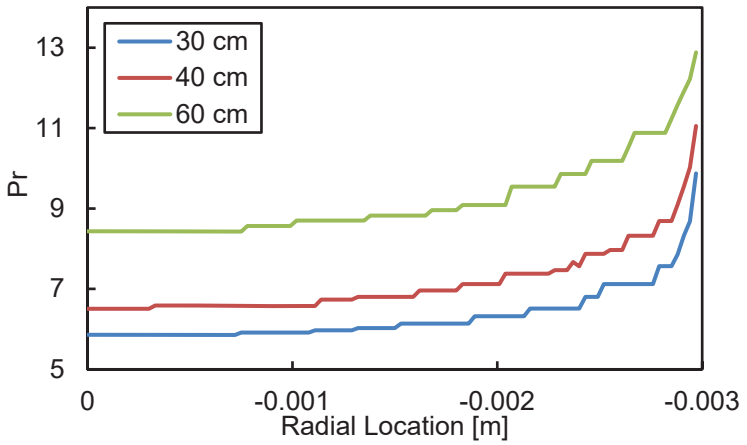

Figure 3.32 Radial Prandtl number distributions, $T_{\text{inlet}} = 309\,\text{K}$

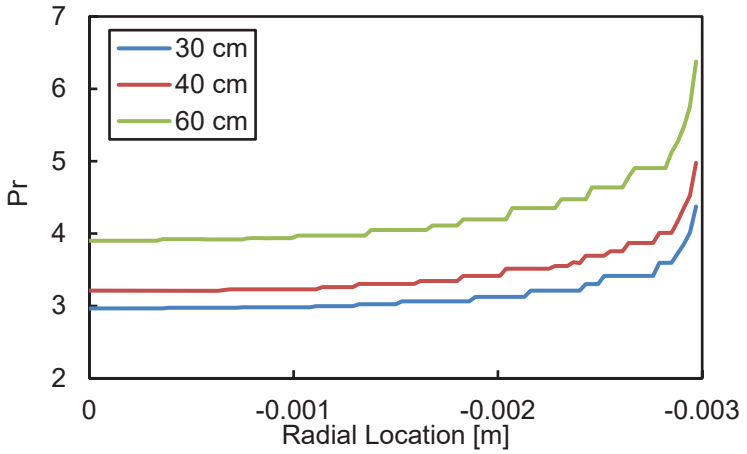

Figure 3.33 Radial Prandtl number distributions, $T_{\text{inlet}} = 312\,\text{K}$

This complicates application of the heat transfer correlation, in which Nu is a function of Pr. This is addressed in the experiment (Dang, 2004) using Equation 59, assigning a

Pr value depending on which fluid properties, taken either at bulk or film temperatures, produce a larger Pr. Use of the "integrated" specific heat value, which relies on fluid enthalpy data (for a non-calorically perfect gas, $h \neq c_p T$), can be challenging to implement in this regime. The large specific heat values near the pseudocritical line result in small radial temperature gradients for a given heat flux and therefore small denominators in Equation 60. To overcome this, a parallel approach using CFD results to inform the correlation in the one-dimensional model is used.

Another algorithm was used to determine with greater precision a local *effective* Prandtl number, $\mathrm{Pr}_{\mathrm{eff}}$, at each cross section. The heat transfer coefficient was calculated using the constant heat flux and bulk and wall temperatures from CFD results. The heat transfer coefficient and temperatures were then used to iteratively obtain a Prandtl number corresponding to these results and the correlation from (Dang, 2004). This would enable a numerically derived $\mathrm{Pr}_{\mathrm{eff}}$ which could be expressed as a function of bulk and wall *reduced* temperatures $T_{\mathrm{b,r}}$ and $T_{\mathrm{w,r}}$, as defined in Equation 65.

$$T_{\mathrm{b,r}} = \frac{T_{\mathrm{b}}}{T_{\mathrm{pc}}}$$
$$T_{\mathrm{w,r}} = \frac{T_{\mathrm{w}}}{T_{\mathrm{pc}}} \tag{65}$$

This would allow a seamless implementation of the reduced order method, utilizing a simplified semi-empirical correlation across the pseudocritical line, where experiment shows a peak in HTC. Further challenges arise from this approach from a handful of causes. First, Equation 66 makes the simple mathematical observation that because the Gnielinski correlation can be roughly approximated to a function of Pr to a weak power, backing out a Pr value from a Nu calculated from a measured HTC can lead to large errors if the correlation is not exact. The second cause follows: Dang and Hihara report

the accuracy of their correlation as 20%, a typical value for semi-empirical correlations in the experimental literature. Third, wall temperatures were not reported, so heat transfer prediction ability of CFD and the reduced-order model is assessed on the basis of HTC values only.

$$\mathrm{Nu} \sim f\left(\mathrm{Pr}^{1/3}\right) \therefore \mathrm{Pr} \sim f(\mathrm{Nu}^3) \tag{66}$$

These factors give rise to calculated $\mathrm{Pr}_{\mathrm{eff}}$ values that consistently lie outside the bounds of the extreme values (should the extremes lie at the centerline, in the boundary layer, or at the wall), challenging implementation of the developed correlation.

3.5. Uncertainty in the Critical Region

To assess the ability of the heat transfer community to both measure and predict near-critical heat transfer behavior through available sCO_2 correlations found in the literature, an uncertainty analysis is desired to track the propagation of error in these flows, with a focus on the material property uncertainty due to instrumentation error. Uncertainty analysis is seen in the literature for SC fluids (Locke, 2005) but not near the critical point or along the pseudocritical line. The sharp gradients in fluid properties seen in this region imply heat transfer predictions are highly sensitive to the accuracy of temperature and pressure measurements. An experimental test case from (Dang, 2004) is used as a baseline ($q'' = -12\ \mathrm{kW/m^2}$, $G = 200\ \mathrm{kg/m^2\text{-}s}$, $D = 6\ \mathrm{mm}$, $P = 8\ \mathrm{MPa}$, and $T_{\mathrm{in}} = 309\ \mathrm{K}$). A root-sum-square (RSS) method (Kline, 1953; Moffat, 1988) was used to calculate uncertainty in the quantities Re and Pr, important for most heat transfer correlations, arising from temperature and pressure instrumentation error. Only this category of measurement uncertainty is treated here. The uncertainty in a calculated value will be the root of the sum of squared values of partial derivatives taken with respect to

all function parameters, multiplied by their own uncertainties. Here, a nested RSS procedure is required to account for fluid properties which themselves are strong functions of temperature and weak functions of pressure in the near-critical region. The RSS method is shown for an arbitrary calculated quantity R obtained from independent variables X_i in Equation 67.

$$\delta R = \left[\sum_{i=1}^{N} \left(\frac{\partial R}{\partial X_i}\delta X_i\right)^2\right]^{1/2} \tag{67}$$

Measurement uncertainties reported in (Dang, 2004) are used here. Type-T thermocouples were calibrated to a constant accuracy of ± 0.1 ℃, and pressure transducer uncertainty is reported as ± 1000 Pa. A fine table of fluid property data (ρ, μ, c_p, and k) was created using NIST REFPROP data at 201 pressures between 7.5 MPa and 8.5 MPa and at 2001 temperatures between 280 K and 320 K, encompassing the operating pressure and range of inlet temperatures studied in the experiment. This code uses the Span and Wagner real-gas equation-of-state (Span, 1996). First-order numerical differentiation of these values was performed to obtain partial derivatives in temperature and pressure for the data. Fluid property uncertainty was then obtained with RSS. An example using density is seen in Equation 68.

$$\rho = \rho(T,P) \rightarrow \delta\rho = \left[\left(\frac{\partial \rho}{\partial T}\delta T\right)^2 + \left(\frac{\partial \rho}{\partial P}\delta P\right)^2\right]^{1/2} \tag{68}$$

Here, δT and δP are the reported thermocouple and pressure transducer uncertainties, respectively. The RSS procedure was repeated with the partial derivatives of the calculated quantities with respect to the fluid properties determined analytically. Here, the Reynolds number is defined as:

$$\mathrm{Re} = \frac{GD}{\mu} \tag{69}$$

The partial derivative of Re with respect to the dynamic viscosity, μ, is:

$$\frac{\partial \mathrm{Re}}{\partial \mu} = -\frac{GD}{\mu^2} \tag{70}$$

The Prandtl number is defined as:

$$\mathrm{Pr} = \frac{\mu c_p}{k} \tag{71}$$

And the partial derivative of Pr with respect to μ, c_p, and k are:

$$\frac{\partial \mathrm{Pr}}{\partial \mu} = \frac{c_p}{k} \tag{72}$$

$$\frac{\partial \mathrm{Pr}}{\partial c_p} = \frac{\mu}{k} \tag{73}$$

$$\frac{\partial \mathrm{Pr}}{\partial k} = -\frac{\mu c_p}{k^2} \tag{74}$$

The friction factor is that used in (Dang, 2004), seen in Equation 61, which is a function of Re only. Its derivative is taken as:

$$\frac{\mathrm{d}f}{\mathrm{dRe}} = -\frac{A_1}{\mathrm{Re}[\ln(\mathrm{Re}) - A_2]^3} \tag{75}$$

Where $A_1 = 3.20124$ and $A_2 = 2.07486$.

The modified Gnielinski correlation, seen in Equation 57 is a function or Re, f, and Pr and its partial derivatives are:

$$\frac{\partial \mathrm{Nu}}{\partial \mathrm{Re}} = \frac{(f_\mathrm{f}/8)\mathrm{Pr}}{1.07 + 12.7\sqrt{f_\mathrm{f}/8}(\mathrm{Pr}^{2/3} - 1)} \tag{76}$$

$$\frac{\partial \mathrm{Nu}}{\partial f} = \frac{B_1 \mathrm{Pr}(\mathrm{Re_b} - 1000)\left[\sqrt{f_\mathrm{f}}\left(\mathrm{Pr}^{2/3} - 1\right) + B_2\right]}{\left[\sqrt{f_\mathrm{f}}(\mathrm{Pr}^{2/3} - 1) + B_3\right]^2} \tag{77}$$

Where $B_1 = 0.0139194$, $B_2 = 0.476601$, and $B_3 = 0.238301$, and:

$$\frac{\partial \mathrm{Nu}}{\partial \mathrm{Pr}} = \frac{C_1(\mathrm{Re_b} - 1000)\left[f_\mathrm{f}^{3/2}\left(\mathrm{Pr}^{2/3} - 3\right) + C_2 f_\mathrm{f}\right]}{\left[\sqrt{f_\mathrm{f}}(\mathrm{Pr}^{2/3} - 1) + C_3\right]^2} \tag{78}$$

Where $C_1 = 9.27962 \times 10^{-3}$, $C_2 = 0.714902$, and $C_3 = 0.238301$.

4. Results

Results are presented in chronological order of work performed, beginning with the experimental effort concerning semi-intrusive temperature measurement, for spatially realized temperature data. Results from the numerical studies using CFD, a bespoke 1D code, and single measurement uncertainty analysis follow.

4.1. Adaptation of Temperature-Sensitive Paint

Experiments were performed on acrylic and aluminum coupons coated with TSP. First, a simple pressure vessel was used to establish that the paint could survive and be used for temperature measurement after exposure to the harsh medium of a supercritical fluid. Following this, a more sophisticated apparatus was used to obtain data from a coupon while still immersed in the fluid.

4.1.1. Proof of Concept Results

Figure 4.1 is an image of the sCO_2 exposed coupon from initial work in a pressure vessel without optical access. The left image was taken under natural lighting of the TSP coated surface. Effect of the sCO_2 on the paint surface is clearly seen, resulting in pitting in the paint which was smooth prior to exposure. However, the paint was still well-bonded to the surface, and beyond the pitting, did not appear to be damaged on visual inspection. The image on the right was taken through the acrylic base, using the excitation light source to illuminate the coupon. From this image, impact of the sCO_2 exposure is striking. It is likely that the sCO_2 permeated into the acrylic coupon from the rough-cut edge, resulting in an internal reflection which seemed to provide some additional florescence.

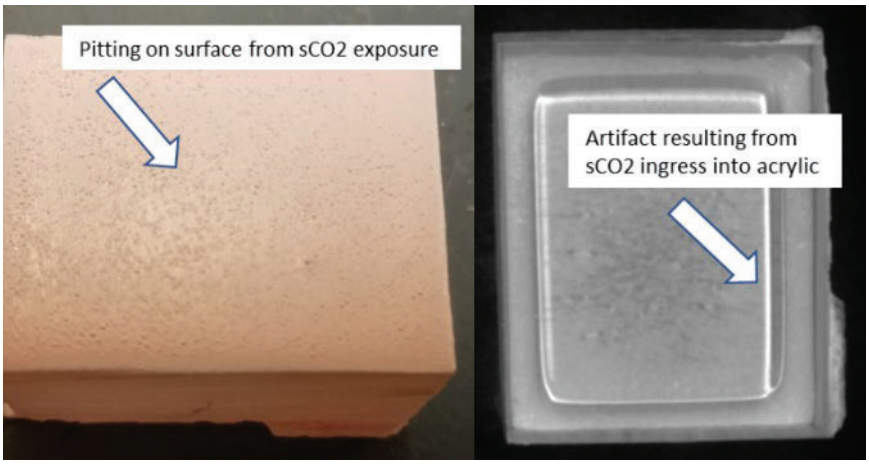

Figure 4.1 TSP coupon detail: effects of sCO_2 exposure

Figure 4.2 shows a comparison of the two samples illuminated by the UV excitation light source and captured by a pco.edge 4.2 scientific CMOS camera. This image is taken with the coated surface facing the camera, with the sCO_2 exposed sample on the left, and the control on the right, with both samples at room temperature. Surprisingly, the exposed coupon shows a higher room temperature intensity as compared to the control coupon. If the TSP were significantly degraded due to exposure, the intensity would be lower than the control. The increase in intensity may be the result of the increased surface roughness, the excitation of residual CO_2, or potentially an interaction between the sCO_2 and sensing particles (Cook, 1966; Omary, 2003; Wauchop, 1971). Whatever the cause, further investigation is necessary.

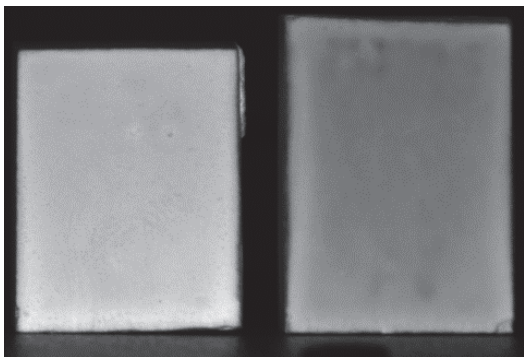

Figure 4.2 TSP coupons under excitation, left: exposed coupon, right: control coupon

To assess the impact of the sCO_2 exposure on the response of the TSP to temperature, both TSP coupons were placed with the TSP face-down on a heated copper plate. Images were captured at 4 temperatures, ranging from room temperature to approximately 76°C. Temperature uniformity of the copper plate was confirmed by the matching of 4 thermocouples within 0.5K. The surface averaged intensity at each temperature was normalized by the corresponding surface average room temperature intensity for each coupon as is done in a typical experiment. These results are plotted in Figure 4.3. Utilizing the hot intensity normalized by the room temperature intensity results in similar trends between the two samples. The largest difference was observed at a plate temperature of 50°C. This 7% difference in intensity ratio would translate to an error of 7K. This suggests that the underlying physical process inherent to the TSP sensing molecules has not been drastically altered, yet a re-calibration is necessary. Therefore, the likelihood of successful implementation of the temperature sensitive paint technique to a supercritical fluid is feasible; especially when one considers the potential use of protective coatings applied to the TSP.

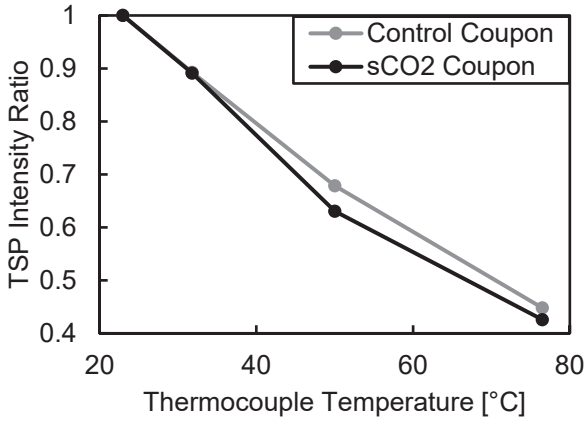

Figure 4.3 TSP coupon response comparison

4.1.2. Experimental Results

One coupon was selected from the batch prepared for this experiment for validation with respect to the previously established calibration curve. Figure 4.4 shows that the TSP agrees with thermocouple measurement within 1.3 ℃ in air. Error associated with both thermocouple and TSP measurements is taken as ± 1 ℃.

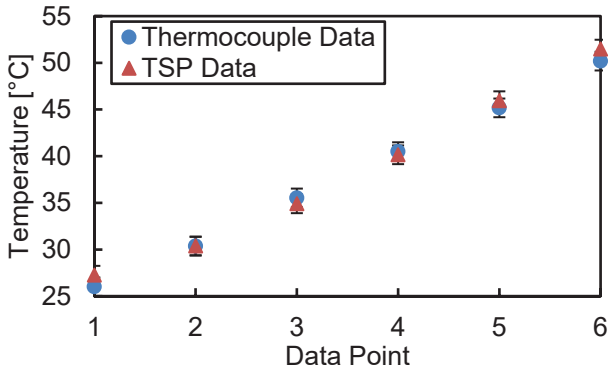

Figure 4.4 TSP measurement validation in air

Figures 4.5 – 4.10 present temperature data obtained from TSP post-processing for three coupons. Temperature data for the three reference conditions are compared with thermocouple data and plotted against time exposed to supercritical carbon dioxide. Each coupon has an exposed section and a section to which protective coating has been applied.

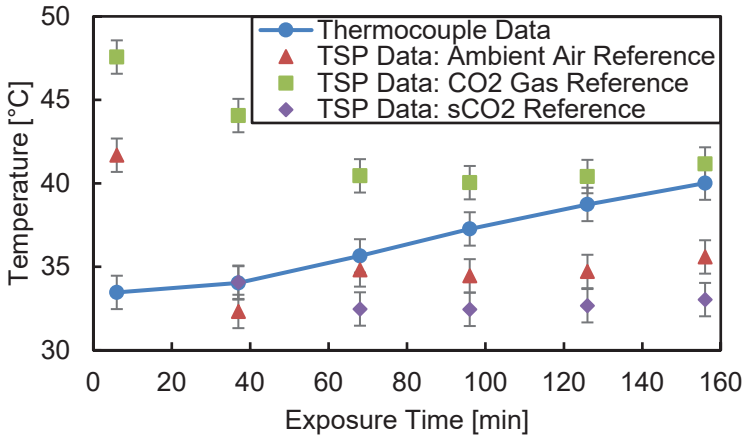

Figure 4.5 Coupon D: uncoated section

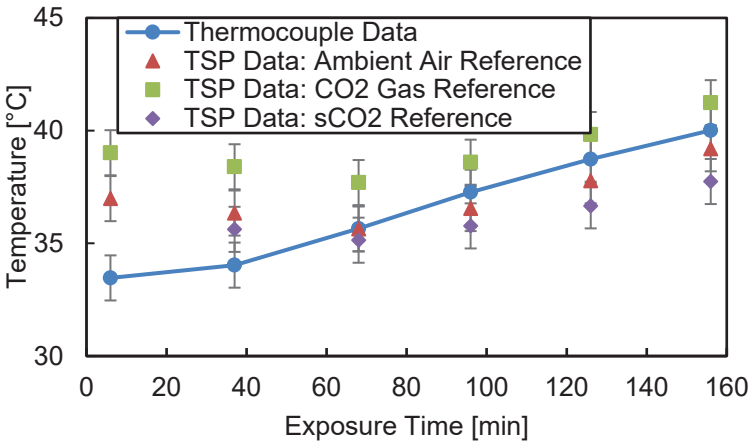

Figure 4.6 Coupon D: coated section

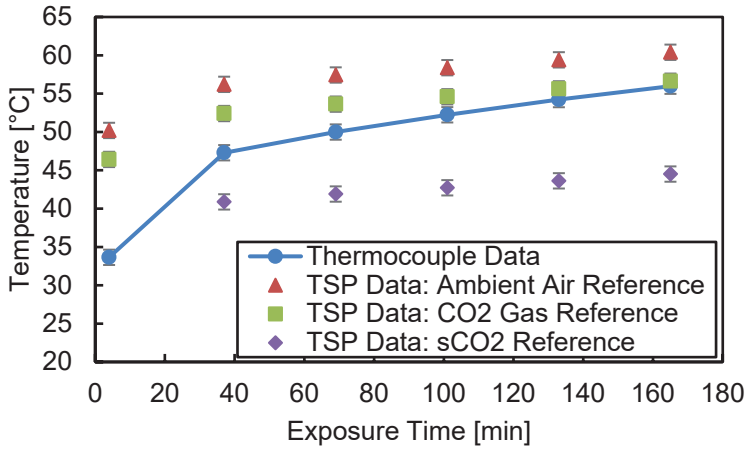

Figure 4.7 Coupon F: uncoated section

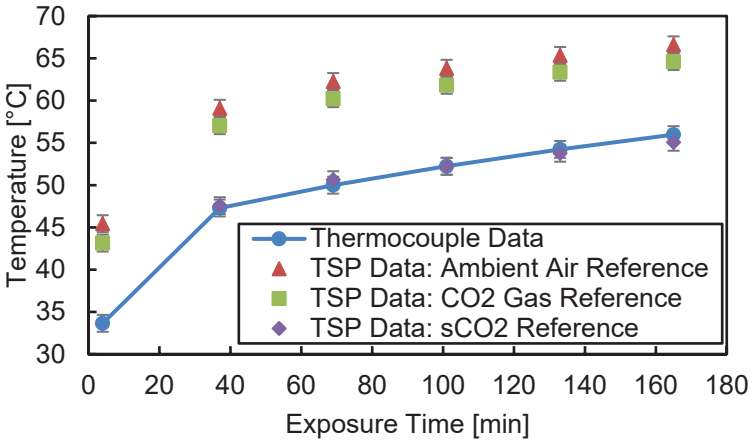

Figure 4.8 Coupon F: coated section

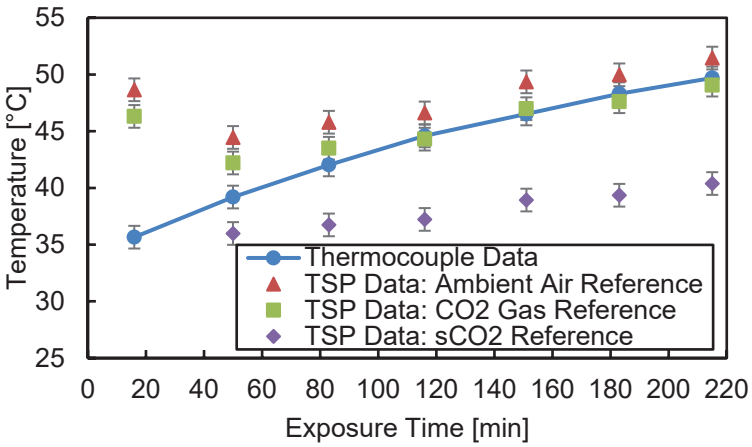

Figure 4.9 Coupon G: uncoated section

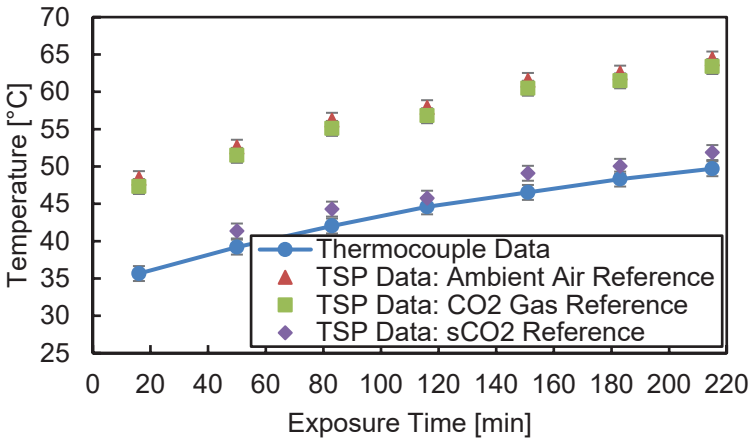

Figure 4.10 Coupon G: coated section

The impact of reference image selection on TSP temperature prediction is pronounced. Selecting an ambient air condition tends to lead to a temperature over prediction, whether or not a coating is used. As excited TSP intensity is inversely proportional to temperature, this suggests a significant reduction in transmissivity between sea level air or gaseous CO_2 and supercritical CO_2. Further investigation with spectroscopy is required to determine whether this is driven by increased attenuation of the ultraviolet excitation light or the visible light emitted by the TSP, or if both are attenuated equally. The most accurate results arise when both reference and data images

are taken in a supercritical fluid.

The data further suggest that use of a clear coating or sealant is desirable. Ingress of sCO_2 into the TSP is seen in previous and current work and has a significant impact on temperature prediction, although the mechanism of this effect is unknown. Future testing in air will be performed on TSP coupons exposed to sCO_2 to ascertain the effect on the previously established calibration curve.

Finally, these data point to a decrease in TSP temperature prediction performance near the critical temperature. Coupon D data shows relatively poor agreement between thermocouple data and sCO_2-referenced TSP data, even with use of a protective coating. The author suggests this again arises from a stronger attenuation of light near the critical point, and an analysis of the intensity of the relevant spectrum is desired. Coupons F and G show good agreement between thermocouple data and TSP temperature prediction for coated sections, using a sCO_2 reference image. For these cases, TSP underpredicts a maximum of 0.9 °C for Coupon F and over predicts a maximum of 2.6 °C for Coupon G. These discrepancies are not significantly greater than those traditionally seen in experiments in air.

The effect of sCO_2 exposure on the TSP surface is shown in Figures 4.11 – 4.13. The left side of the coupons was left uncoated and shows effects of exposure to the supercritical fluid. The right side was treated with 4 light coats of a popular commercially available polyurethane sealant.

Figure 4.11 Coupon D texture: 156 min total exposure

Figure 4.12 Coupon F: 152 min total exposure

Figure 4.13 Coupon G: 217 min total exposure

Bubbling of the TSP surface as a result of sCO_2 ingress is seen here, similar to that observed in coupons prepared on acrylic backing from earlier work. The resulting rough surface has a propensity to cast shadows on itself should the excitation light source be not completely normal to the surface. This can have the effect of reducing the amount of light captured by the camera and lead to an overprediction of temperature using the traditional calibration curve. The polyurethane coating allows the surface to remain much smoother during exposure but still is not impervious to sCO_2 ingress. Larger bubbling features are observed with varying severity. Variation in coating surface degradation between Coupon D and Coupon F suggests that coating performance is a function of operating temperature, as Coupon F experienced higher fluid temperature for a similar exposure time. Variation in degradation between Coupon F and Coupon G suggests, unsurprisingly, that coating performance is also a function of exposure time, as these

coupons were exposed to similar fluid temperature, with Coupon G exposed for a further 65 minutes.

4.2. Cylindrical Pin-Fin Array

Simulations were conducted parametrically, and data is obtained for four principal test cases. Baseline cases were run using air modeled as ideal gas at one atmosphere, first using geometry from previous validated CFD and again at geometry scaled down by a factor of 12, representative of sCO_2 turbine blade internal cooling geometry to confirm there were no scaling effects. A series of cases simulating a compressor bleed cooling flow at 30 MPa was run with a Reynolds number range from 2,000 to 167,000. Three transcritical series follow, first at constant inlet temperature 300 K and Reynolds number ranging from 1,000 to 15,000. Next, the impact of varying inlet temperature near the critical temperature was studied at constant Reynolds number. Finally, inlet temperature was varied at constant mass flux with Reynolds numbers from 5,000 to 13,000. Case series 1-3 include a case at Re = 15,000. A summary of case series is presented in Table 4.1.

Table 4.1

Case matrix

Series	Fluid	Inlet Cond.	D_{pin} [m]	G [kg/m^2-s]	Re
a	Air	330 K / 0.1 MPa	0.015 (validated case)	19	15 k
b	Air	330 K / 0.1 MPa	0.00125	227	15 k
1	sCO_2	330 K / 30 MPa	0.00125	120 – 10,600	2 k – 167 k
2	Transcritical CO_2	300 K / 7.4 MPa	0.00125	46 - 737	1 k – 15 k
3	Transcritical CO_2	300–306K / 7.4 MPa	0.005	280 – 737	15 k
4	Transcritical CO_2	300 - 306 K / 7.4 MPa	0.005	240	5 k – 13 k

Results of Nusselt number for variable Reynolds number series, averaged over the pin and bottom endwall surfaces, are presented in log-log format in Figure 4.14. Nusselt number for variable inlet temperature series are compared in linear format in Figure 4.15.

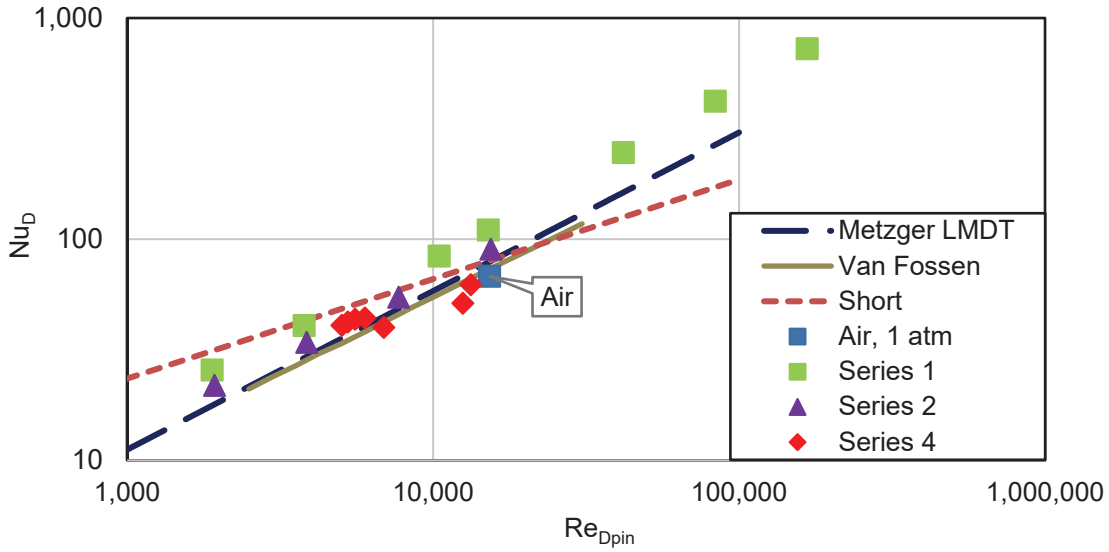

Figure 4.14 Average Nusselt number vs. Reynolds number

A heat transfer enhancement relative to correlations established in air was seen for the high pressure sCO_2 flow in Series 1, considerably far from the critical point. The trend of Nusselt number vs. Reynolds number in this regime appeared to match established correlations, although at increased magnitude, for this liquid-like area of the supercritical regime. The same behavior was observed in the transcritical fluid of Series 2.

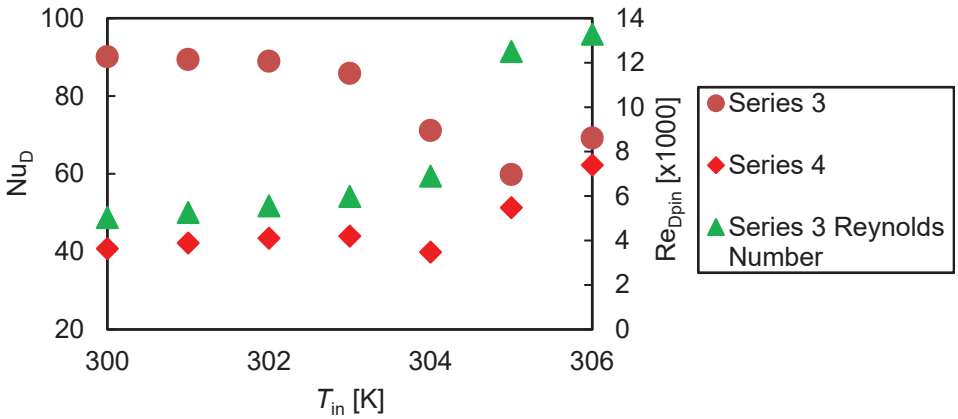

Figure 4.15 Nusselt number vs. inlet temperature

The considerable variation in Reynolds number at fixed mass flux (Series 4) is effected by dramatic fluid property gradients across this temperature range, as shown in Figure 4.16. The variation in Nusselt number for both the fixed-Re and fixed-G case series is striking over a 6 K range of inlet temperature, again arising from severe thermodynamic and transport property change near the critical point. This suggests that Reynolds number alone is not a sufficient nondimensional parameter in sCO_2 flows near T_{pc}. Heat transfer performance is seen to be highly sensitive to inlet temperature, and for this reason results are plotted against inlet temperature rather than bulk temperature in Figure 4.15.

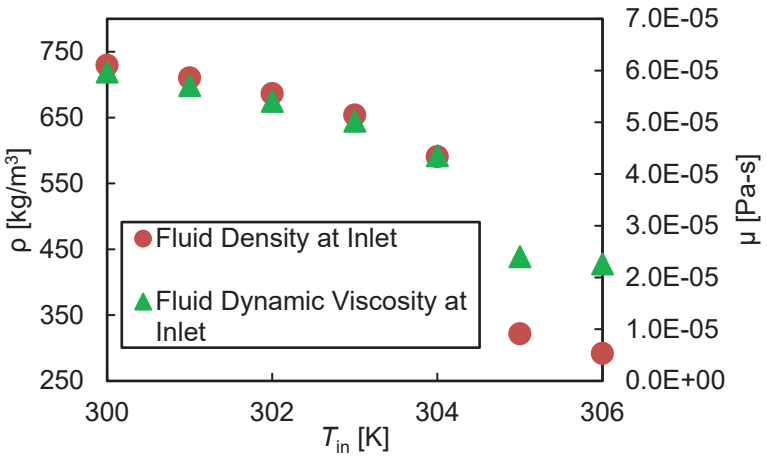

Figure 4.16 Transcritical fluid properties, 7.4 MPa isobar

A local Nusselt reduction is seen at inlet temperature 304 K, and this is due to the peak of thermal conductivity at the pseudocritical temperature, as shown in Figure 4.17. This indicates there was not a corresponding peak in heat transfer coefficient for this case, an explanation for which follows.

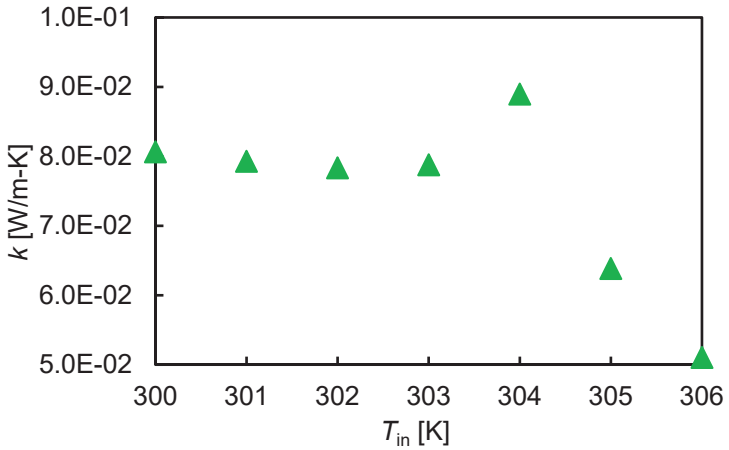

Figure 4.17 Thermal conductivity near T_{pc}, 7.4 MPa isobar

Friction factor is plotted against Reynolds number for varying-Re series in Figure 4.18.

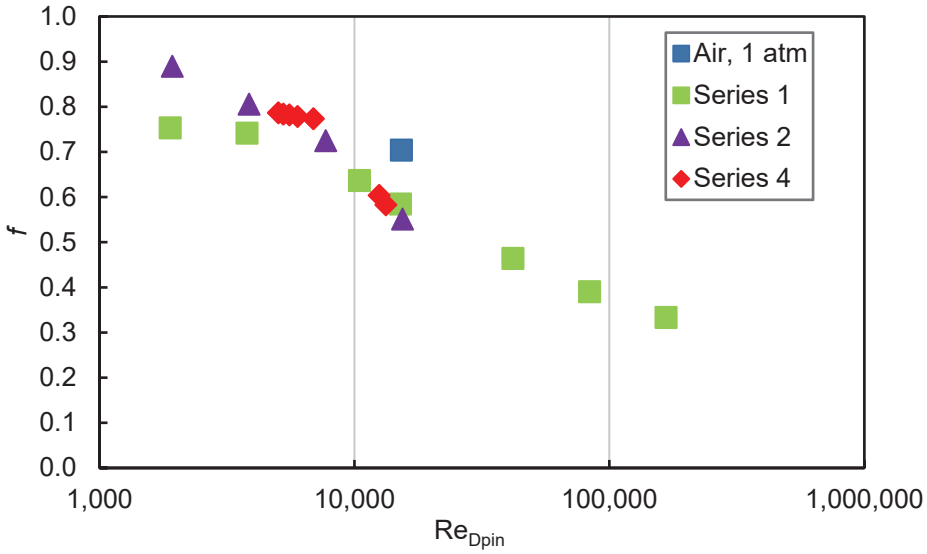

Figure 4.18 Darcy friction factor vs. Reynolds number

This follows the expected trend as viscous friction is increasingly dominated by inertial forces with increasing Reynolds number. A more relevant metric is obtained when Nusselt number and friction factor are normalized with respect to the baseline pin-fin channel with air at 1 atm and at constant Reynolds number and hydraulic diameter. A measure of relative heat transfer device performance is obtained in Figure 4.19. At the

center of the plot is a baseline case through which flows air at 1 atm. The plot is divided into four quadrants. Quadrants I and II contain results indicating a favorable heat transfer performance relative to baseline, and quadrants II and III correspond to an improvement in friction factor performance. Quadrant II is the union of these two cases and contains most results. The exception is one case lying in quadrant III, which corresponds to the aforementioned dip in Nusselt number at inlet temperature 305 K and 7.4 MPa. The majority of results, however, suggest an important benefit to employing trans- and supercritical flows in heat transfer devices.

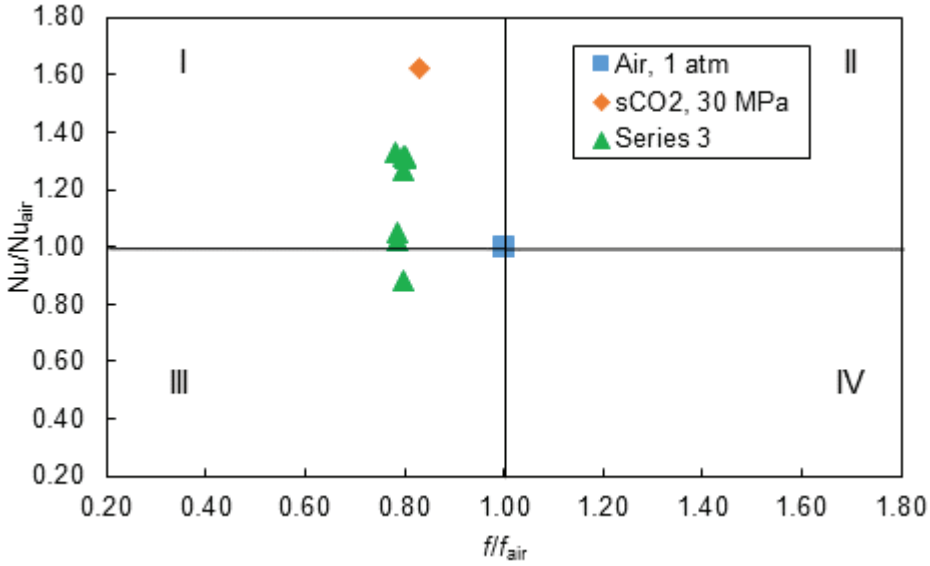

Figure 4.19 Normalized Nusselt number vs. normalized friction factor, Re = 15k

The transcritical deterioration in Nusselt number is next investigated. Streamlines in the wake of the first row center pin are taken on a plane at mid pin, colored with velocity magnitude normalized with respect to inlet velocity, and are shown for air at 1 atm, sCO_2 at 30 MPa, and transcritical CO_2 at 7.4 MPa, all at Re = 15 k in Figure 4.20, Figure 4.21, and Figure 4.22.

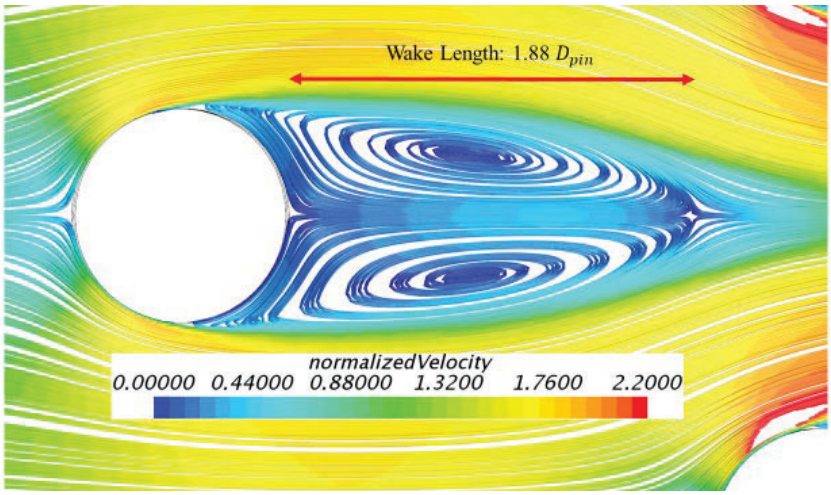

Figure 4.20 Row 1 center pin wake streamlines: air at 1 atm, Re = 15k

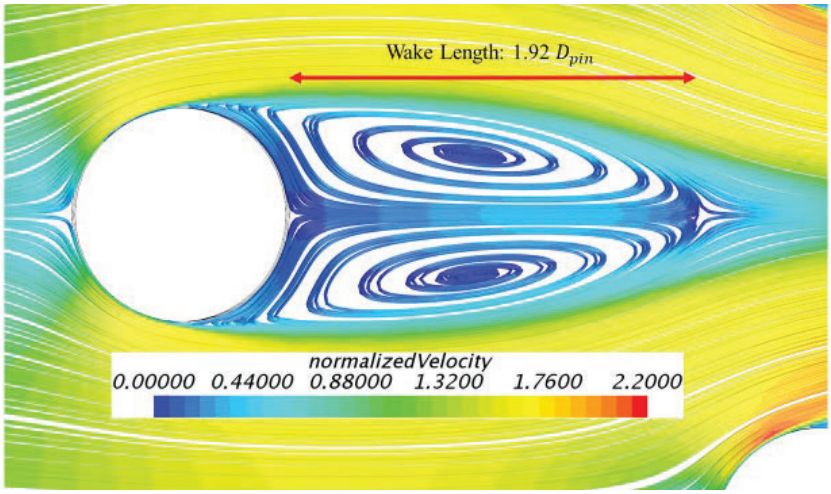

Figure 4.21 Row 1 center pin wake streamlines: sCO_2 at 30 MPa, Re = 15k

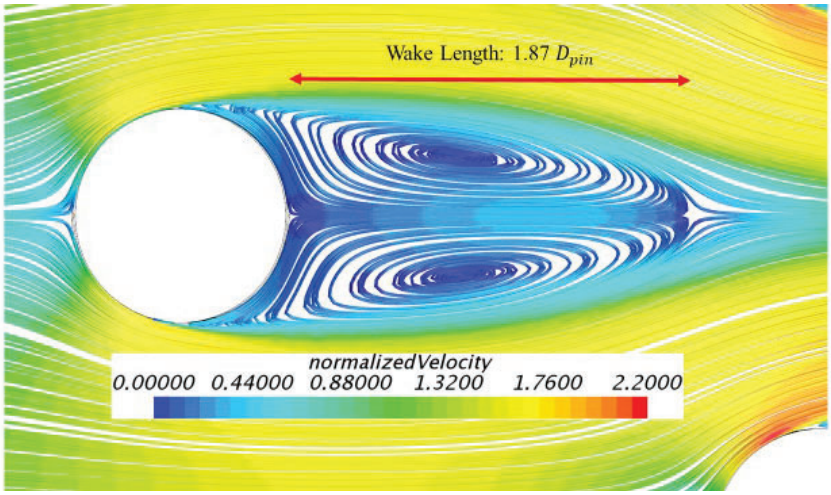

Figure 4.22 Row 1 center pin wake streamlines: transcritical CO_2 at 7.4 MPa, Re = 15k

It is clear that there is no appreciable difference in wake size at this Reynolds number across thermodynamic regimes. It must be noted that the effect of body forces (either gravity or rotation) was not thoroughly studied here and is proposed for future work. However, it can be shown that the impact of buoyancy due to gravity (oriented in the pin-axis direction) is not significant at the range of mass flux and Reynolds numbers studied here. Local Nusselt number and shear stress magnitude distribution are plotted around the circumference of the same first row, center pin in Figure 4.23.

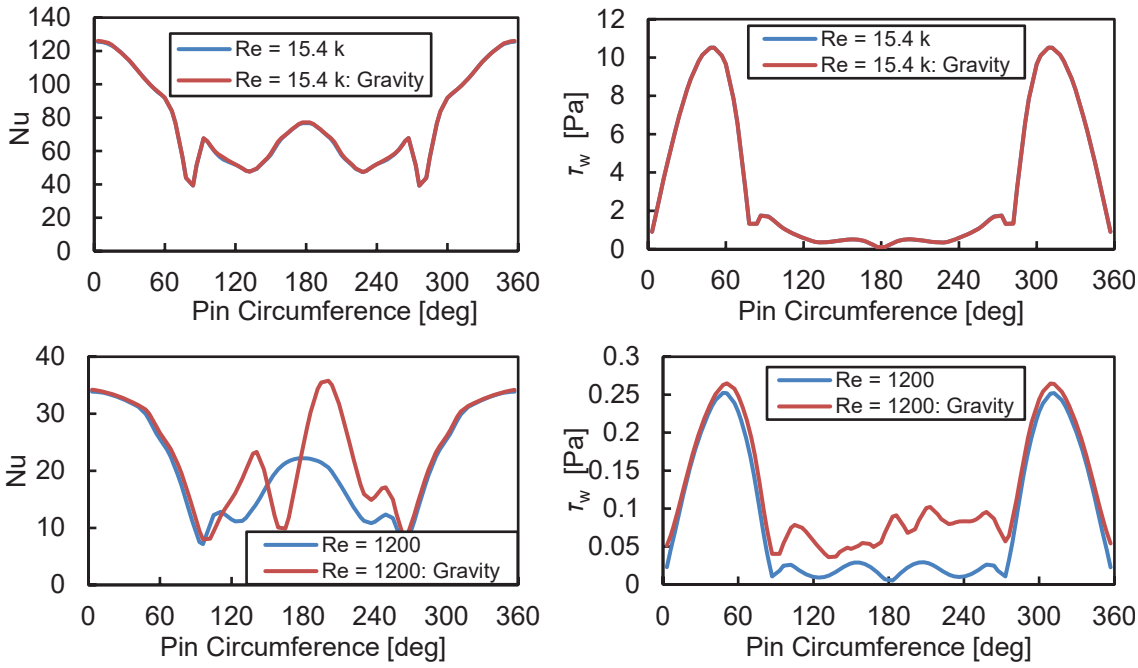

Figure 4.23 Buoyancy effects, current cases vs. low Re case

Further, an isometric view of streamlines in the wake of the row 1 center pin are provided in Figures 4.24 – 4.27 to illustrate how the impact of buoyancy on flow isotropy is only significant at very low Reynolds numbers.

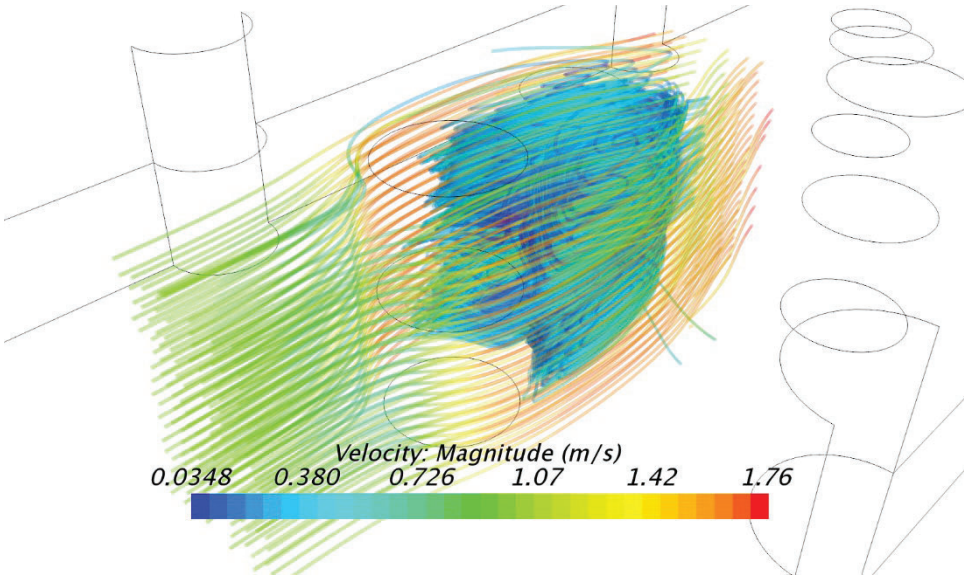

Figure 4.24 Row 1 center pin wake streamlines: transcritical CO_2 at 7.4 MPa, Re = 15k, no gravity.

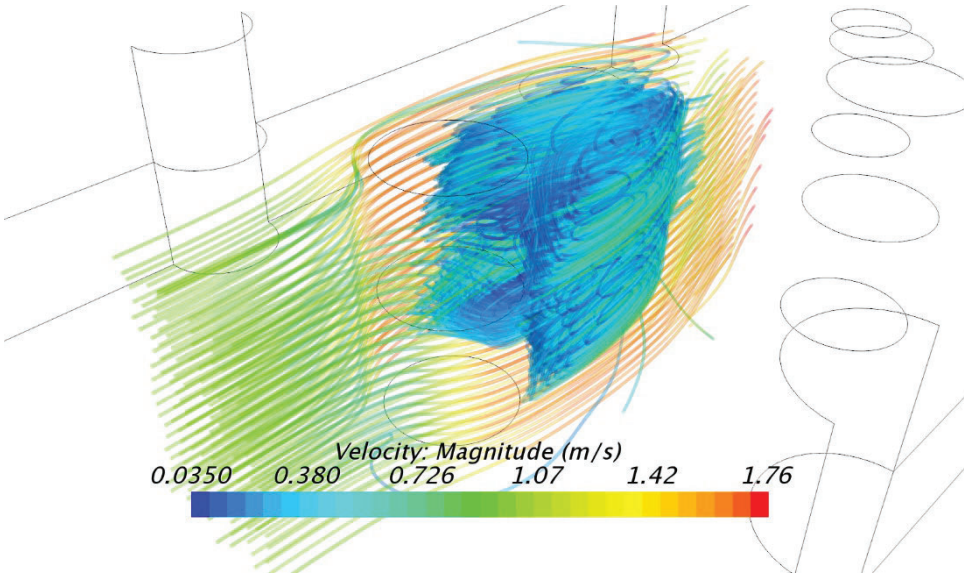

Figure 4.25 Row 1 center pin wake streamlines: transcritical CO_2 at 7.4 MPa, Re = 15k, with gravity.

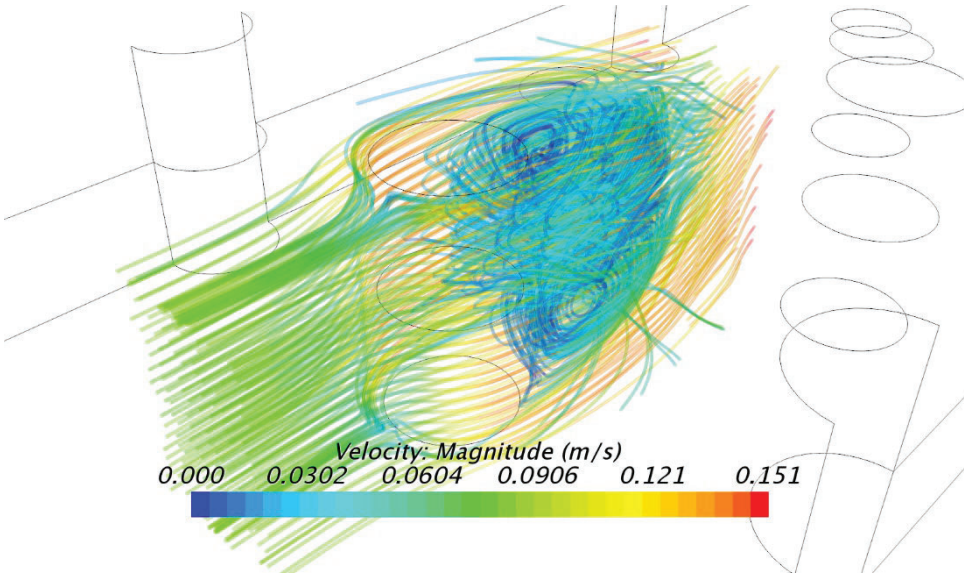

Figure 4.26 Row 1 center pin wake streamlines: transcritical CO_2 at 7.4 Mpa, Re = 1,200, no gravity.

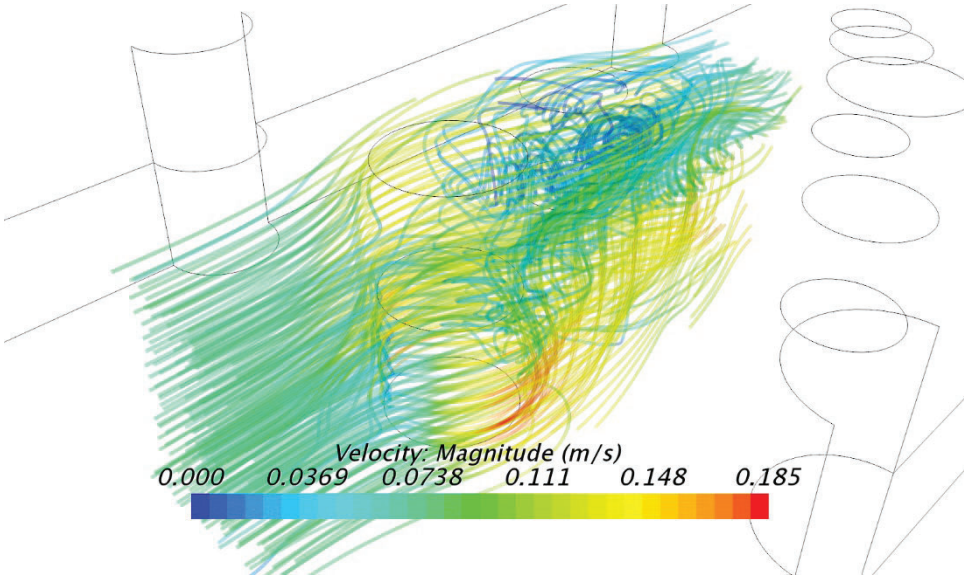

Figure 4.27 Row 1 center pin wake streamlines: transcritical CO_2 at 7.4 MPa, Re = 1,200, with gravity.

No appreciable change in flow physics is observed by introducing a body force due to gravity at the Reynolds numbers being studied here. By contrast, significant anisotropy arises from buoyancy forces in the wake of pins at Re ≈ 1,200. It is suggested that the absence of any enhancement in heat transfer coefficient at the thermodynamic location of

the thermal conductivity peak is the result of the rapid diffusion by the turbulent flow of any boundary layer containing fluid at these favorable conditions. A decrease in Nusselt number arises from this phenomenon. Further study of the impact of buoyancy on low Reynolds number trans- and supercritical CO_2 in turbulated cooling flows is desired to better characterize these flows.

4.3. Reduced-Order Model

Wall temperature and HTC prediction of the one-dimensional code is presented here over a range of inlet temperatures that cross the pseudocritical temperature at 8 MPa, from 306 K to 312 K. Results are shown first for the modified Gnielinski correlation seen in Equation 57 using a Prandtl number calculated at bulk temperature only in Figure 4.28 - Figure 4.34. CFD cases with corresponding inlet conditions were run for this purpose without gravity, for simplicity.

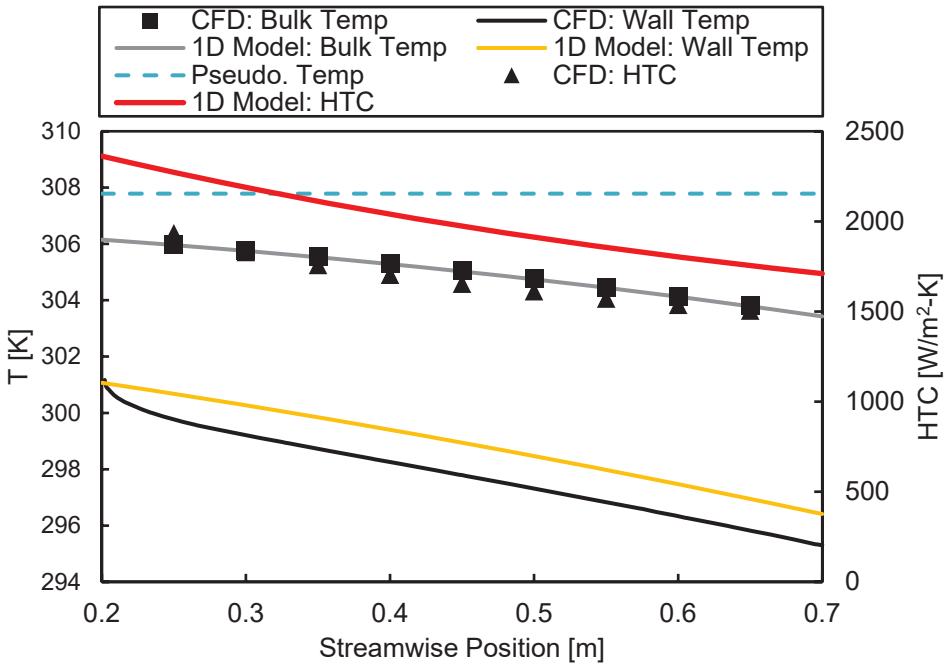

Figure 4.28 Temperature and HTC predictions: 1D model compared with CFD results, $T_{\text{inlet}} = 306\,\text{K}$.

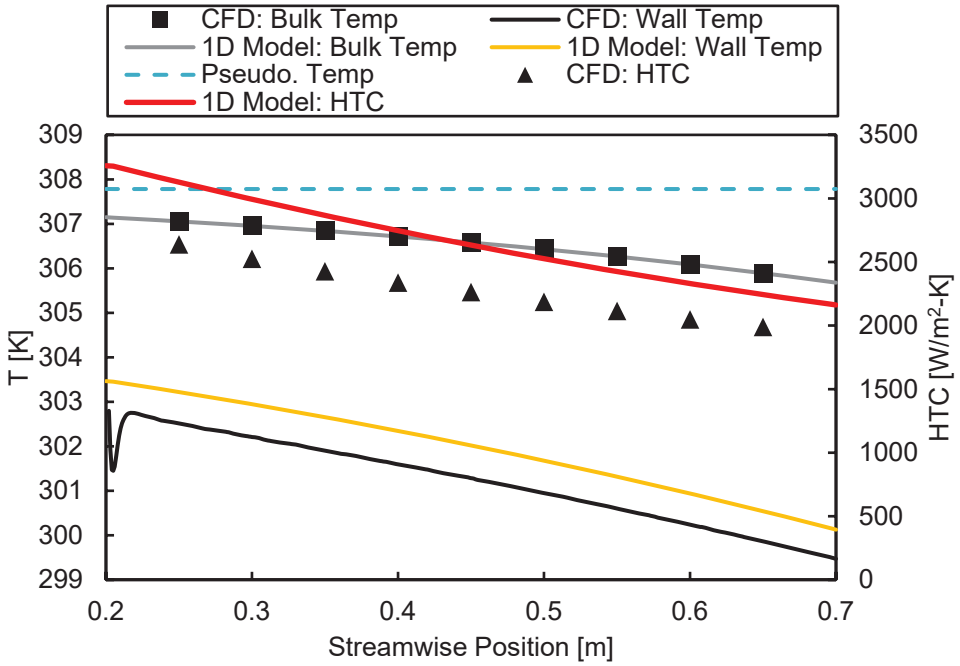

Figure 4.29 Temperature and HTC predictions: 1D model compared with CFD results, $T_{\text{inlet}} = 307\,\text{K}$.

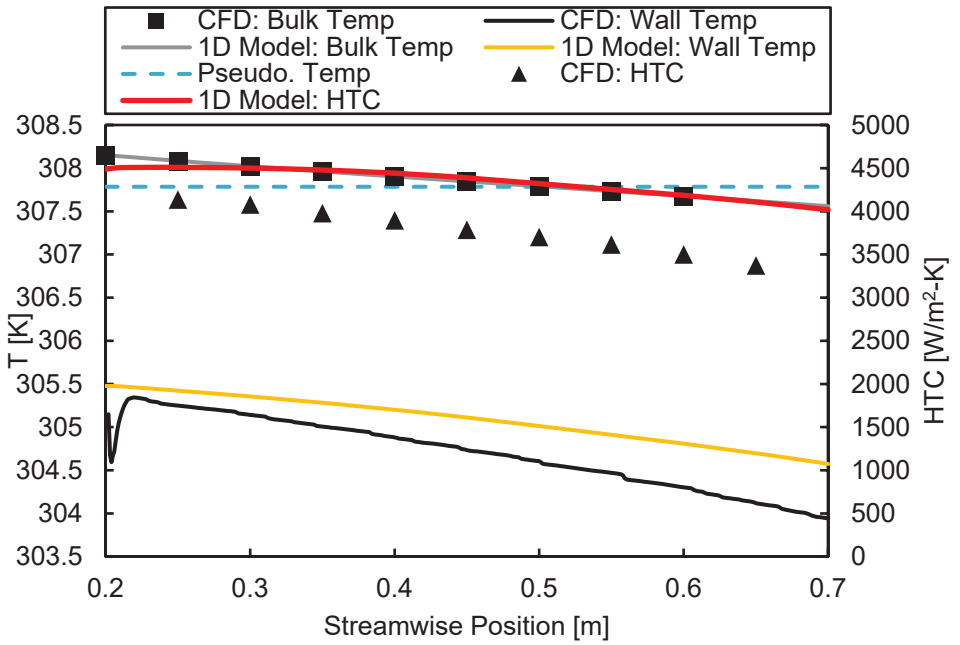

Figure 4.30 Temperature and HTC predictions: 1D model compared with CFD results, $T_{\text{inlet}} = 308\,\text{K}$.

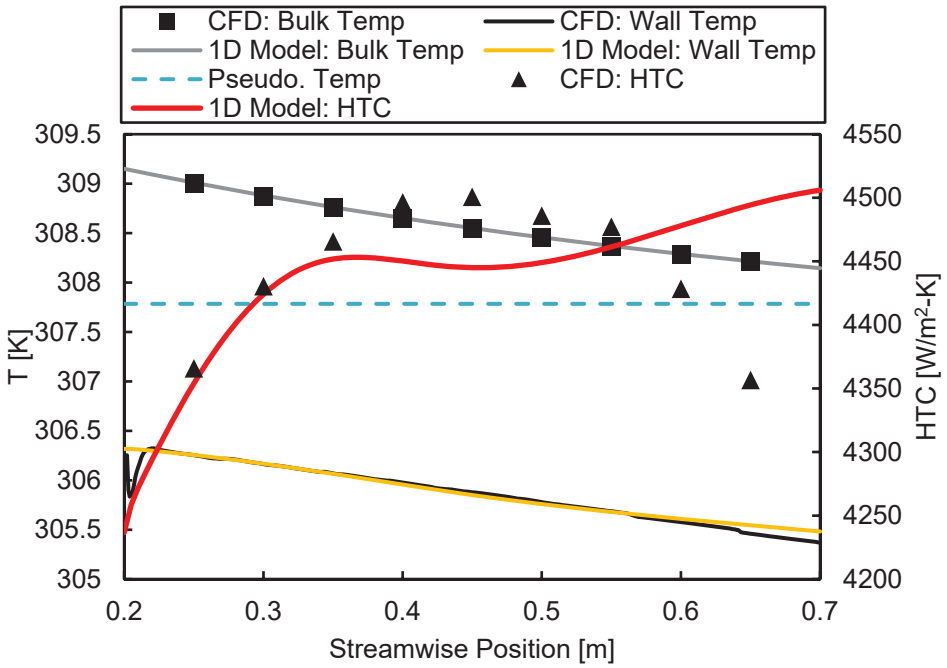

Figure 4.31 Temperature and HTC predictions: 1D model compared with CFD results, $T_{\text{inlet}} = 309\,\text{K}$.

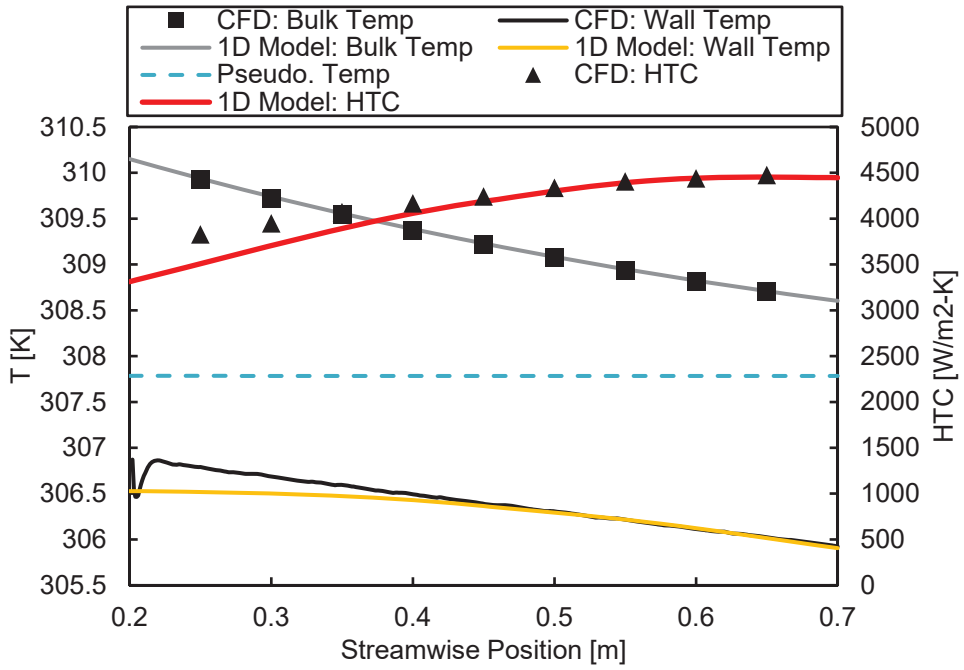

Figure 4.32 Temperature and HTC predictions: 1D model compared with CFD results, $T_{\text{inlet}} = 310\,\text{K}$.

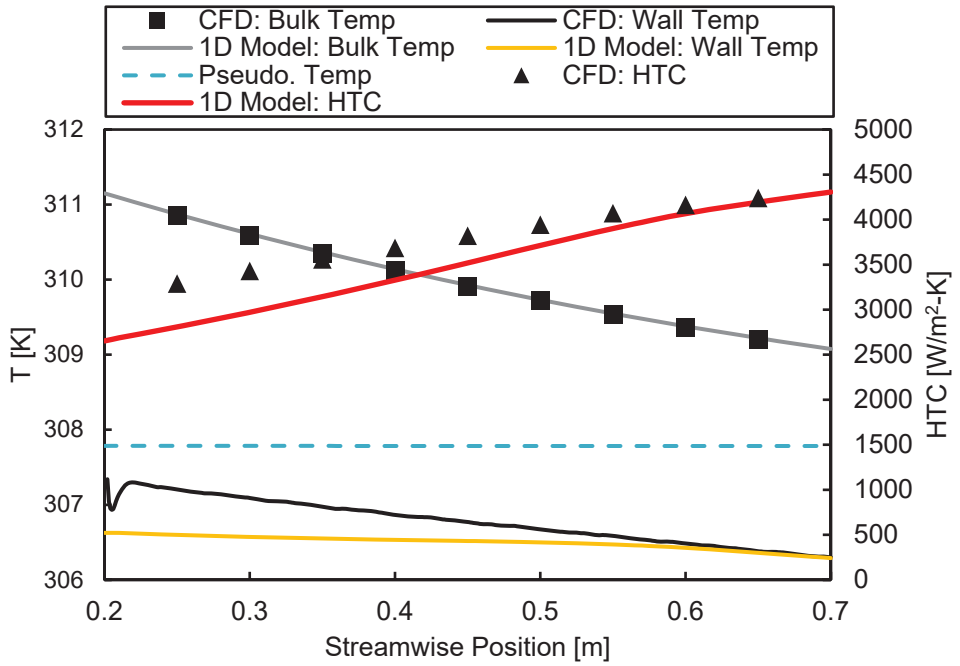

Figure 4.33 Temperature and HTC predictions: 1D model compared with CFD results, $T_{\text{inlet}} = 311\,\text{K}$.

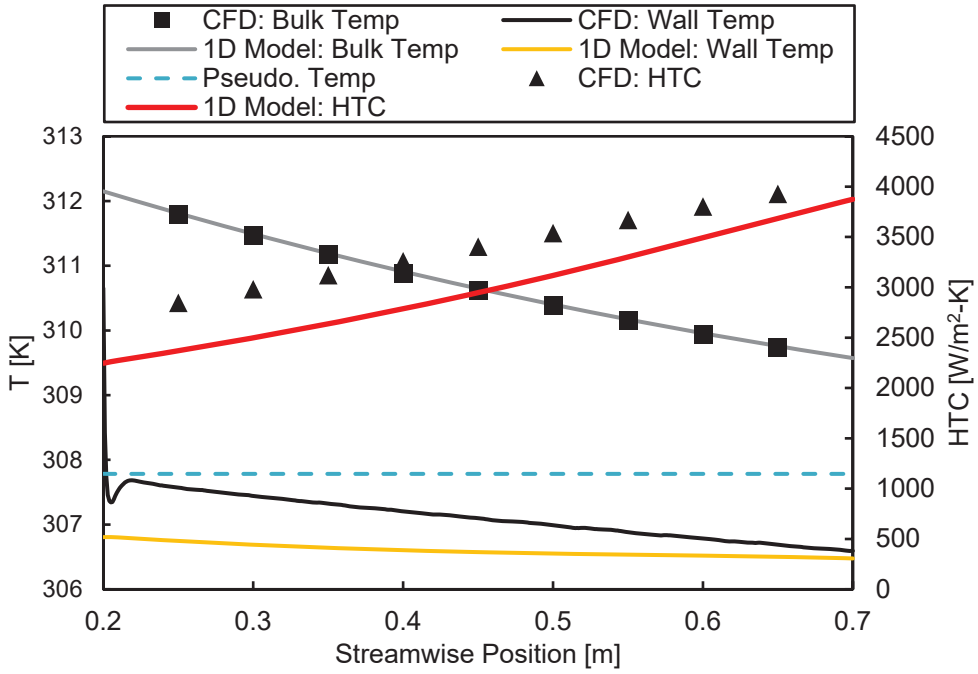

Figure 4.34 Temperature and HTC predictions: 1D model compared with CFD results, $T_{\text{inlet}} = 312\,\text{K}$.

The reduced-order model performs a simple heat balance for finite volume

experiencing a constant heat flux, so bulk temperature prediction matches well with CFD, as expected. The 1D code in this configuration, however, shows a slight overprediction of T_w (underprediction of ΔT and overprediction of HTC) with respect to CFD for $306 < T_{inlet} < 308$ K, and a slight underprediction of T_w (overprediction of ΔT and underprediction of HTC) for $T_{inlet} = 311$ K and 312 K. Model performance is very good for $T_{inlet} = 309$ K and 310 K, which is interesting as these represent the test cases most closely straddling the pseudocritical line, and overall nearest T_{pc}. Due to rapidly changing properties, and small deviation in wall temperature can result in significant HTC differences, and this is most striking for the $T_{inlet} = 309$ K case. Results from the 1-D model employing the adaptive Prandtl number according to Equation 59 are shown in Figure 4.35 - Figure 4.38.

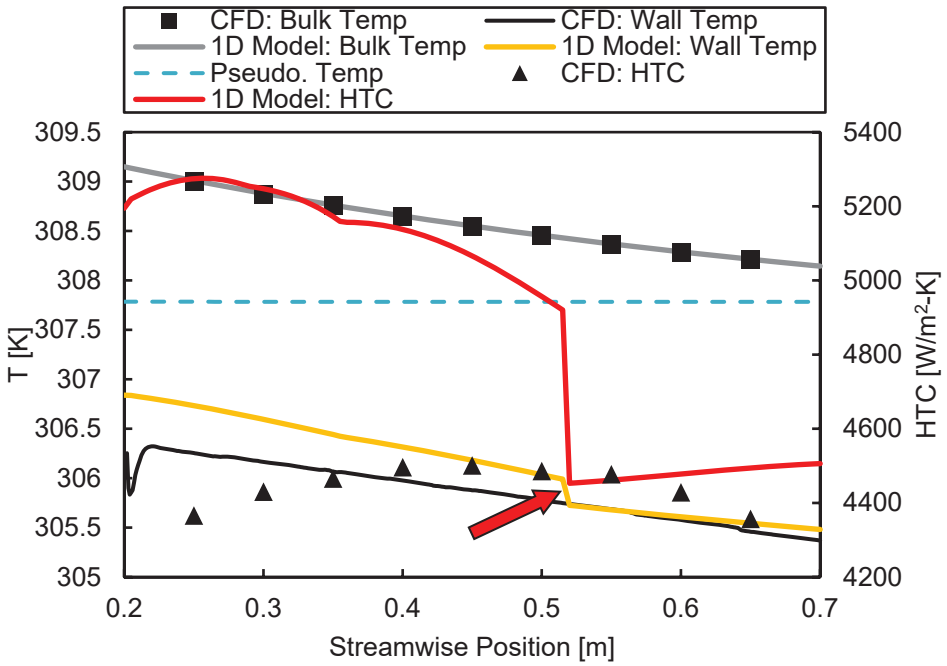

Figure 4.35 Temperature and HTC predictions: 1D model with adaptive Pr formulation compared with CFD results, $T_{inlet} = 309$ K.

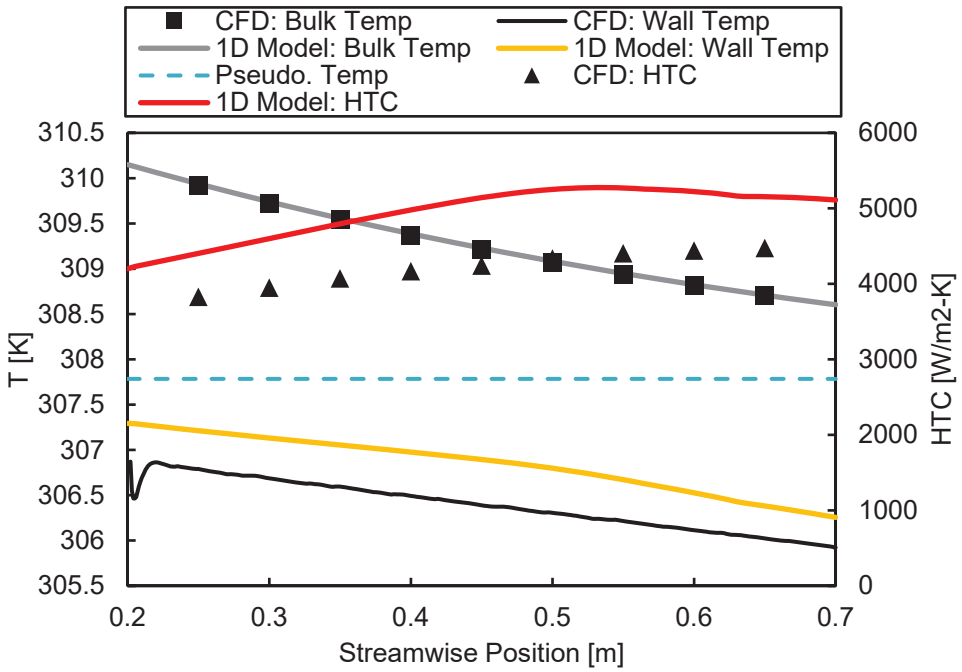

Figure 4.36 Temperature and HTC predictions: 1D model with adaptive Pr formulation compared with CFD results, $T_{\text{inlet}} = 310$ K.

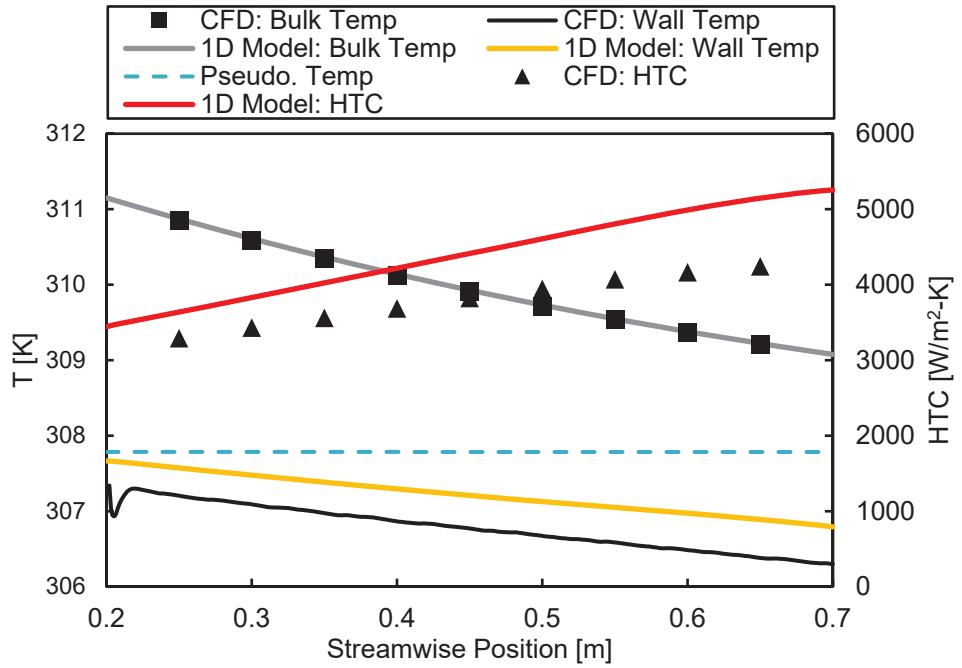

Figure 4.37 Temperature and HTC predictions: 1D model with adaptive Pr formulation compared with CFD results, $T_{\text{inlet}} = 311$ K.

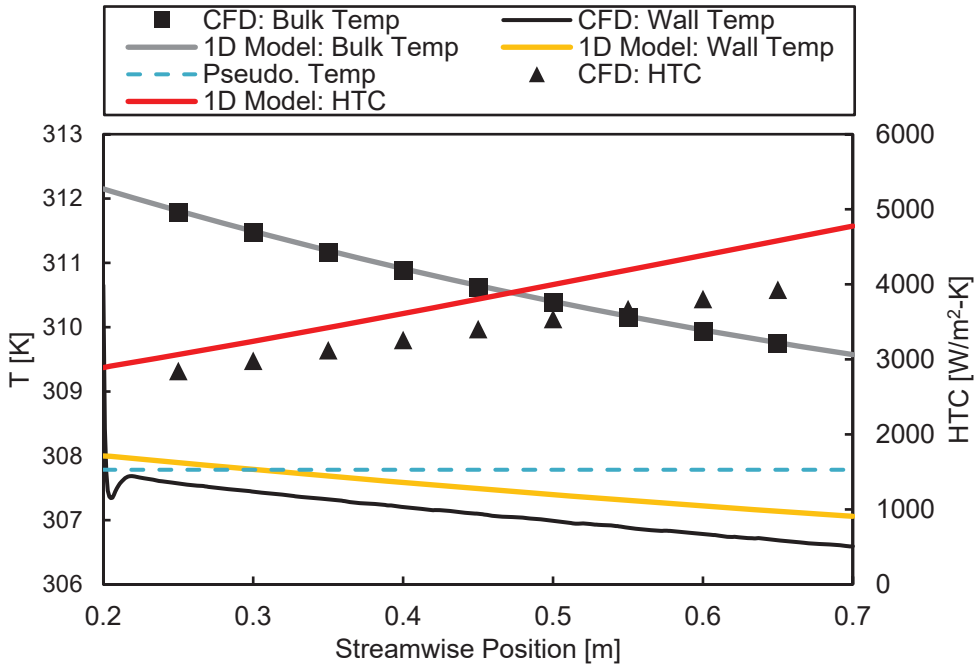

Figure 4.38 Temperature and HTC predictions: 1D model with adaptive Pr formulation compared with CFD results, $T_{\text{inlet}} = 312\,\text{K}$.

A change in Prandtl formulation is invoked starting at $T_{\text{inlet}} = 309\,\text{K}$ and continues at higher inlet temperatures. The effect of the switch case on wall temperature prediction is most noticeable at this temperature in Figure 4.35, and this is indicated by the red arrow. For cases below $T_{\text{inlet}} = 309\,\text{K}$, $c_{p_\text{b}} \geq \overline{c}_p$, the first of the three possible cases. At 309 K, the inlet condition is such that $c_{p_\text{b}} < \overline{c}_p$ with $\mu_\text{b}/k_\text{b} \geq \mu_\text{f}/k_\text{f}$, which is the second case. At $x = 0.36\,\text{m}$, this second condition reverses, leading to the third case. At $x = 0.52\,\text{m}$, the case reverts to $c_{p_\text{b}} \geq \overline{c}_p$, the first case again, and this is where the temperature discontinuity indicated by the red arrow is seen. This is the only case where the code demonstrates this behavior. From the results thus far, it would seem the inclusion of an adaptive Prandtl number does little to help the fidelity of the code. The average HTC results are plotted against each inlet temperature case in Figure 4.39.

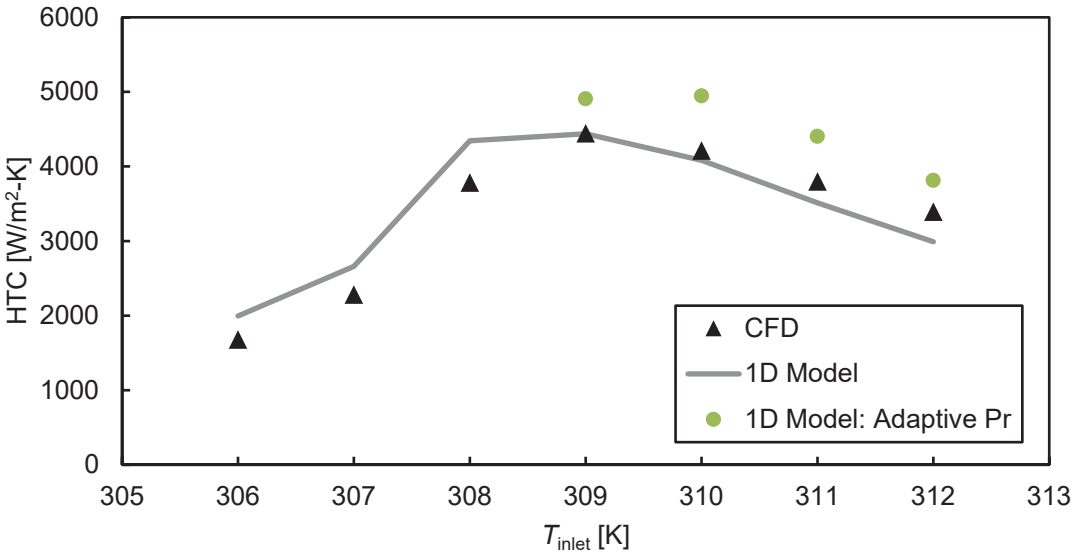

Figure 4.39 Average HTC prediction performance vs. T_{inlet}: 1D model compared with CFD results.

Better agreement is demonstrated here by the 1-D code employing the simplified approach using Pr_b only, however, if average HTC predictions are compared against the original experimental values once more and plotted against the predicted average bulk temperature, the result suggests some logic behind the more sophisticated formulation.

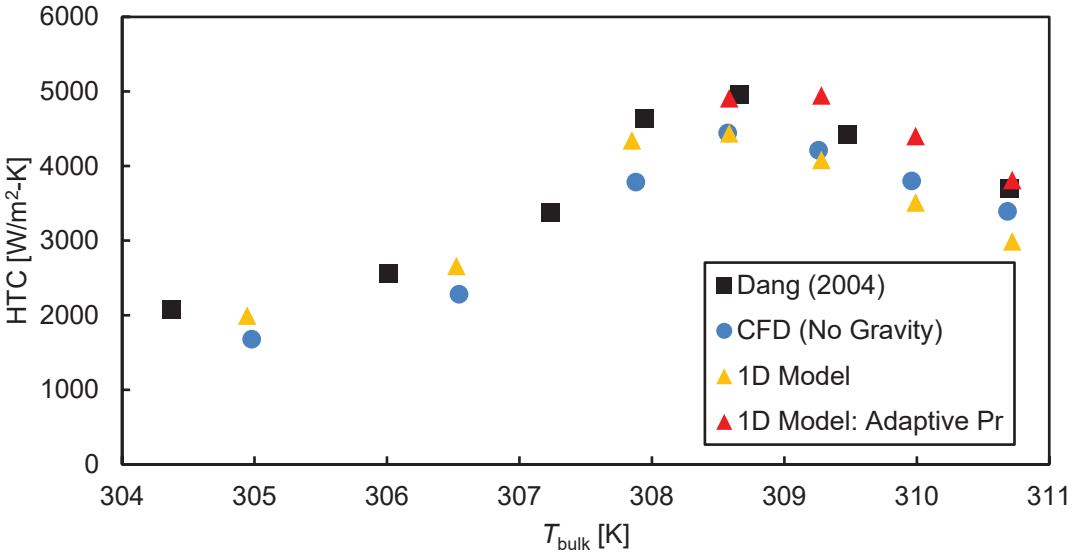

Figure 4.40 Average HTC prediction performance vs. T_{bulk}: 1D model compared with CFD results and experiment.

At T_b above the pseudocritical HTC peak, better agreement is demonstrated by the adaptive Pr cases. The CFD results to which the reduced-order method has erstwhile been compared were obtained without simulating gravity. This suggests buoyancy plays a larger role than was previously considered in development of the correlation from (Dang, 2004), a surprising result in pipes of such small diameter.

The reduced-order method developed here can be considered, if not a design tool, then an illustrative one, being capable of replicating experimental heat transfer behavior within the bounds of often reported experimental uncertainty in much of the heat transfer literature ($\pm 15\%$). This method is next brought to bear on a flow condition more likely to be encountered in the recuperators of a sCO_2 Brayton cycle, nearer the critical point, and near the pseudocritical line at 7.5 MPa (the current geometry lends itself to this rather well, current $D_\mathrm{h} = 6\,\mathrm{mm}$, and $D_\mathrm{h} \leq 6\,\mathrm{mm}$ for most PCHE flow paths) (Kwon, 2020). Figure 4.41 - Figure 4.43 show temperature and absolute pressure predictions for possible recuperator flows. The dashed green line highlights the proximity of these flows to the pseudocritical line, indicating the pressure at which $T_\mathrm{b} = T_\mathrm{pc}$ at each streamwise location.

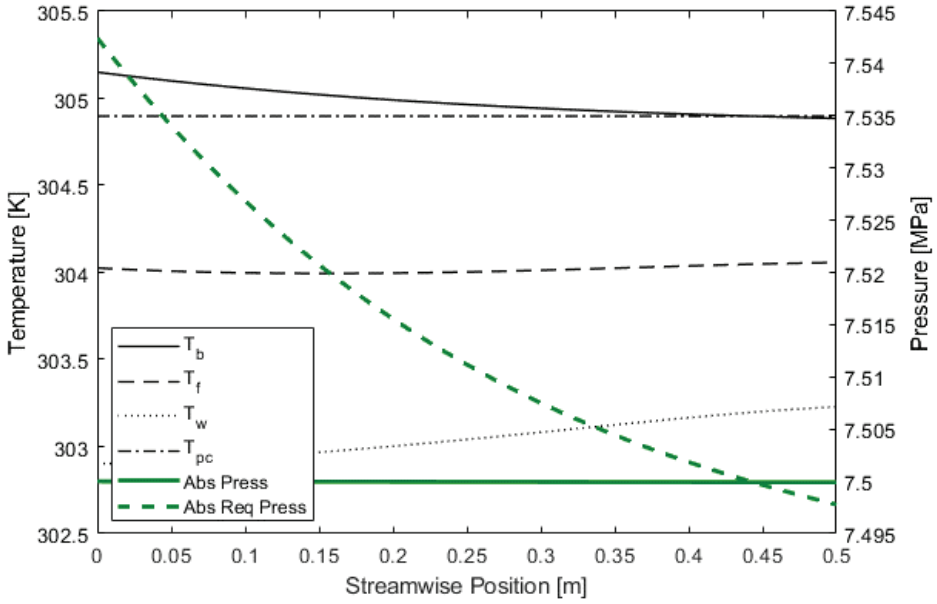

Figure 4.41 Temperatures with pressure target, recuperator conditions, $T_{\text{inlet}} = 305\,\text{K}$

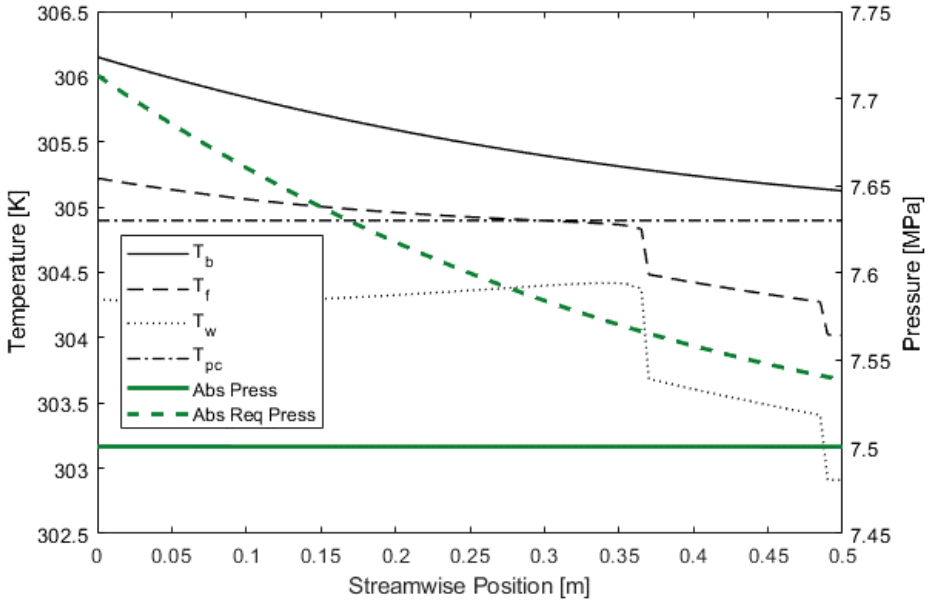

Figure 4.42 Temperatures with pressure target, recuperator conditions, $T_{\text{inlet}} = 306\,\text{K}$

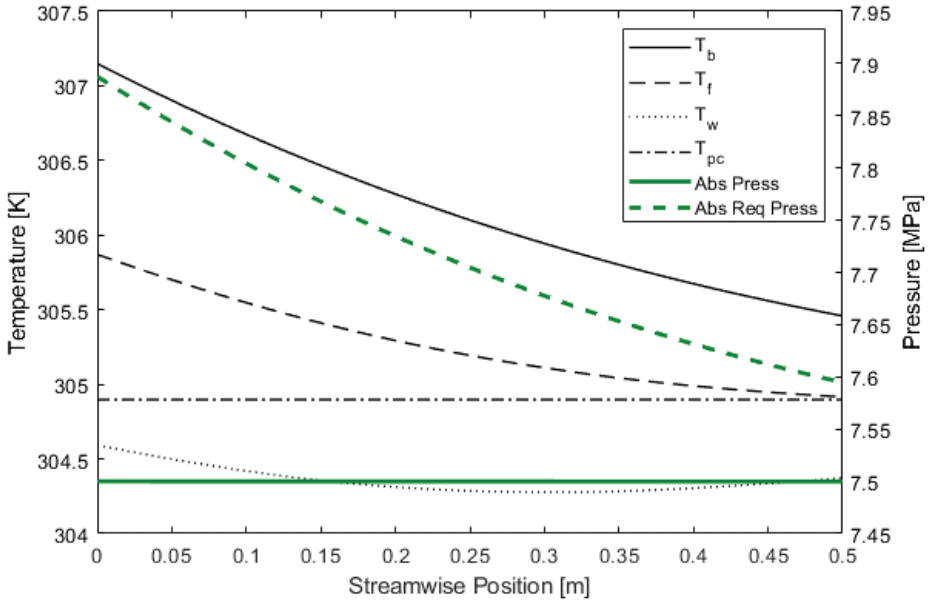

Figure 4.43 Temperatures with pressure target, recuperator conditions, $T_{\text{inlet}} = 307\,\text{K}$

Heat flux remains the fixed value ($-12\,\text{kW/m}^2$) from experiment, which may not be representative of these applied flows. Care must be taken at these lower pressures if it is not desired that the fluid enters the liquid phase, which is the case for the near-wall fluid at $T_{\text{inlet}} = 305\,\text{K}$ and $306\,\text{K}$. Still, these data suggest a significant increase in HTC may be achieved with a modest increase in static pressure in the recuperator flow, perhaps through the use of a diffuser of appropriate area ratio. The flow could be expanded through a nozzle after a suitable heat transfer length.

4.4. Uncertainty in the Critical Region

It is useful to first plot uncertainties in fluid properties only, focusing on the region from 7.5 to 8.5 MPa to highlight the growth of the uncertainty peaks approaching the critical point. The fluid property uncertainties (represented as percentages as calculated below) are presented as surfaces in Figure 4.44 (colored to provide depth).

$$\%\ \text{uncertainty} = 100 \times \frac{\delta R(T,P)}{R(T,P)} \tag{79}$$

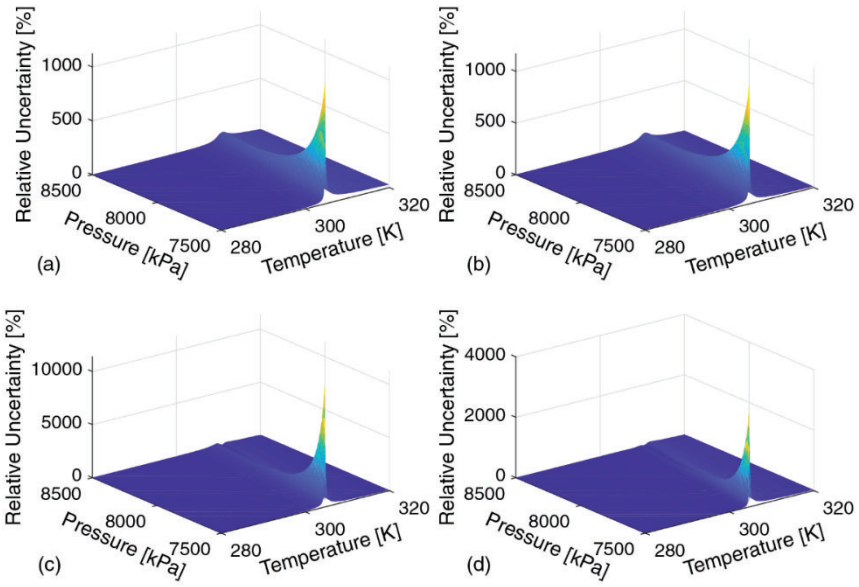

Figure 4.44 Fluid property relative uncertainty surfaces: (a) ρ (b) μ (c) c_p (d) k

Overlays of relative property uncertainties on 7.5, 8, and 8.5 MPa isobars are shown in Figure 4.45.

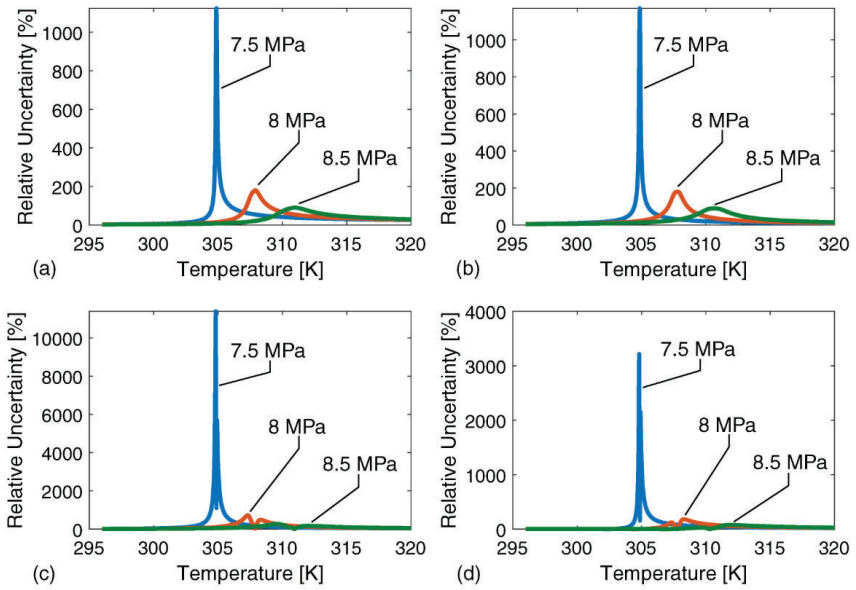

Figure 4.45 Fluid property relative uncertainty isobars: (a) ρ (b) μ (c) c_p (d) k

Surfaces and overlays on isobars of relative uncertainty for calculated quantities Re, Pr, f, and Nu are presented in Figure 4.46 and Figure 4.47.

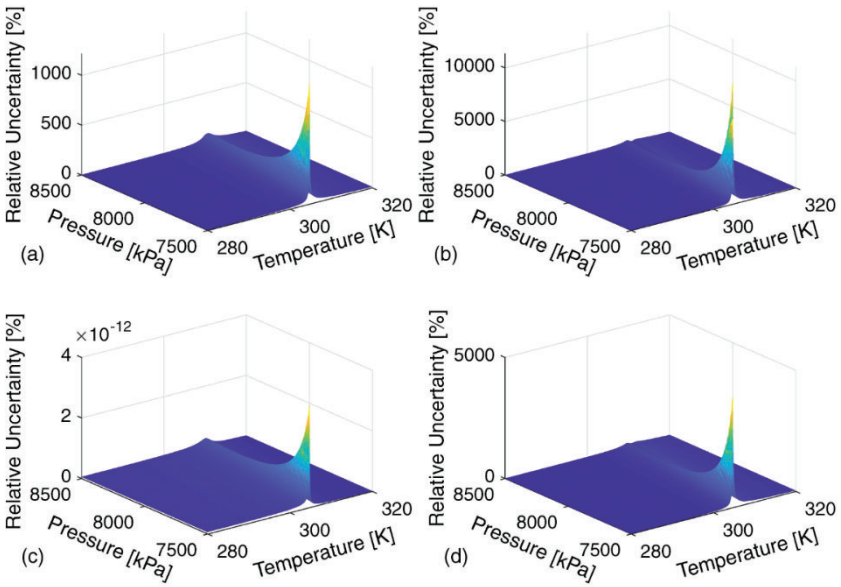

Figure 4.46 Calculated property relative uncertainty surfaces: (a) Re (b) Pr (c) f (d) Nu

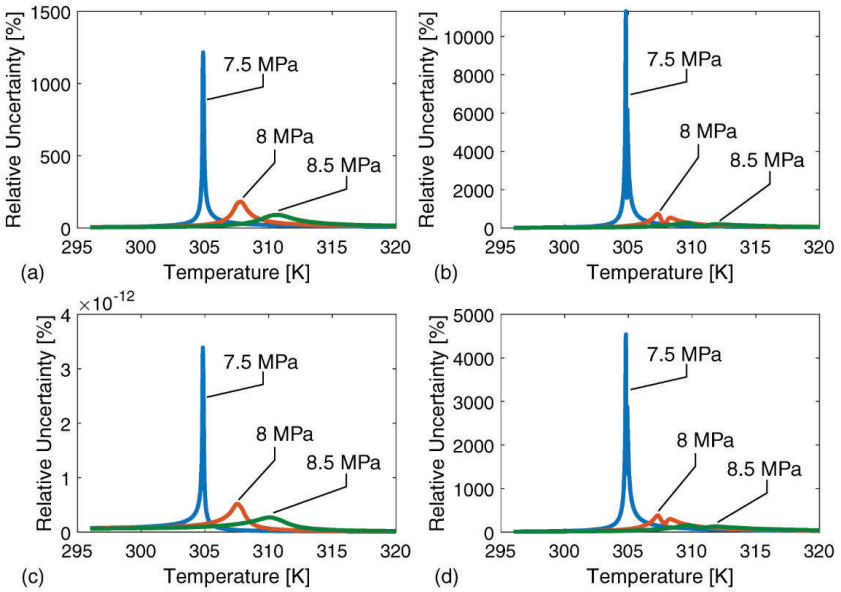

Figure 4.47 Calculated property relative uncertainty isobars: (a) Re (b) Pr (c) f (d) Nu

Tabulated maxima are presented in Table 4.2.

Table 4.2

Uncertainty maxima

	Maximum Relative Uncertainty [%]		
	7.5 MPa	8 MPa	8.5 MPa
ρ	1124	180	90
μ	1171	181	90
c_p	11397	719	269
k	3213	180	77
Re	1215	182	90
Pr	11315	739	279
f	3×10^{-12}	5×10^{-13}	3×10^{-13}
Nu	4538	381	160

It is both expected and clear from the data that thermodynamic regions with large fluid property gradients will be accompanied by large uncertainties. What remains striking is that even at higher operating pressures further away from the critical point, common in the experimental literature (such as 8 MPa), uncertainties very near the pseudocritical temperature are anywhere from two to seven times a given property value. In the absence of measurement devices with arbitrarily small uncertainties, it is currently very difficult to use experimental data to construct holistic and meaningful correlations for heat transfer prediction that are agnostic to geometric dimensions or thermodynamic conditions.

Behavior near the critical point itself is expectedly volatile, but this data shows even at conditions several atmospheres of pressure above this point, error propagation to

calculated values Re, Pr, and Nu is severalfold the value. The error propagation to f, in its current formulation, is shown as very small. It is calculated here as a function of Re only, which itself is a function solely of μ at a constant mass flux. Viscosity enjoys the gentlest gradients of the fluid properties studied here near the critical point and along the pseudocritical line, leading to a significantly reduced error propagation. Friction factor can therefore be calculated for these flows with relative confidence.

For the remaining calculated quantities, it is an understatement that these data suggest difficulty will arise in implementing novel Nu correlations for even simple flow geometries in this thermodynamic regime.

5. Conclusions

The theme arching over the results of this work is the call for more spatially resolved data in heat transfer research. To facilitate a wholistic understanding of heat transfer to supercritical flows, not only is a larger dataset required, but also a consistent method of data reduction and reporting. The best evidence for this is the substantial spatial variation in heat transfer quantities revealed during the comparison of CFD results to experimental data in horizontal pipes, which also highlights the impact of selection of reference quantities. Key findings for the several investigations are summarized below.

5.1. Semi-Intrusive Temperature Measurement

Recommendations following from this work for future experiments in sCO_2 heat transfer are as follows:

1. TSP reference images should be taken in the supercritical state.
2. TSP for supercritical fluids should be coated in a thin layer of protective coating, with a matte finish, and compatible with the TSP base layer.
3. A new calibration curve is desired for very near the critical point.

A spectral analysis of the above procedure, particularly near the critical point, is desired to determine a possible need for modification of the TSP calibration curve in this regime. Further investigation of repeatability of TSP temperature prediction across multiple sCO_2 exposure sessions is crucial to understand performance degradation vs. time in supercritical fluid. A variety of protective coatings and coating techniques should be investigated to compare resistance to attack by sCO_2 and impact on temperature prediction.

5.2. Cylindrical Pin-Fin Array

Average Nusselt number vs. Reynolds number predictions for high-pressure sCO_2 suggest a good agreement with the trend of existing correlations, and with that of Metzger and Haley (1982) specifically. As the conditions at compressor exit in these sCO_2 Brayton cycles are relatively distant from the critical point, a return to liquid-like behavior is expected, and the observed trend matching supports this. A lightly modified correlation can be proposed, as a function of Reynolds number alone, based on these results:

$$\mathrm{Nu}_D = 0.0836\,\mathrm{Re}^{0.751} \tag{80}$$

A Nusselt vs. Reynolds correlation is possible in the transcritical region but will also be a function of bulk fluid properties, as is the case with the more sophisticated previously established correlations, such as that of Short (2002), as well as ratios of wall vs. bulk viscosity and thermal conductivity as seen in the literature. This early effort can suggest the following correlation for Nusselt number for inlet conditions of 300 K and 7.4 MPa:

$$\mathrm{Nu}_D = 0.149\,\mathrm{Re}^{0.6613} \tag{81}$$

It is clear further investigation is required to more fully characterize both the local and averaged thermal behavior of transcritical CO_2 flows in these cooling geometries. A Reynolds number and mass flux parametric study is desired at a range of thermodynamic states surrounding the critical point to generate a more complete picture of heat transfer. Also, experimental validation of any proposed correlations is crucial. The proposed, more complete numerical work in this area will inform the design and implementation of future experimental efforts in characterizing heat transfer in turbulated flows of trans- and supercritical CO_2.

A far more relevant body force than gravity in internal turbine blade cooling flows is forces arising from high-speed rotation. Rotation was not studied in-depth in this study, but one exploratory case was run at low angular speed (5 RPM) to suggest the significant effect of high rotation rate on transcritical CO_2 flows, even at the moderate Reynolds numbers covered here. To mitigate crossflow by virtue of the right and left periodic boundaries, these were changed to adiabatic walls, resulting in a 1.6 % increase in average Nusselt number and 9.1 % increase in static pressure drop relative to the corresponding non-rotating case. Local Nusselt number and shear stress magnitude distributions on the row 1 center pin are plotted in Figure 5.1 to demonstrate the impact of a modest rotation.

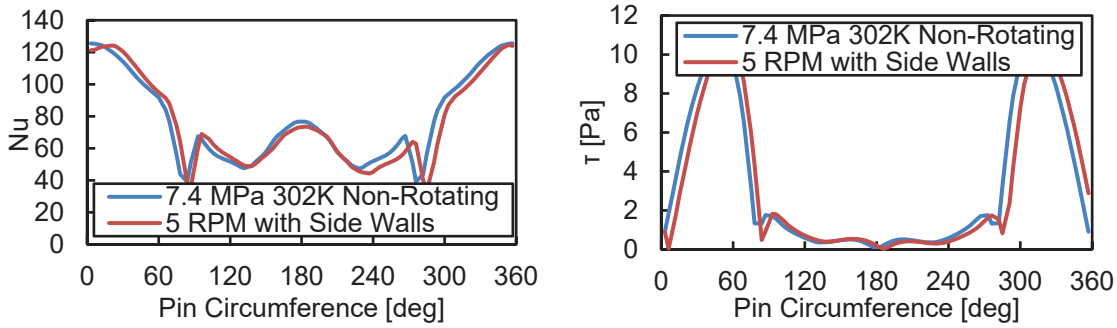

Figure 5.1 Effect of rotation on Nusselt number and wall shear stress distributions: sCO_2 at 7.4 Mpa, $\mathrm{Re} = 15\,\mathrm{k}$.

Considering rotation rates in real-world application are orders of magnitude larger, this is significant behavior and will be relevant to heat transfer performance, particularly should asymmetrical flow turbulators be considered, and is indicative that due to the large magnitude of body force in rotating turbomachinery, buoyancy effects will manifest at much larger Reynolds numbers. This is significant in coolant flows near the critical point.

5.3. Reduced-Order Model

The obstacles encountered in obtaining a functional Pr_{eff} frustrate highly accurate heat transfer performance from the one-dimensional code. As a greater amount of CFD data is gathered, the use of machine learning as a pattern recognition tool could be illuminating in predicting heat transfer quantities as a function in various $T_{b,r}$ and $T_{w,r}$ regimes. The method, as it currently exists, can a valuable computationally tractable "what if" tool to investigate what small changes in heat exchanger operating points can effect in terms of heat exchanger thermal and hydraulic performance. In recuperator flows, very close to the critical pressure, small changes (and potentially small irreversibilities) could pay dividends, manifesting in significant increases in heat transfer.

5.4. Uncertainty in the Critical Region

The fluid properties of sCO_2 vary significantly near the critical point and along the pseudocritical line, in some cases leading to deviation from expected heat transfer behavior, and, in turn, introducing modeling difficulties. A study was performed to determine the impact of measurement uncertainty both on calculated real fluid properties and the associated impact on predicted heat transfer rates using existing correlations. Results indicate that due to the strong sensitivity of fluid temperature and pressure on thermal and transport properties, even at conditions significantly above the critical pressure, uncertainties are much greater than those seen in subcritical flows. Uncertainty in c_p near T_{pc} at operating pressures commonly seen in literature (8 MPa) is above 700% and remains above 250% even 10 atmospheres above the critical pressure. Resulting uncertainty in calculated Pr and Nu is of similar magnitude, posing a significant impediment to the creation of dimensionless heat transfer correlations of practical accuracy.

A practice of presenting dimensional results, such as heat transfer coefficients, in lieu of Nu in the experimental literature may help minimize the impact of these large uncertainties when validating models. This, however, limits the agnosticism of models and the applicability of results to varied scales. The data presented here suggest this inflated uncertainty effect is concentrated precisely in the location where the greatest potential benefit of sCO_2 heat transfer is observed, so clearly there remains a need in the heat transfer community to better characterize the behavior in this region. A suggested approach may be the study of flows at still larger operating pressure, where fluid properties remain strong functions of temperature, but their gradients lead to more manageable property uncertainties.

An upper limit on the magnitude of these gentler gradients is the subject of future work, but novel correlations accounting for variable fluid properties could in this way be developed with uncertainties approaching those found in subcritical flows. These could then be applied to the near-critical region for a more rigorous heat transfer characterization than is currently possible.

REFERENCES

Adebiyi, G., & Hall, W. (1976). Experimental investigation of heat transfer to supercritical pressure carbon dioxide in a horizontal pipe. *International Journal of Heat and Mass Transfer*, 19(7), 715-720. doi:10.1016/0017-9310(76)90123-X

Ahn, Y., Bae, S. J., Kim, M., Cho, S. K., Baik, S., Lee, J. I., & Cha, J. E. (2015). Review of supercritical CO2 power cycle technology and current status of research and development. *Nuclear Engineering and Technology*, 47(6), 647-661. doi:10.1016/j.net.2015.06.009

Ameli, A., Afzalifar, A., Turunen-Saaresti, T., & Backman, J. (2018). Effects of real gas model accuracy and operating conditions on supercritical CO2 compressor performance and flow field. *Journal of Engineering for Gas Turbines and Power*, 140(6) doi:10.1115/1.4038552

Avadhanula, V. K., & Held, T. J. (2017). Transient modeling of a supercritical CO2 power cycle and comparison with test data. *Proceedings of the ASME Turbo Expo.* doi:10.1115/GT2017-63279

Barber-Nichols, Inc. *Turbo-Machinery Considerations Using Super-Critical Carbon Dioxide Working Fluid for a Closed Brayton Cycle*.

Baskov, V. L., Kuraeva, I. V., & Protopopov, V. S. (1977). Heat transfer with the turbulent flow of a liquid at supercritical pressure in tubes under cooling conditions. *High Temperature*, 15(1), 81-86. Retrieved from www.scopus.com

Bellan, J. (2000). Supercritical (and subcritical) fluid behavior and modeling: Drops, streams, shear and mixing layers, jets and sprays. *Progress in Energy and Combustion Science*, 26(4), 329-366. doi:10.1016/S0360-1285(00)00008-3

Bergman, T., et al. (2011). *Introduction to Heat Transfer*: John Wiley & Sons, Inc, Jefferson City, MO, USA.

Bourke, P. J., Pulling, D. J., Gill, L. E., & Denton, W. H. (1970). Forced convective heat transfer to turbulent CO2 in the supercritical region. *International Journal of Heat and Mass Transfer*, 13(8), 1339-1348. doi:10.1016/0017-9310(70)90074-8

Bringer, R., & Smith, J. (1957). Heat Transfer in the Critical Region. *American Institute of Chemical Engineers Journal*, 3(1), 49-55. doi: 10.1002/aic.690030110

Bruch, A., Bontemps, A., & Colasson, S. (2009). Experimental investigation of heat transfer of supercritical carbon dioxide flowing in a cooled vertical tube. *International Journal of Heat and Mass Transfer*, 52(11), 2589-2598. doi:10.1016/j.ijheatmasstransfer.2008.12.021

Brun, K., et al. (2014). *Novel Supercritical Carbon Dioxide Power Cycle Utilizing Pressurized Oxy-combustion in Conjunction with Cryogenic Compression*. San Antonio, TX, USA: SWRI.

Bunker, R. S. (2007). Gas turbine heat transfer: Ten remaining hot gas path challenges. *Journal of Turbomachinery*, 129(2), 193-201. doi:10.1115/1.2464142

Cabeza, L. F., de Gracia, A., Fernández, A. I., & Farid, M. M. (2017). Supercritical CO2 as heat transfer fluid: A review. *Applied Thermal Engineering*, 125, 799-810. doi:10.1016/j.applthermaleng.2017.07.049

Carlès, P. (2010). A brief review of the thermophysical properties of supercritical fluids. *The Journal of Supercritical Fluids*, 53(1), 2-11. doi:10.1016/j.supflu.2010.02.017

Carraro, G., Danieli, P., Lazzaretto, A., & Boatto, T. (2021). A common thread in the evolution of the configurations of supercritical CO2 power systems for waste heat recovery. *Energy Conversion and Management*, 237 doi:10.1016/j.enconman.2021.114031

Çengel, Y. (2011). *Thermodynamics: An Engineering Approach*. McGraw Hill Education Ltd., New York, NY, USA.

Cook, G. R., Metzger, P. H., & Ogawa, M. (1966). Absorption, photoionization, and fluorescence of CO2. *The Journal of Chemical Physics*, 44(8), 2935-2942. doi:10.1063/1.1727158

Dang, C., & Hihara, E. (2004). In-tube cooling heat transfer of supercritical carbon dioxide. part 1. experimental measurement. *International Journal of Refrigeration*, 27(7), 736-747. doi:10.1016/j.ijrefrig.2004.04.018

Engware, *Brayton cycle efficiency.* [Image]. Licensed under CC BY 2.5. Retrieved from https://en.wikipedia.org/wiki/Brayton_cycle#/media/File:GFImg7.png

Engware, *Brayton-cycle specific power output*. [Image]. Licensed under CC BY 2.5. Retrieved from https://en.wikipedia.org/wiki/Brayton_cycle#/media/File:GFImg8.png

Fang, X. (1999). Modeling and analysis of gas coolers. *ACRC CR-15, Department of Mechanical and Industrial Engineering, University of Illinois at Urbana-Champaign*, USA.

Fernandes, R., Ricklick, M., Prasad, A., & Pai, Y. (2017). Benchmarking Reynolds averaged Navier–Stokes turbulence models in internal pin fin channels. *Journal of Thermophysics and Heat Transfer*, 31(4), 976-982. doi:10.2514/1.T5046

Filonenko, G. (1954). Hydraulic resistance of pipes. *Teploenergetika*, 1(4), 40-44.

Gnielinski, V. (1975). Neue gleichungen für den wärme- und den stoffübergang in turbulent durchströmten rohren und kanälen. *Forschung Im Ingenieurwesen*, 41(1), 8-16. doi:10.1007/BF02559682

Gupta, S., Saltanov, E., Mokry, S. J., Pioro, I., Trevani, L., & McGillivray, D. (2013). Developing empirical heat-transfer correlations for supercritical CO2 flowing in vertical bare tubes. *Nuclear Engineering and Design*, 261, 116-131. doi:10.1016/j.nucengdes.2013.02.048

Hinze, J. (1975). *Turbulence*. McGraw-Hill, New York, NY, USA.

Huai, X., & Koyama, S. (2007). Heat transfer characteristics of supercritical CO2 flow in small-channeled structures. *Experimental Heat Transfer*, 20(1), 19-33. doi:10.1080/08916150600977424

Huang, D., Wu, Z., Sunden, B., & Li, W. (2016). A brief review on convection heat transfer of fluids at supercritical pressures in tubes and the recent progress. *Applied Energy*, 162, 494-505. doi:10.1016/j.apenergy.2015.10.080

Innovative Scientific Solutions Inc., *Calibration of UniTemp TSP*. [Image]. Retrieved from https://innssi.com/temperature-sensitive-paints/

"Emission Spectra of CCTR TSP Excited using LM2X-DM-460 LED," Temperature Sensitive Paints, Innovative Scientific Solutions, Inc., https://innssi.com/temperature-sensitive-paints/

Jackson, J. (2002). Consideration of the heat transfer properties of supercritical pressure water in connection with the cooling of advanced nuclear reactors. *Proceedings of the 13th Pacific Basin Nuclear Conference*, Shenzhen City, China, October 21-25.

Jiang, P., Wang, Z., & Xu, R. (2018). A modified buoyancy effect correction method on turbulent convection heat transfer of supercritical pressure fluid based on RANS model. *International Journal of Heat and Mass Transfer*, 127, 257-267. doi:10.1016/j.ijheatmasstransfer.2018.07.042

Kim, H. Y., Kim, H., Kang, D. J., Song, J. H., & Bae, Y. Y. (2008). Experimental investigations on heat transfer to CO2 flowing upward in a narrow annulus at supercritical pressures. *Nuclear Engineering and Technology*, 40(2), 155-162. doi:10.5516/NET.2008.40.2.155

Kline, S., & McClintock, F. (1953). Describing uncertainties in single-sample experiments. *Mechanical Engineering*, 75, 3-8.

Krasnoshchekov, E., & Protopopov, V. (1969). Local heat transfer of carbon dioxide under supercritical pressure under cooling conditions. *Teplofizika Bysokikh*

Temperatur, 7(5), 922-930. Retrieved from www.scopus.com

Kuang, G., Ohadi, M., & Dessiatoun, S. (2008). Semi-empirical correlation of gas cooling heat transfer of supercritical carbon dioxide in microchannels. *HVAC&R Research*, 14(6), 861-870. doi:10.1080/10789669.2008.10391044

Kwon, J. S., Son, S., Heo, J. Y., & Lee, J. I. (2020). Compact heat exchangers for supercritical CO2 power cycle application. *Energy Conversion and Management*, 209, 112666. doi:10.1016/j.enconman.2020.112666

Lazova, M., Huisseune, H., Kaya, A., Lecompte, S., Kosmadakis, G., & De Paepe, M. (2016). Performance evaluation of a helical coil heat exchanger working under supercritical conditions in a solar organic Rankine cycle installation. *Energies (Basel)*, 9(6), 432. doi:10.3390/en9060432

Lee, H., Kim, H., Yoon, J., Choi, K., & Son, C. (2013). The cooling heat transfer characteristics of the supercritical CO2 in micro-fin tube. *Heat and Mass Transfer*, 49(2), 173-184. doi:10.1007/s00231-012-1070-2

Li, Y., Sun, F., Xie, G., Sunden, B., & Qin, J. (2019). Numerical investigation on flow and thermal performance of supercritical CO2 in horizontal cylindrically concaved tubes. *Applied Thermal Engineering*, 153, 655-668. doi:10.1016/j.applthermaleng.2019.03.034

Liao, S. M., & Zhao, T. S. (2002). Measurements of heat transfer coefficients from supercritical carbon dioxide flowing in horizontal Mini/Micro channels. *Journal of Heat Transfer*, 124(3), 413-420. doi:10.1115/1.1423906

Liu, T., & Sullivan, J. (2005). *Pressure and Temperature Sensitive Paints*. Springer, New York.

Liu, Z., He, Y., Yang, Y., & Fei, J. (2014). Experimental study on heat transfer and pressure drop of supercritical CO2 cooled in a large tube. *Applied Thermal Engineering*, 70(1), 307-315. doi:10.1016/j.applthermaleng.2014.05.024

Lorentzen, G. (1994). Revival of carbon dioxide as a refrigerant. *International Journal of Refrigeration*, 17(5), 292-301. doi:10.1016/0140-7007(94)90059-0

Menter, F. R. (1994). Two-equation eddy-viscosity turbulence models for engineering applications. *AIAA Journal*, 32(8), 1598-1605. doi:10.2514/3.12149

Metzger, D. E., & Haley, S. W. (1982). Heat transfer experiments and flow visualization for arrays of short pin fins. *Proceedings of the ASME Turbo Expo*. doi:10.1115/82-GT-138

Moffat, R. J. (1988). Describing the uncertainties in experimental results. *Experimental*

Thermal and Fluid Science, 1(1), 3-17. doi:10.1016/0894-1777(88)90043-X

Mokry, S., & Pioro, I. (2011). Heat Transfer Correlation for Supercritical Carbon Dioxide Flowing Upward in a Vertical Bare Tube. *Proceedings of the Supercritical CO_2 Power Cycles Symposium*, May 24-25, Boulder, CO, USA.

Oh, H., & Son, C. (2010). New correlation to predict the heat transfer coefficient in-tube cooling of supercritical CO2 in horizontal macro-tubes. *Experimental Thermal and Fluid Science*, 34(8), 1230-1241. doi:10.1016/j.expthermflusci.2010.05.002

Omary, M. A., Kassab, R. M., Haneline, M. R., Elbjeirami, O., & Gabbaï, F. P. (2003). Enhancement of the phosphorescence of organic luminophores upon interaction with a mercury trifunctional lewis acid. *Inorganic Chemistry*, 42(7), 2176-2178. doi:10.1021/ic034066h

Pai, Y., et al. (2017). Preliminary Investigation of Bio-Inspired Cylinders for Improved Thermal Performance of Internal Cooling Channels. *Proceedings of the 53rd AIAA/SAE/ASEE Joint Propulsion Conference*, 10-12 July, Atlanta, GA, USA. doi:10.2514/6.2017-4977

Pai, Y., Prasad, A., & Ricklick, M. (2020). Extended surface heat transfer coefficients via endwall temperature measurements. *Journal of Thermophysics and Heat Transfer*, 34(1), 101-108. doi:10.2514/1.T5750

Petrov, N. E., & Popov, V. N. (1985). Heat transfer and resistance of carbon dioxide being cooled in the supercritical region. *Thermal Engineering (English Translation of Teploenergetika)*, 32(3), 131-134. Retrieved from www.scopus.com

Duffey, R. B., & Pioro, I. L. (2005). Experimental heat transfer of supercritical carbon dioxide flowing inside channels (survey). *Nuclear Engineering and Design*, 235(8), 913-924. doi:10.1016/j.nucengdes.2004.11.011

Pitla, S. S., Groll, E. A., & Ramadhyani, S. (2002). New correlation to predict the heat transfer coefficient during in-tube cooling of turbulent supercritical CO2. *International Journal of Refrigeration*, 25(7), 887-895. doi:10.1016/S0140-7007(01)00098-6

Prasad, A., & Ricklick, M. (2017). A Detailed Uncertainty Analysis of Heat Transfer Experiments using Temperature Sensitive Paint. *55th AIAA Aerospace Sciences Meeting*, 9-13 January, Grapevine, TX, USA. doi:10.2514/6.2017-1283

Prasad, A., et al. (2018). Investigation of Bio-Inspired Pin Geometries for Enhanced Heat Transfer Applications. *2018 Joint Propulsion Conference*, 9-11 July, Cincinnati, OH, USA. doi:10.2514/6.2018-4429

Preda, T., Saltanov, E., Pioro, I., & Gabriel, K. S. (2012). Development of a heat transfer correlation for supercritical CO2 based on multiple data sets. *Proceedings of the International Conference on Nuclear Engineering*, 5(1) 211-217. doi:10.1115/ICONE20-POWER2012-54516

Pritchard, P. (2011). *Fox and McDonald's Introduction to Fluid Mechanics*, John Wiley & Sons, Inc., USA.

Saltanov, E., Pioro, I., Mann, D., Gupta, S., Mokry, S., & Harvel, G. (2015). Study on specifics of forced-convective heat transfer in supercritical carbon dioxide. *Journal of Nuclear Engineering and Radiation Science*, 1(1) doi:10.1115/1.4026395

Short, B. E., Raad, P. E., & Price, D. C. (2002). Performance of pin fin cast aluminum coldwalls, part 2: Colburn j-factor correlations. *Journal of Thermophysics and Heat Transfer*, 16(3), 397-403. doi:10.2514/2.6693

Simões, P. C., Afonso, B., Fernandes, J., & Mota, J. P. B. (2008). Static mixers as heat exchangers in supercritical fluid extraction processes. *The Journal of Supercritical Fluids*, 43(3), 477-483. doi:10.1016/j.supflu.2007.07.015

Smith, C. R., Sabatino, D. R., & Praisner, T. J. (2001). Temperature sensing with thermochromic liquid crystals. *Experiments in Fluids*, 30(2), 190-201. doi:10.1007/s003480000154

Son, C., & Park, S. (2006). An experimental study on heat transfer and pressure drop characteristics of carbon dioxide during gas cooling process in a horizontal tube. *International Journal of Refrigeration*, 29(4), 539-546. doi:10.1016/j.ijrefrig.2005.10.010

Span, R., & Wagner, W. (1996). A new equation of state for carbon dioxide covering the fluid region from the triple-point temperature to 1100 K at pressures up to 800 MPa. *Journal of Physical and Chemical Reference Data*, 25(6), 1509-1596. doi:10.1063/1.555991

Suo-Antilla, A., & Wright, S. (2011). Computational Fluid Dynamics Code for Supercritical Fluids. *Proceedings of the Supercritical CO_2 Power Cycles Symposium*, May 24-25, Boulder, CO, USA.

Tanimizu, K., & Sadr, R. (2016). Experimental investigation of buoyancy effects on convection heat transfer of supercritical CO2 flow in a horizontal tube. *Heat and Mass Transfer*, 52(4), 713-726. doi:10.1007/s00231-015-1580-9

Tennekes, H., & Lumley, J. (1972). [Course content]. *A First Course in Turbulence*. MIT Press, Cambridge, MA, USA.

Thome, J., (2006). *Engineering Data Book III*. Wolverine Tube, Inc.

VanFossen, G. J. (1982). Heat-transfer coefficients for staggered arrays of short pin fins. *Journal of Engineering for Gas Turbines and Power*, 104(2), 268-274. doi:10.1115/1.3227275

Vollmer, M., & Möllmann, K. (2018). *Infrared thermal imaging: Fundamentals, research and applications*. John Wiley & Sons, Inc, Newark, NJ, USA.

Wang, J., Guan, Z., Gurgenci, H., Veeraragavan, A., Kang, X., Sun, Y., & Hooman, K. (2018). Numerical study on cooling heat transfer of turbulent supercritical CO2 in large horizontal tubes. *International Journal of Heat and Mass Transfer*, 126, 1002-1019. doi:10.1016/j.ijheatmasstransfer.2018.06.070

Wang, J., Guan, Z., Gurgenci, H., Veeraragavan, A., Kang, X., & Hooman, K. (2019). A computationally derived heat transfer correlation for in-tube cooling turbulent supercritical CO2. *International Journal of Thermal Sciences*, 138, 190-205. doi:10.1016/j.ijthermalsci.2018.12.045

Wauchop, T., & Broida, H. (1971). Cross Sections for the Production of Fluorescence of CO2 in the Photoionization of CO2 by 58.4-Nanometer Radiation. *J. of Geophysical Research*, 76(1).

White, M. T., Bianchi, G., Chai, L., Tassou, S. A., & Sayma, A. I. (2021). Review of supercritical CO2 technologies and systems for power generation. *Applied Thermal Engineering*, 185 doi:10.1016/j.applthermaleng.2020.116447

Wright, L. M., & Han, J.-C. (2013). Heat transfer enhancement for turbine blade internal cooling. *Proceedings of the ASME 2013 Heat Transfer Summer Conf. Collocated with the ASME 2013 7th Int. Conf. on Energy Sustainability and the ASME 2013 11th Int. Conf. on Fuel Cell Science, Engineering and Technology*, doi:10.1115/HT2013-17813

Yang, V. (2000). Modeling of supercritical vaporization, mixing, and combustion processes in liquid-fueled propulsion systems. *Proceedings of the Combustion Institute*, 28(1), 925-942. doi:10.1016/s0082-0784(00)80299-4

Yoon, S. H., Kim, J. H., Hwang, Y. W., Kim, M. S., Min, K., & Kim, Y. (2003). Heat transfer and pressure drop characteristics during the in-tube cooling process of carbon dioxide in the supercritical region. *International Journal of Refrigeration*, 26(8), 857-864. doi:10.1016/S0140-7007(03)00096-3

Zhang, X. R., & Yamaguchi, H. (2007). Forced convection heat transfer of supercritical CO2 in a horizontal circular tube. *The Journal of Supercritical Fluids*, 41(3), 412-420. doi:10.1016/j.supflu.2006.11.003

Zhu, B., Xu, J., Wu, X., Xie, J., & Li, M. (2019). Supercritical “boiling” number, a new parameter to distinguish two regimes of carbon dioxide heat transfer in tubes. *International Journal of Thermal Sciences*, 136, 254-266. doi:10.1016/j.ijthermalsci.2018.10.032

PUBLICATIONS

Sullivan, N., Chao, Y., Boetcher, S., & Ricklick, M. (2021). Impact of uncertainty on prediction of supercritical CO2 properties and Nusselt numbers. *Journal of Heat Transfer*, doi:10.1115/1.4051856

Sullivan, N., & Ricklick, M. (2019). Semi-intrusive temperature measurement technique in supercritical carbon dioxide. *Proceedings of AIAA Propulsion and Energy Conference*, 19-22 August, Indianapolis, IN, USA. doi:10.2514/6.2019-4324

Sullivan, N., Ricklick, M., & Boetcher, S. (2020). Supercritical co2 heat transfer in a staggered pin-fin channel. *Proceedings of AIAA Propulsion and Energy Conference.* doi:10.2514/6.2020-3696

Sullivan, N., Ricklick, M., Boetcher, S., & Chao, Y. (2021, August). Heat Transfer Enhancement Optimization in Supercritical CO_2 with Reduced-Order Model. *AIAA Propulsion and Energy Conference*, 9-11 August, Virtual Event.